Study of the plasma phenomenon in HiPIMS discharge. : Application to the reactive deposition of tantalum and hafnium carbide nanocomposite coatings and characterization of their physicochemical, structural, mechanical and oxidation resistance propertie.

Huan Luo

Huan Luo. Study of the plasma phenomenon in HiPIMS discharge. : Application to the reactive deposition of tantalum and hafnium carbide nanocomposite coatings and characterization of their physicochemical, structural, mechanical and oxidation resistance propertie.. Material chemistry. Université Bourgogne Franche-Comté, 2020. English. NNT : 2020UBFCA010 . tel-03697503

HAL Id: tel-03697503
https://theses.hal.science/tel-03697503

Submitted on 17 Jun 2022

THESE DE DOCTORAT DE L'ETABLISSEMENT UNIVERSITE BOURGOGNE FRANCHE-COMTE

PREPAREE A UNIVERSITE DE TECHNOLOGIE DE BELFORT-MONTBELIARD

Ecole doctorale n°37

École Doctorale Sciences Pour l'Ingénieur et Microtechniques

Doctorat de Matériaux

Par

LUO Huan

Study of the plasma phenomenon in HiPIMS discharge. Application to the reactive deposition of tantalum and hafnium carbide nanocomposite films and characterization of their physicochemical, structural, mechanical and oxidation resistance properties.

Thèse présentée et soutenue à Montbéliard, le 16/06/2020

Composition du Jury :

M. SANCHETTE Frederic	Professeur	Université de Technologie de Troyes, France	Président du jury
M. CAVAlLEIRO Albano	Professeur	University of Coimbra, Portugal	Rapporteur
M. CZERWIEC Thierry	Professeur	Université de Lorraine, France	Rapporteur
Mme. NOUVEAU Corinne	Maître de Conférences	Arts et Métiers Paris Tech de Cluny, France	Examinateur
M. BILLARD Alain	Professeur	Université de Technologie de Belfort-Montbéliard, France	Directeur de thèse
M. GAO Fei	Professeur	Université de Technologie de Belfort-Montbéliard, France	Co-Directeur de thèse

Acknowledgment

The author did all the works in this thesis in the team of Micro Nano Materials and Surfaces (MINAMAS), department of Micro Nano Sciences and Systems (MN2S), Franche-Comté Electronic Mechanic Thermic and Optic–Sciences and Technologies (FEMTO-ST), at University Bourgogne Franche-Comté, UTBM, CNRS.

I would like to firstly express my sincerest gratitude to my supervisor Prof. Alain BILLARD, who has given me the most meticulous guidance and helps in research works. I am deeply impressed by his abundant knowledge and professionalism and inspired by his dedication to his academic career. I would also like to express my appreciation to my co-supervisor Prof. Fei GAO, who has given me insightful discussions and constructive suggestions on the calculation methods in the plasma model. I am touched by his academic and professional attitude and I appreciate his help in giving me the opportunity to get funding from the UT-INSA (2016) project and encourage me to pursue my Ph.D. in France.

I would like to express my gratitude to Dr. Pascal Briois, Dr. Mohammad Arab Pour Yazdi, and Dr. Eric Aubry for their constructive advice and encouragement for my experiments. I would also like to express my thanks to all the friends and colleagues working in the laboratory for their advice and for the good atmosphere every day, they are: Ms. Mahsasadat Safavi, Mr. Khalid Neffaa, Mr. Christian Petitot, Ms. Emmanuelle Arcens, Mr. Siavash Bakhtiarnia, Mr.Xiaolei Ye.

I would like to sincerely thank all the friends who work in Belfort and in China. I would thank Dr. Hui Sun for his generous help on living issues in France. He also has enlightened me many times by his substantial knowledge and penetrating views. I would also thank Dr. Chen Liu, Dr. Rui Ma, Dr. Xiujuan Fan, Dr. Xieliang Xie, Mr. Shengrong Zhuo, Mr. Yang Zhou, and Mr. Zhiguang Hua for all the happy times spent together in the past three years.

I would like to thank the China Scholarship Council (CSC), who has financially support me studying in France.

At last, I would like to express my deepest love and the most profound gratitude to my family. I am so grateful that my parents have supported me a lot and encourage me to bravely try whatever I want. I am also so grateful that my husband Dr. Hao Bai has accompanied me all the time during my Ph.D. study. Thank you for your tolerance and understanding of my character. Thank you for your selfless love.

.

Abstract

With the increasing requirements for thin film performance, **Hi**gh **P**ower **I**mpulse **M**agnetron **S**puttering (HiPIMS) technology has been developed and considered as a reliable and effective method for film preparation. HiPIMS technology adopts a power supply mode of high power impulse which provides a peak power density of up to KW/cm^2. The excited high ionization fraction of the sputtered species allows for much greater flexibility for manipulating film structure and performance, leading to films with unique properties that are often unachievable in the other PVD approaches. However, the underlying plasma mechanism for supporting film growth involved in HiPIMS technology is currently blurred, which poses some challenges for HiPIMS. Moreover, HiPIMS technology is still expensive and stationed in the laboratory, many films with desirable properties and potentials have not been explored under the HiPIMS framework.

Within this work, (i) the driven mechanism of high density plasma coherent structure (i.e., spokes) in the HiPIMS discharge and (ii) how the structure and properties of the nanocomposite films of TaC/a-C:H and HfC/a-C:H are regulated by HiPIMS were investigated. In the study of the driven mechanism of spokes, based on the analysis of the dispersion relationship of HiPIMS plasma and the evolution of the coupling between two azimuthal waves, the coupling-induced wave model was proposed. The validity and accuracy of the proposed model were verified by comparison with published experimental data on the HiPIMS spokes. In the study of nanocomposite TaC/a-C:H and HfC/a-C:H films, the chemical bond states, structure, morphology, residual stress, mechanical and tribological properties, thermal stability as well as oxidation resistance of the films were investigated. By comparison with these films deposited by DC magnetron sputtering, it is demonstrated that HiPIMS technology provides a potential strategy for preparing higher performance TaC/a-C:H and HfC/a-C:H films in terms of hardness, friction coefficient and wear resistance, oxidation resistance and thermal stability by modulating the chemical bonding state and nanocomposite structure of the films through reactive plasma. Moreover, HiPIMS

deposited films have greater potential for further hardening after high-temperature vacuum annealing.

Résumé

Avec les exigences croissantes pour les performances des films minces, la technologie de pulvérisation magnétron par impulsions de haute puissance (HiPIMS) a été développée et est considérée comme une méthode fiable et efficace pour la préparation des films. La technologie HiPIMS adopte un mode d'alimentation par impulsions de puissance élevée qui fournit une densité de puissance maximale atteignant le KW/cm^{-2}. La forte ionisation des espèces pulvérisées permet une bien plus grande flexibilité pour ajuster la structure et les performances du film, conduisant à des films avec des propriétés uniques qui sont souvent irréalisables dans les autres approches PVD. Cependant, le mécanisme sous-jacent du plasma pour soutenir la croissance du film impliqué dans la technologie HiPIMS est actuellement flou, ce qui pose certains défis pour la technologie HiPIMS. De plus, la technologie HiPIMS reste onéreuse et principalement limitée au laboratoire, de nombreux films aux propriétés et potentiels souhaitables n'ont pas été explorés dans le cadre de la pulvérisation HiPIMS.

Dans ce travail, (i) l'origine de la structure cohérente du plasma haute densité (i.e., les « spokes ») dans la décharge HiPIMS et (ii) comment la structure et les propriétés des films nanocomposites de TaC/a-C: H et HfC/a-C: H sont gérées par HiPIMS ont été étudiés. Dans l'étude du mécanisme de formation des « spokes », basée sur l'analyse de la relation de dispersion du plasma HiPIMS et l'évolution du couplage entre deux ondes azimutales, un modèle d'onde induit par couplage a été proposé. La validité et l'exactitude du modèle proposé ont été vérifiées par comparaison avec les données expérimentales publiées sur les « spokes » HiPIMS. Dans l'étude des films nanocomposites TaC/a-C: H et HfC/a-C: H, les états des liaisons chimiques, la structure, la morphologie, la contrainte résiduelle, les propriétés mécaniques et tribologiques, la stabilité thermique ainsi que la résistance à l'oxydation des films ont été étudiés. En comparaison avec ces films déposés par pulvérisation magnétron DC, il est démontré que la technologie HiPIMS permet une stratégie potentielle pour préparer des films TaC/a-C: H et HfC/a-C: H plus performants en termes de dureté, de coefficient de frottement et de résistance à l'usure, de résistance à l'oxydation et de stabilité thermique

en modulant l'état de liaison chimique et la structure nanocomposite des films à travers un plasma réactif. De plus, les films déposés par HiPIMS ont un plus grand potentiel de durcissement supplémentaire après un recuit sous vide à haute température.

Content

General introduction

Surface engineering is to impart special mechanical or Physico-chemical properties to the base material through the surface coating and/or surface modification technology. It can meet the wear resistance, corrosion resistance, heat resistance and decoration of the surface of the base material, but also can endow the surface of the base material some special properties in optical, electrical, magnetic, thermal, chemical and biological aspects. Moreover, surface engineering has developed into an interdisciplinary discipline that spans materials science, tribology, physics, chemistry, interface mechanics, and surface mechanics. Its rapid development and widespread application have remarkably contributed to progress for industrial development.

At present, the plasma-based physical vapor deposition (PVD) has been deeply studied in academia and widely used in industrial applications. In the plasma-based PVD process, the deposition species are either evaporated by thermal evaporation or sputtered from the cathode target by ion bombardment. For decades, sputtering has been considered a flexible, reliable and effective method for film preparation. Also, the magnetron sputtering technology that was developed during the 1960 s and 1970 s has been the mainstay in plasma-based sputtering technologies for the past three decades. More recently, with the development of technology and increasingly demanding performance requirements, **Hi**gh **P**ower **I**mpulse **M**agnetron **S**puttering (HiPIMS) technology has been developed.

HiPIMS technology adopts a power supply mode of high power impulse, which provides a peak power density of up to KW/cm^{-2}, where the peak power exceeds the time-averaged power by typically 2 orders of magnitude, and a current density of up to 3-4 A/cm for magnetron sputtering cathode. Meanwhile, the impulse frequency in the range of 50–5000Hz and the low duty cycle in the range of 0.5%–5% are applied. It results in a very high plasma density and high ionization fraction of the sputtered particles, allowing for much greater flexibility for manipulating film structure and performance through additional modulation of the energy and density of the deposition species, leading to films with unique properties that are often unachievable in the other

PVD approaches. Such HiPIMS process is also capable of preparing dense, homogenous and defect-free films with excellent adhesion to the substrate, which are the ideal properties desired as a protective film and is necessary for industrial-scale film production.

However, the underlying plasma mechanism for driving thin film growth involved in the HiPIMS deposition process is currently blurred, and it is still really expensive and not yet developed enough at the industrial level. The unknown plasma discharge mechanism causes HiPIMS to face some challenges, for example, the low deposition rate. Moreover, since HiPIMS technology is still stationed in the laboratory, many films with desirable properties and potentials (suggested by other surface technologies) have not been explored under the HiPIMS framework. A typical example is a carbon-based nanocomposite film of transition metal. However, that is exactly what HiPIMS technology is good at, because it can more flexibly and effectively adjust the structure of the film during the growth process. These issues encourage researchers to go ahead to explore the discharge mechanism of HiPIMS and the characteristics of the thin films it makes.

Within this context, the main purpose of this Ph.D. project is to study the driven mechanism of high density plasma coherent structure (i.e., spoke) of the HiPIMS plasma, and investigate how the structure and properties of the nanocomposite films of TaC/a-C:H and HfC/a-C:H are regulated by HiPIMS process. In previous research work, the majority of researches on the phenomenon of spokes in HiPIMS discharges focus on experimental observations, the theoretical investigations are rarely done. The vast majority of reported TaC/a-C:H and HfC/a-C:H films are concentrated in the conventional, well-proven direct current magnetron sputtering (DCMS) process, and few studies have been conducted under HiPIMS system.

This thesis is composed of four chapters. Chapter 1 presents the principles of HiPIMS technology used for film preparation and the experimental details and characterization techniques employed in this Ph.D. project. Moreover, the deposition equipment, selected substrates, and measurement parameters are fully displayed.

In Chapter 2, the dispersion relationship suitable for describing the plasma characteristics during HiPIMS discharge is deduced and the evolution of the coupling between two azimuthal waves in the plasma is investigated. Based on the dynamic evolution of this coupling, the coupling-induced wave model is proposed for explaining the driven mechanism of the spoke.

In Chapter 3, TaC/a-C:H films deposited in HiPIMS are investigated and compared with those deposited in DC. Note that for the TaC/a-C:H films deposited in DC, except for different power supply modes, other deposition parameters remain the same, such as discharge current, working pressure, argon and carbon source C_2H_2 flow rates. The chemical bonding state, structure, morphology, mechanical and tribological properties as well as oxidation resistance of the prepared TaC/a-C:H films are analyzed and compared. Moreover, the effects of the application of substrate bias on the above-mentioned characteristics and performance of the film are also systematically discussed.

Chapter 4 is dedicated to exploring the HfC/a-C:H films which serve as another hotspot in transition metal carbon-based nanocomposites. In addition to mechanical properties, tribological performance and oxidation resistance, the analysis of the thermal stability of HfC/a-C:H films is emphasized. Moreover, by comparing the HfC/a-C:H films deposited in (i) different C_2H_2 flow rates and (ii) different deposition conditions, HiPIMS and DC (without substrate bias), the correlations between carbon content, deposition conditions and mechanical properties, tribological behavior, oxidation resistance, and thermal stability are systematically discussed and established. At the end of this thesis, the significance of clarifying the driving mechanism of the HiPIMS plasma phenomenon involved in the film deposition and the superiority of HiPIMS technology in depositing carbon-based nanocomposite films are summarized.

Chapter 1 Synthesis and characterization of thin films

The purpose of this thesis is to study the plasma characteristics of HiPIMS technology and employ the advantages of HiPIMS plasma to deposit carbon-based nanocomposite films of two transition metals to improve their performance, such as mechanical properties, tribological performances, and oxidation resistance. Therefore, it is necessary to describe the film deposition process and introduce the techniques used to characterize and measure the thin films prepared. The first part of this chapter is dedicated to the production process used for thin film deposition. In the second part, the different measurement techniques required to characterize the morphology, structure, chemical bonding state and multiple properties of thin films are described.

1.1 Synthesis of thin films

1.1.1 Introduction of HiPIMS deposition technique

Plasma-based physical vapor deposition (PVD) has found widespread use in various industrial applications, especially in thin film production. In the plasma-based PVD process, the deposition species are either evaporated by thermal evaporation or sputtered from the cathode target by ion bombardment. For decades, sputtering has been considered a flexible, reliable and effective method for film preparation. Also, the magnetron sputtering technology that was developed during the 1960 s and 1970 s has been the mainstay in plasma-based sputtering applications for the past three decades [1].

High power impulse magnetron sputtering (HiPIMS) technology is a kind of ionized physical vapor deposition technology based on magnetron sputtering developed in recent years. It employs high power pulses as the power supply mode to provide peak power density up to the order of KW/cm^{-2} for magnetron sputtering cathodes [2], while simultaneously, current density up to 3-4 A/cm^{-2} is obtained on the target surface. The frequency in the range of 50–5000 Hz and the low duty cycle in the range of 0.5% –5% are applied [3][4] to ensure that the magnetron sputtering cathode does not overheat when the average power is comparable to that of conventional direct current magnetron sputtering. This mode of power supply results in high energy density and high ionization fraction of the sputtered particles [5][6], which facilitates more effective regulation of film growth by controlling the energy and direction of the sputtered species. It is a significant advantage over conventional DC magnetron sputtering where the sputtered vapor consists mainly of neutral species [7][8]. Moreover, the pulsing of the discharge also allows for much greater flexibility in the HiPIMS process in film preparation due to additional control parameters such as pulse width, duty cycle, and pulse frequency. Based on the above discharge characteristics, HiPIMS technology has become a hot spot in international research and the studies on (i) the characteristics of high power impulse discharge [9][10], (ii) the physical mechanism of plasma [11][12], and (iii) the deposited thin films [13][14] has progressed rapidly.

1.1.2 Principle of HiPIMS deposition technique

Figure 1-1 presents the schematic diagram of the working principle for HiPIMS deposition technique illustrating collective particle dynamics. The plasma for thin film deposition is generated by the potential difference between the magnetron cathode and the reactor wall serving as the anode. During the plasma generation process, its initial excitation begins with electron ionization triggered by the electric field of the high power impulse, and its maintenance comes from the ring-shaped control of the electrons by the interaction of the electric field and magnetic field configuration.

In the typical HiPIMS device, electrons are magnetized by the magnetron because their gyration radius is much smaller than the characteristic size of the magnetron, while ions are unmagnetized due to their larger gyration radius [15][16]. Therefore, during the HiPIMS discharge process, the electrons in the plasma are constrained by the orthogonal distribution of the electric and magnetic fields, while the ions are guided only by the electric field.

At the early stage of discharge, the electrons are excited by high power impulse and are constrained in the ionization region above the target surface to do $\mathbf{E} \times \mathbf{B}$ drift. If the magnetron generates a toroidal magnetic field, the electrons perform a closed circular motion in the form of a cycloid in the ionization region [17]. It greatly prolongs the motion path of the electrons, which enhances the collision probability under the premise that the average free path and the reaction space are not changed. Also, it promotes the gradual accumulation of the kinetic energy of the electrons in such a manner of motion to a level sufficient to cause electron ionization collisions [1], which is the key to the enhanced ionization rate.

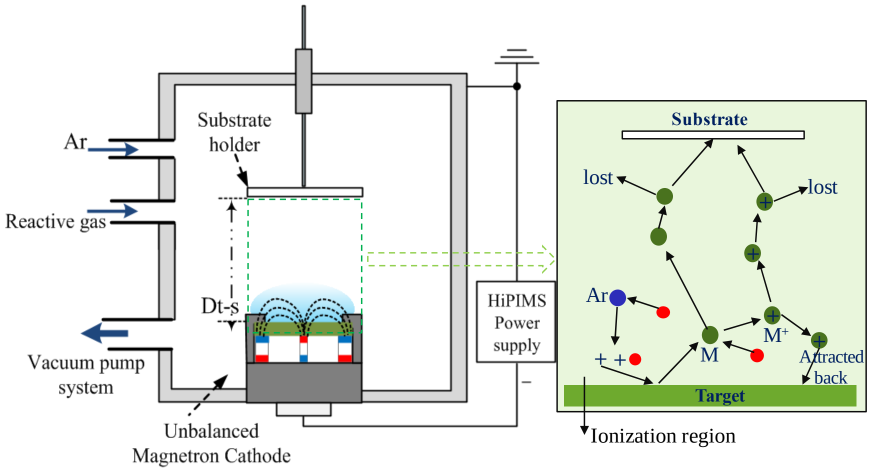

Figure 1-1. Schematic diagram of the working principle of HiPIMS deposition process.

During the $\mathbf{E} \times \mathbf{B}$ drift process, high-energy electrons collide with argon atoms and generate Ar ions and new electrons (the energy carried is weak), while most of the kinetic energy of the electrons participating in this collision is consumed. The Ar ions are accelerated to the cathode target under the action of the cathode potential drop and the target surface is bombarded with high energy ions to sputter the target atoms. The newly generated electrons are captured by the electric and magnetic fields and added to the electron flow that is performing the $\mathbf{E} \times \mathbf{B}$ drift, thereby starting to accumulate kinetic energy and waiting for the next cycle of collision ionization.

After the sputtering events, the sputtered target atoms are transported into the ionization region above the target surface. For the sputtered target atoms, there are two possibilities for their whereabouts. One is being ionized through the electron collision. When the sputtered particles pass through the ionization region, the energetic electrons that do $\mathbf{E} \times \mathbf{B}$ drift may cause this ionization collision. At this moment, the dominant ionization mechanism transitions from Penning ionization (that is, the ionization of the sputtered vapor is through impact with the Ar atoms that are in the metastable excited state) to electron impact ionization ($e+M \rightarrow M^{+}+2e$). Sputtered atoms are ionized into target ions M^{+} and new secondary electrons. The target ions M^{+} are then deposited toward the substrate after subsequent multiple scattering elastic collisions, which contributes to the film growth. It should be noted that a partial target ions M^{+} may be close enough to cathode potential drop and have a low kinetic energy. They are easily attracted back to the cathode direction and then accelerated across the high voltage sheath to take part in the resputtering mechanism. This resputtering caused by back-attracted target ions M^{+} promotes an increase in the ionization rate but impairs the deposition rate. The other is that part of the target sputtered atoms (carrying the energy obtained from the sputtering process of the noble atoms) escapes from the ionization region without undergoing ionization collision and without being affected by the cathode potential drop due to they are far away from the potential drop. Finally, they reach the substrate to participate in the growth of the film or be lost into the walls of the chamber.

Besides, a few percents of the bombarding gas ions do not participate in sputtering, but merely are neutralized at the target surface and reflected back to the ionization region. These reflected working gas atoms have inherently high energy since they are first accelerated toward the cathode (as ions) by the high potential cathode drop and most of that energy is not transferred to the target atoms. Thus the reflected gas atoms will collide with the neutral working gas and thereby increasing the gas dilution, while others will quickly leave the ionization region.

The by-products of each ionization collision, secondary electrons, are re-confined by the $\mathbf{E} \times \mathbf{B}$ drift and continue to participate in subsequent collision ionization (for maintaining the plasma and enhancing the ionization rate). As the number of ionization collisions of electrons increases, they are gradually migrated out of the range that the magnetic field can affect, accompanied by the gradual depletion of kinetic energy. Electrons that eventually move away from the ionization region will reach the substrate by the electric field **E**. Since the energy of the electron is already very low, the energy transferred to the substrate is small, which results in a low temperature rise of the substrate.

1.1.3 Description of the experimental device for film preparation

All the thin films in this thesis are prepared in the industrial-size reactor (Balzers 640R unit). The deposition system is shown in Fig.1-2, which is mainly constituted by the deposition chamber, vacuum system (primary pump and turbomolecular pump), hardware control unit, gas flow control system, and programming control unit as well as HiPIMS power supply (Hüttinger 4002).

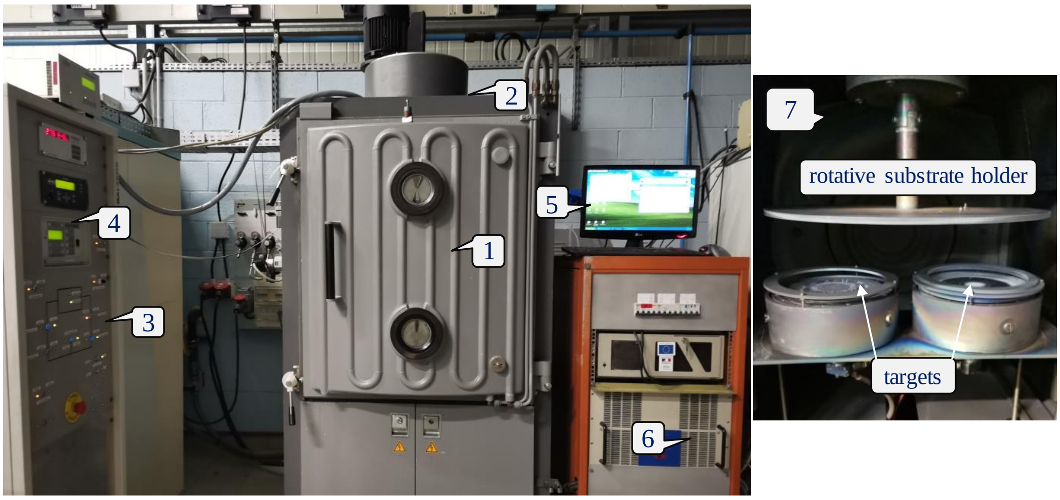

Figure 1-2. HiPIMS deposition system: 1 - deposition chamber, 2 - vacuum system, 3 - hardware control unit, 4 - gas flow control system, 5 - programming control unit, 6 - HiPIMS power supply, 7 - internal deposition chamber with two targets and a rotating substrate holder.

The distribution of two magnetrons and substrate holder inside the deposition chamber is shown in Fig. 1-2 (right). It is possible to install two targets of 150 mm diameter and 8 mm thickness on the unbalanced magnetron cathodes. The distance between the substrate holder and the target surface $D_{t\text{-}s}$ is adjustable and is set to 10 cm in the case of deposited films of this thesis. Moreover, the system allows the bias potential to be applied to the substrate holder.

For the films deposited by HiPIMS, the target is powered by Hüttinger Elektronik 4002 operating in the unipolar mode. The cathode discharge parameters are set to: U = -600 V, I = 2.2 A (average current), t_{on} = 45 μs, f = 500 Hz. The potential of the substrate holder is operated at three modes: floating, -50 V, -100 V bias. The reference films are deposited by DC (Pinnacle Plus, Advanced Energy) with the average current of 2.2 A, $f = 50$ KHz and $T_{off} = 5$ μs. M2 disc substrates (63 HRc, ∅=30 mm × 8 mm), stainless steel slides (40 mm×20 mm×4 mm), silicon wafers (10 mm×10 mm) and iron sheets (400 mm×4 mm×0.25 mm) are selected as the substrates for testing mechanical properties and tribological performance, morphology, chemical bond states, and residual stress of the films. The substrates of M2 and stainless steel are mirror polished with a diamond suspension of 1 μm of granulometry and degreased in ethanol afterward.

Prior to film deposition, the vacuum chamber is pumped down to a base pressure of ∼10^{-4} Pa. The substrates are etched for ten minutes in pure argon atmosphere to remove adventitious contaminants attached to the substrate surface. It is performed by biasing the substrate holder at -700 V, while the target is set at around 2 A average current. Subsequently, a pure metal (Ta or Hf) interlayer of approximately 200 nm thickness is preliminarily deposited between the film and the substrate to improve the film adhesion. During the deposition process, argon (Ar) and acetylene (C_2H_2) are used as working and reaction gases, respectively. The mass flow rate of Ar is kept constant at 200 standard cubic centimeters per minute (sccm) and of C_2H_2 is varied from 10 sccm to 20 sccm with 2 sccm step increments. To obtain homogeneous films, the rotating substrate holder is fixed at the speed of 30 revolutions per minute (r.p.m).

1.2 Characterization of thin films

The description and principle of the HiPIMS technology in the previous section emphasized that the way the thin film is deposited plays an important role in the final structure and performance of the film. This section deals with several characterization methods that have been used in this thesis, which is able to better understand their behavior.

The morphology of the film is observed by Scanning Electron Microscopy (SEM), while the structural characterization of the film is performed by X-Ray Diffraction (XRD). The composition of the film is obtained using an energy dispersive X-ray spectroscopy (EDS) mounted in the SEM. The chemical bonding state of the film is measured by X-ray photoelectron spectroscopy (XPS). The residual stress of the film is measured through the radius of curvature (R) of the film as-deposited on a cantilever beam, which is obtained by the Altysurf profilometer. The mechanical properties, nanohardness and effective Young's modulus, of the film are measured by using the Nanoindentation Tester from CSM Instrument (Switzerland). The tribological performance of the film at room temperature is carried out by pin-on-disk Tribometer from CSM. Finally, the thermal stability and the oxidation resistance of the film are tested by vacuum annealing treatment and annealing treatment under air environment, respectively. The details of each technique are described in the following paragraphs.

1.2.1 Morphological characterization

The surface morphology of the film is observed by Scanning Electron Microscopy (JEOL JSM-7800F) which makes it possible to obtain nanometric resolution. The experimental device photograph of SEM is shown in Fig. 1-3. It is equipped with an energy dispersive X-ray spectroscopy (EDS) detector for estimating the composition of the films. Moreover, in the context of this thesis, SEM (and/or EDS) is used to obtain the transversal cross-sectional morphology of the film (obtained by brittle fracture) to study the type of film growth, the thickness of the film, the degree of oxidation of the film, and the wear track after the tribological test.

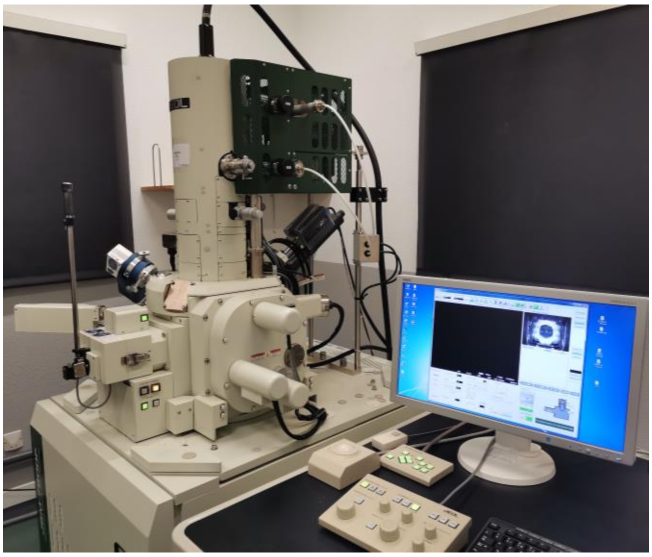

Figure 1-3. The Scanning Electron Microscopy (JEOL JSM-7800F) system.

1.2.2 Structure characterization

The structure of the film is determined by X-ray diffraction (XRD). The equipment used in this thesis is BRUKER D8 focusing diffractometer equipped with a LynxEye linear detector and a Co K_α radiation (λ=1.78897 Å). It works at the current of 40 mA and the voltage of 35 kV. Diffraction patterns in the air are collected in a Bragg-Brentano configuration (θ-2θ) at a scanning speed (2θ) of $0.1°s^{-1}$ in the range of 20 ° to 80 °. The schematic diagram of XRD in $\theta/2\theta$ configuration is shown in Fig. 1-4, and relies on Bragg's law, expressed as [18]:

$$2\ d_{hkl}\ \sin\theta = n\ \lambda, \tag{1-1}$$

in which d_{hkl} is the interplanar distance, θ the incidence angle, λ is the wavelength of the incident beam, and n is an integer.

In addition to the crystalline phase of the film, other information related to the crystalline structure of the films, such as lattice parameter and average grain size, can also be obtained from the diffraction spectra. The lattice parameters can be calculated by Bragg relation from the main diffraction planes. The average grain size can be calculated using the Scherrer's formula [19] from the full width at half maximum (FWHM) of the diffraction peaks:

$$\beta \cos\theta = K\lambda/d_{hkl}, \tag{1-2}$$

where the β is the line broadening at half the maximum intensity (FWHM), after subtracting the instrumental line width, in radians. The θ is the incidence angle in radians and the λ is the incident beam wavelength. The d_{hkl} is the average size of the crystalline domains in the <hkl> direction, which may be smaller or equal to the grain size. The K is the Scherrer constant, which is a dimensionless shape factor, with a value close to unity. The shape factor has a typical value of about 0.89, but varies with the actual shape of the crystallite. Moreover, it should be noted that in this thesis, the total broadening of the FWHM is attributed to the grain size and the strain broadening is ignored.

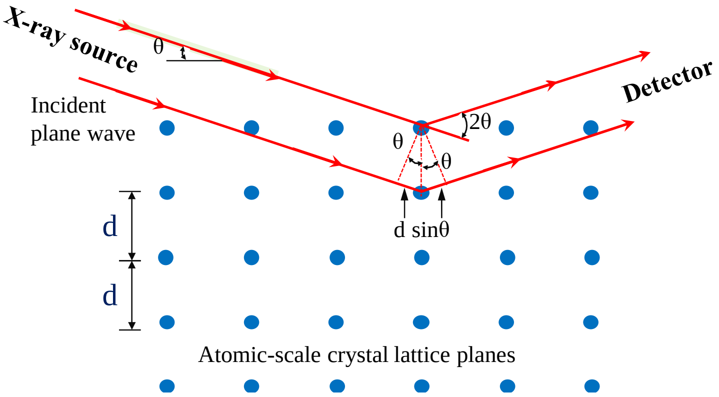

Figure 1-4. Schematic diagram of XRD in θ/2θ configuration, θ is the angle of the incident beam relative to the surface of the sample.

1.2.3 Chemical bonding states characterization

The elemental composition, stoichiometric ratio of crystalline phase, chemical state and electronic state of the elements that exist within the film are analyzed by X-ray photoelectron spectroscopy (XPS) in an attempt to reveal the intrinsic origin of the excellent properties of the films. The working principle of XPS [20] is based upon the photoelectric effect, illustrated in Fig. 1-5.

When a photon from X-ray source impinges the sample surface its energy can be absorbed completely by the electronic cloud of the atoms present in the sample. If the energy is high enough, it causes the sample ionization and the ejection of the so-called photoelectrons with kinetic energy. When these electrons are detected and collected, the XPS spectrum is drawn based on the number of electrons detected and their binding energy. Each element produces a characteristic set of XPS peaks at characteristic binding energy values, which can directly identify each element that exists in or on the surface of the sample being analyzed. These characteristic spectral peaks correspond to the configuration of the electrons within the atoms, e.g., 1s, 2s, 2p, 3s, etc.

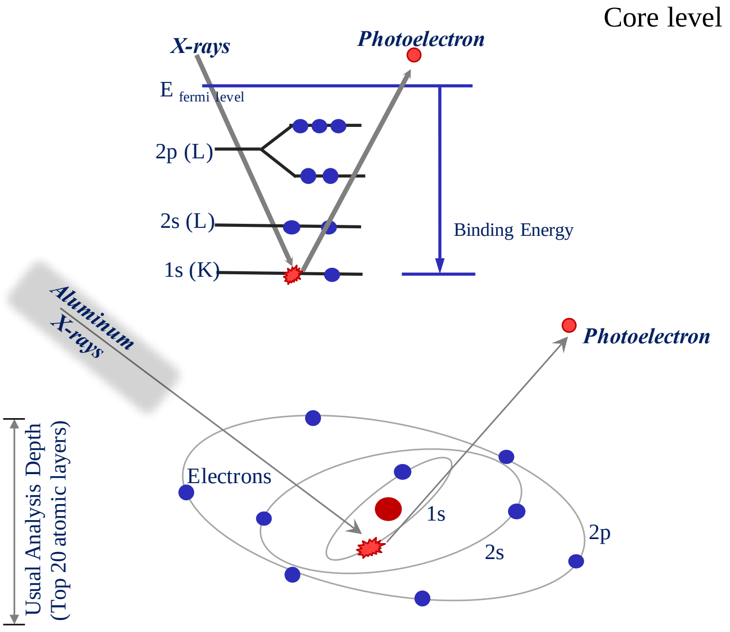

Figure 1-5. Schematic of XPS physics-Photoelectric Effect.

In this thesis, the XPS measurement is performed under the ultra-high vacuum (~10^{-8} Pa) with aluminum Kα monochromatized radiation at the 1486.7 eV X-ray photon source. The measurements are performed in constant analyzer energy mode with a 50 eV pass energy for high resolution spectra. Charge calibration is performed by setting the binding energy of the C 1s photoelectron peak to 285 eV. The films are analyzed with a 45 ° take-off angle. The samples are previously cleaned by 0.5 keV Ar ion bombardment before XPS measurement to preferentially remove the hydrocarbon surface contamination layer without affecting the film's elemental composition. The Shirley background subtraction procedure is performed to subtract the XPS background spectra stemming from electron inelastic scattering. The fitting analysis is conducted by using a Gaussian with a Lorentzian mix function on the C 1s of the film to estimate the relative content of different carbon bonds (i.e., metal carbide and amorphous carbon).

1.2.4 Measurement of the film residual stress

In the thesis, the residual stress is measured on the thin film deposited on the iron sheet, of which dimension is 400 mm × 4 mm × 0.25 mm. Prior to film deposition, the substrate of the iron sheet is annealed to remove stress and keep the curvature of the substrate to zero to avoid introducing errors in the measurement of the curvature of the film.

After film deposition, the radius of curvature (R) of the as-deposited film is measured by the Altysurf profilometer equipped with the optical probe. Based on the curvature, the residual stress inside the film is thus calculated according to the simplified Stoney formula [21]:

$$\sigma = \frac{E_s}{6(1-\upsilon_s)}\frac{d_s^2}{d_f}\frac{1}{R} \tag{1-3}$$

in which E_s, d_s and υ_s represent Young's modulus, thickness and Poisson's ratio of the substrate, respectively. d_f stands for the thickness of the film.

1.3 Properties of thin films

1.3.1 Measurement of the film mechanical properties

The nanohardness H and effective Young's modulus E^* of the films are carried out by the Nanoindentation Tester (applied load is 5 mN) from CSM Instruments using the continuous stiffness measurement method, equipped with a Berkovich diamond indenter tip at room temperature. The measuring principle is to press the Berkovich tip which has a three-sided pyramid geometry into a sample. The load placed on the indenter tip is increased as the tip penetrates further into the film and soon reaches a user-defined value. During the indentation, the penetration depth is recorded and the area of the indentation is determined using the known geometry of the Berkovich tip.

While indenting, various parameters such as load and depth of penetration can also be recorded. The record of these values can be used to create a load-displacement curve, such as the one shown in Fig. 1-6 (referenced from [23]). Based on such a curve, the mechanical properties of the film can be extracted.

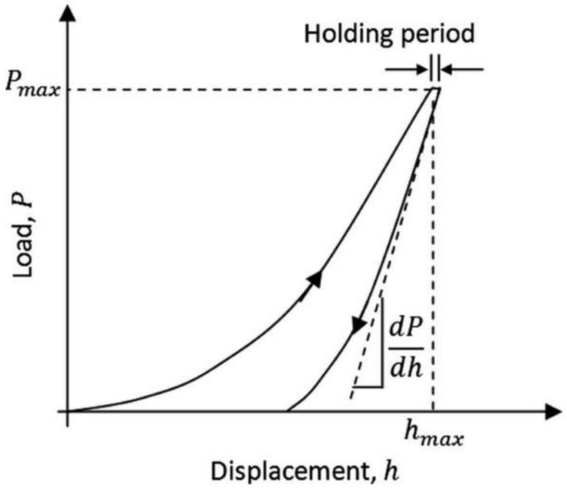

Figure 1-6. Schematic of the load-displacement curve for instrumented nanoindentation test.

In the case of the films in this thesis, prior to the measurement, the contact area function is calibrated using a standard fused silica material. The values of hardness and effective Young's modulus are calculated from the average of twelve load/unload curves performed for each sample and determined based on the Oliver-Pharr model [22]. In order to eliminate the substrate effect, the indentation depth is kept less than 10% of the film thickness during measurement.

1.3.2 Measurement of the film tribological performance

The tribological performance of the films is carried out by a pin-on-disk Tribometer from CSM (Switzerland). All pin-on-disk measurements are conducted via unlubricated sliding against 6 mm WC/Co balls in ambient air at a relative humidity of about 40% - 45%. For the TaC/a-C:H films in Chapter 3 whose tribological properties have been measured, the test parameters are set to 5 N applied normal load, 1.6 cm/s sliding speed, 3 mm contact track radius and 10000 sliding laps. For the HfC/a-C:H films investigated in Chapter 4, the test parameters are set to 5 N applied normal load, 5 cm/s sliding speed, 3 mm contact track radius and 10000 sliding laps. After the tribology tests, the cross-sectional profiles of wear tracks are characterized by using Altysurf profilometer equipped with the inductive probe. The wear rates (W_r) are calculated using the equation:

$$W_r = V/(L \times S), \tag{1-4}$$

where V is the wear volume of the films, L is the applied normal load, and S is the sliding distance. The surfaces of wear tracks of the films are observed via SEM/EDS.

1.3.3 Measurement of film thermal stability and oxidation resistance

The thermal stability of the film is investigated by the vacuum annealing treatment at different temperatures (from 200 °C up to 800 °C with an incremental step of 100 °C) in the resistively heated laboratory vacuum furnace. Before annealing treatment, the furnace chamber is evacuated to the pressure of about 10^{-4} Pa. During annealing treatment, the heating rate is 200 °C/h, and after achieving the desired temperature the holding period is set to 2 h. Following, all samples are cooled in vacuum until room temperature is reached.

The oxidation resistance of the film is performed under air atmosphere at different temperatures (from 200 °C up to 700 °C with an incremental step of 100 °C, with a heating rate of 100 °C/h) in the furnace of Nabertherm with a dwell time of 2 h. Subsequently, all films experienced a natural cooling process. The oxidation degree of the film after annealing was measured by XRD, SEM, and EDS.

1.4 Conclusion

In this chapter, the experimental procedures used during the thesis are described. Two main sections have been presented, dedicated to the synthesis and characterization of the films. In the first section, the basic concepts of the HiPIMS technique are given, with a special focus put on the principle of HiPIMS deposition. All experimental parameters for the deposition of the nanocomposite films involved in this thesis using HiPIMS and DC power supplies are elucidated. In the second part, according to the target performance, several characterization methods required for the nanocomposite films are introduced. The primary features of the films that have to be conducted are the chemical composition (XPS, EDS), the nature of crystalline phase (XRD) as well as the morphology (SEM). The measurement methods and parameters of the properties, including mechanical properties, tribological performance, oxidation resistance, and thermal stability, are fully presented.

1.5 References

[1] Gudmundsson, J. T., Brenning, N., Lundin, D., & Helmersson, U. (2012). High power impulse magnetron sputtering discharge. Journal of Vacuum Science & Technology A: Vacuum, Surfaces, and Films, 30(3), 030801.

[2] Anders, A. (2011). Discharge physics of high power impulse magnetron sputtering. Surface and Coatings Technology, 205, S1-S9.

[3] Helmersson, U., Lattemann, M., Bohlmark, J., Ehiasarian, A. P., & Gudmundsson, J. T. (2006). Ionized physical vapor deposition (IPVD): A review of technology and applications. Thin solid films, 513(1-2), 1-24.

[4] Gudmundsson, J. T. (2008). Ionized physical vapor deposition (IPVD): magnetron sputtering discharges. In Journal of Physics: Conference Series (Vol. 100, No. 8, p. 082002). IOP Publishing.

[5] Kouznetsov, V., Macak, K., Schneider, J. M., Helmersson, U., & Petrov, I. (1999). A novel pulsed magnetron sputter technique utilizing very high target power densities. Surface and coatings technology, 122(2-3), 290-293.

[6] Macák, K., Kouznetsov, V., Schneider, J., Helmersson, U., & Petrov, I. (2000). Ionized sputter deposition using an extremely high plasma density pulsed magnetron discharge. Journal of Vacuum Science & Technology A: Vacuum, Surfaces, and Films, 18(4), 1533-1537.

[7] Sellers, J. (1998). Asymmetric bipolar pulsed DC: the enabling technology for reactive PVD. Surface and Coatings Technology, 98(1-3), 1245-1250.

[8] Kelly, P. J., Henderson, P. S., Arnell, R. D., Roche, G. A., & Carter, D. (2000). Reactive pulsed magnetron sputtering process for alumina films. Journal of Vacuum Science & Technology A: Vacuum, Surfaces, and Films, 18(6), 2890-2896.

[9] Helmersson, U., Lattemann, M., Alami, J., Bohlmark, J., Ehiasarian, A. P., & Gudmundsson, J. T. (2005). 48th Annual Technical Conference Proceedings. Denver, CO, 23-28.

[10] Sarakinos, K., Alami, J., & Konstantinidis, S. (2010). High power pulsed magnetron sputtering: A review on scientific and engineering state of the art. Surface and Coatings Technology, 204(11), 1661-1684.

[11] Bohlmark, J., Lattemann, M., Gudmundsson, J. T., Ehiasarian, A. P., Gonzalvo, Y. A., Brenning, N., & Helmersson, U. (2006). The ion energy distributions and ion flux composition from a high power impulse magnetron sputtering discharge. Thin Solid Films, 515(4), 1522-1526.

[12] Huo, C., Raadu, M. A., Lundin, D., Gudmundsson, J. T., Anders, A., & Brenning, N. (2012). Gas rarefaction and the time evolution of long high-power impulse magnetron sputtering pulses. Plasma Sources Science and Technology, 21(4), 045004.

[13] Lundin, D., & Sarakinos, K. (2012). An introduction to thin film processing using high-power impulse magnetron sputtering. Journal of Materials Research, 27(5), 780-792.

[14] Alami, J., Bolz, S., & Sarakinos, K. (2009). High power pulsed magnetron sputtering: Fundamentals and applications. Journal of Alloys and Compounds, 483(1-2), 530-534.

[15] Anders, A., Ni, P., Rauch, A. (2012). Drifting localization of ionization runaway: Unraveling the nature of anomalous transport in high power impulse magnetron sputtering. Journal of Applied Physics, 111(5), 053304.

[16] Brenning, N., Lundin, D., Minea, T., Costin, C., & Vitelaru, C. (2013). Spokes and charged particle transport in HiPIMS magnetrons. Journal of Physics D: Applied Physics, 46(8), 084005.

[17] Cavalier, J., Lemoine, N., Bonhomme, G., Tsikata, S., Honoré, C., & Gresillon, D. (2013). Hall thruster plasma fluctuations identified as the E× B electron drift instability: Modeling and fitting on experimental data. Physics of Plasmas, 20(8), 082107.

[18] K. Liu, T.A. Schmedake, R. Tsu, "A comparative study of colloidal silica soheres: Photonic crystals versus Bragg's low", Physics Letters A 372 (2008) 4517-4520.

[19] P. Scherrer, "Bestimmung der grosse und der inneren struktur von kolloidteilchen mittels rontgenstrahlen, nachrichten von der gesellschaft der wissenschaften, gottingen", Mathematisch-Physikalische Klasse 2 (1918) 98-100.

[20] Moulder, J. F. (1995). Handbook of X-ray photoelectron spectroscopy. Physical electronics, 230-232.

[21] I. Ivanov, P. Kazansky, L. Hultman, I. Petrov, J. E. Sundgren, Influence of an external axial magnetic field on the plasma characteristics and deposition conditions during direct current planar magnetron sputtering, J. Vac. Sci. Technol. A 12 (1994) 314-320.

[22] W. C. Oliver, G. M. Pharr, An improved technique for determining hardness and elastic modulus using load and displacement sensing indentation experiments, J. Mater. Res. 7 (1992) 1564-1583.

[23] Voyiadjis, G. Z., & Almasri, A. H. (2009). Variable material length scale associated with nanoindentation experiments. Journal of engineering mechanics, 135(3), 139-148.

Chapter 2 The spoke origin based on the coupling-induced wave model in HiPIMS plasma

Spokes, identified as the source of anomalous across-**B** field transport during the HiPIMS discharge, have been considered as a result of plasma instability. Based on this cognition, the purpose of this chapter is to derive a dispersion relationship suitable for describing the plasma characteristics during HiPIMS discharge, and to investigate the evolution of the coupling between two azimuthal waves in the plasma. Inspired by the coupling evolution between two azimuthal waves, the coupling-induced wave model is proposed for the origin of the spoke in this chapter. Based on the proposed model, the characteristics of the spoke, such as rotating velocity, frequency, and dynamic features, are predicted and compared with the experimental phenomena and simulation results from the literature. In addition, the evolutions of spoke behavior following from the model are presented, including rotating velocity and mode number along the racetrack.

2.1 Research background and purpose

In HiPIMS device, the orthogonal electric and magnetic field configuration in front of the target surface and the high power density delivered during the short pulses with low duty cycle significantly increase the plasma density and ionization rate of the sputtered target atoms. This generated high plasma density and high ionization fraction allows better control of the film growth by tunning the energy and direction of the deposition species. Accordingly, the structure, morphology and properties of the film can be further modulated to meet the different needs of industrial applications. It is the significant advantage for HiPIMS over conventional DC magnetron sputtering where the sputtered vapor consists mainly of neutral atoms. Therefore, numerous studies have been devoted to HiPIMS-related research, but most of them focus on the research of films prepared by HiPIMS, and are rarely devoted to the investigation of the HiPIMS plasma [1][2][3].

One of the most remarkable phenomena has arguably been the occurrence of the long-scale localized structure, spoke. It is observed as a centimeter scale wavelength high density coherent structure rotating in azimuthal direction ($\mathbf{E}\times\mathbf{B}$ direction) with different mode number. Ehiasarian *et al.* [4] observed the well-defined region of high plasma light emission along the racetrack of magnetron discharge. Anders *et al.* [5] and Winter *et al.* [6] also observed the same high density local structures. Recent measurements [7][8][9] in HiPIMS have unambiguously confirmed that the spoke is the main source of anomalous transport (across the magnetic field toward substrate) that greatly influences the deposition process of HiPIMS plasma. Hecimovic [7] revealed that the ions from the spokes are diffusing away toward the substrate and the ion diffusion coefficients are six times higher than the Bohm diffusion coefficient. Anders *et al.* [8] and Kozyrev, *et al.* [9] showed that the plasma is ejected from the spokes toward the anode. Besides, it was shown that the formation of such plasma inhomogeneities (spokes) is caused by the necessity to transfer high density electron current across the magnetic field toward substrate [9].

Based on the above experimental evidence, the understanding of the spoke nature becomes crucial, and it can be the key to explain anomalous transport across the magnetic field in HiPIMS plasmas. In particular, such anomalous transport has great potential in increasing the low deposition rate which is the current challenge that HiPIMS technology faces in industrial applications. Moreover, the velocity of anomalous transport is important for the quality of thin film.

Some researchers have considered that the spoke is likely the result of plasma instability because any highly ionized plasma is extremely susceptible to develop. Ehiasarian *et al.* [4] explained that the spoke is likely to be the generalized drift wave instability. Brenning *et al.* [10] postulated that the spoke velocities are correlated with the Critical Ionization Velocity that is referred to as “CIV” in many studies of fundamental plasma science. While several other works have investigated the spoke phenomenon in HiPIMS, as well as the dynamic characteristics of the spoke, the physical nature or the origin of the spoke still remain currently ambiguous.

2.2 The coupling-induced wave model

2.2.1 Analysis of azimuthal waves and their interaction

The general configuration of HiPIMS discharge is shown in Fig. 2-1. The magnetic field is taken radial, $\mathbf{B} = \mathrm{B}\hat{z}$, and the applied electric field is along the axial direction, $\mathbf{E} = \mathrm{E}\hat{x}$. The plasma is confined in the ionization region above the target surface by such electromagnetic field configuration. Let us consider this HiPIMS two-component plasma, consisting of the ions and electrons immersed in the strong magnetic field, such that on the scale of the HiPIMS device electrons are magnetized, while the ions are unmagnetized and controlled by the equilibrium and perturbation potential distributions. Therefore, during plasma discharge, large discharge current between the sputtering cathode and the anode is generated. Furthermore, large azimuthal current, circulating in the magnetic field trap close to the magnetron, arises because of the presence of the magnetic field through a combination of diamagnetic and $\mathbf{E}\times\mathbf{B}$ drifts of electrons. Due to the high ionization rate of HiPIMS and quasineutrality condition, the electron drift in the azimuthal direction necessarily imposes a force on the ions through the Coulombic force. Therefore, the azimuthal motion of the plasma actually corresponds to the relative drift of ions and electrons, and it is expected that the mutual constraints and collective effects between electrons and ions are closely related to the observed spokes. Therefore, the analysis of the origin of the spoke must start with the motion of electrons and ions in the azimuthal direction.

The electron drift with the velocity of $\mathbf{V_d} = \mathbf{E}\times\mathbf{B}/\mathrm{B}^2$ is in azimuthal direction which stands for $-\mathrm{y}$ in the following. Based on the non-magnetized nature of the ions, the ions are considered cold since they cannot be accelerated and thus gain energy in the azimuthal direction. The temperature of the electron is assumed to be $\mathrm{T_e}$. In the ionization region, since the perturbation magnetic field caused by plasma is very weak, its effect is ignored. Besides, the value of magnetic pressure β_e ($\beta_e = n_e k T_e / (B^2/2\mu_0)$)

is 7.8×10^{-3}. The values of the plasma parameters n_e, T_e and B for the calculation of β_e are from Table 2-1. For plasma with low β_e value, the plasma instabilities excited by the density gradient and magnetic field gradient can be ignored [11]. The temperature anisotropy usually leads to unstable transverse waves with smaller growth rates. Thus, we consider that the source of free energy for plasma instabilities only comes from the electron $\mathbf{E}\times\mathbf{B}$ drift.

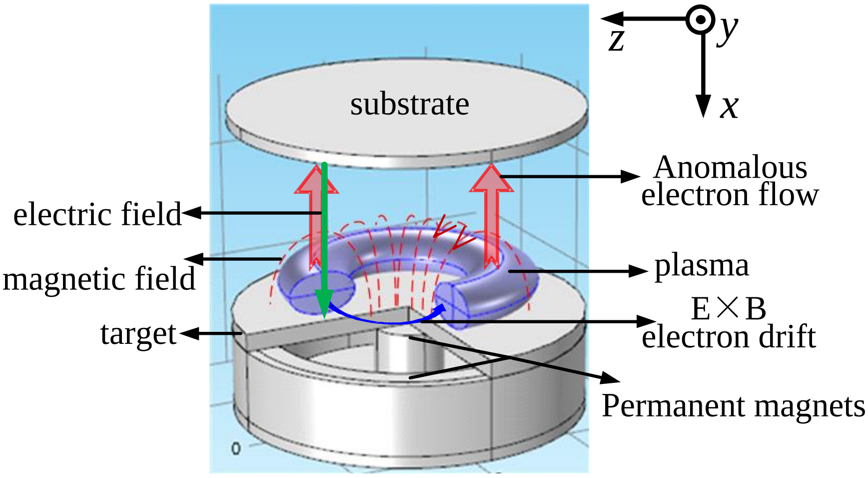

Figure 2-1. The three-dimensional diagram of HiPIMS discharge.

Brenning, N. *et al.* [12] have experimentally confirmed that the anomalous transport toward the substrate is not enough to be explained by the classical collision theory. Moreover, the strong plasma fluctuations that enhance the anomalous electron transport across the magnetic field can be observed in the absence of electron-neutral collisions [13]. Hence, it is reasonable that there is a non-collision mechanism in the HiPIMS as the main cause for forming spoke, although the collisional processes are still important in maintaining the plasma and leading to huge discharge current ($>100\,\mathrm{A}$). Thus, the plasma behavior in HiPIMS ionization region can be effectively considered as the consequence of the interaction of non-collisional waves in the azimuthal direction. Given the above, we focus on the situation where the ions are cold and unmagnetized, the electrons are magnetized, the free energy only derives from electron $\mathbf{E}\times\mathbf{B}$ drift, and the plasma behavior is the consequence of the interaction between non-collisional azimuthal waves.

The interaction of the plasma waves can be analyzed *via* dispersion relation, namely the wavenumber (k_y) and the frequency (ω) matching. In this chapter, the derivation and analysis of the dispersion relation are based on the hybrid model, in which the ion motion is described by the cold fluid model and the electron motion is described by the kinetic model. The ion movement described by the cold fluid equations is written as:

$$\begin{gathered}\frac{\partial n_{i0}}{\partial t}+\nabla\cdot n_{i0}v_i=0\\ M(\frac{\partial}{\partial t}+v_i\cdot\nabla)=-e\nabla\Phi\end{gathered}\quad,\qquad (2\text{-}1)$$

where n_{i0} and v_i are the equilibrium ion density and equilibrium ion velocity, respectively, e is the ionic charge, M is the ion mass and Φ is the plasma equilibrium potential. Linearizing and resolving Eq. (2-1) in order to find the perturbed density of ions, then we obtain

$$n_{i1}=\frac{k_y^2 e n_{i0}\Phi}{\omega^2 M},\qquad (2\text{-}2)$$

in which k_y is the wavenumber along the azimuthal direction. Accordingly, the ion density perturbation (*i.e.*, ion contribution) in HiPIMS plasma can be expressed as:

$$n_{i1}=\frac{k_y^2 e n_{i0}\Phi}{\omega^2 M}=\frac{k_y^2 C_s^2}{\omega^2}\frac{e\Phi}{T_e}n_{i0},\qquad (2\text{-}3)$$

in which C_s the ion sound velocity and e is the electronic charge. Since the ions are unmagnetized that allow the existence and propagation of ion sound wave in the azimuthal direction.

Next, the ion density perturbation n_{i1} and the electron drift $k_y V_d$ are considered into the dispersion relation of the electron Bernstein wave [14] described by the kinetic model. Thus the dispersion relation for azimuthal wave of $E_y \sim \exp(ik_y y - i\omega t)$ can be deduced as:

$$k_y^2\lambda_D^2 = -1 + I_0(b)e^{-b} + \sum_{n=1}^{+\infty} \frac{2(\omega - k_y V_d)^2 I_n(b)e^{-b}}{(\omega - k_y V_d)^2 - (n\omega_{ce})^2} + \frac{k_y^2 C_s^2}{\omega^2}, \tag{2-4}$$

where V_d is the velocity of the electron $\mathbf{E}\times\mathbf{B}$ drift along the azimuthal direction, ω_{ce} is the electron cyclotron frequency, and λ_D is the Debye length. The functions I_n are n-order modified Bessel functions and $b = k_y^2 r_e^2$ (r_e is the electron Larmor radius). The solution of the dispersion relation Eq. (2-4) has been investigated numerically in [15][16][17]. However, we do not analyze the variations of frequency and growth rate under the different plasma discharge parameters as many authors had investigated. The contribution of our study focuses on the dispersion characteristics and subsequent evolution results of the Eq. (2-4) adapted to HiPIMS plasma.

The short wavelength regime of the electronic oscillation, $k_y^2 r_e^2 > 1$, is very prone to occur in the HiPIMS discharge. Under this limit $k_y^2 r_e^2 > 1$, the values of the terms $I_n(b)e^{-b}$ for all $n = 2, 3, \cdots$ are much smaller than 1 except for the first term n=1, since the value of $k_y^2 r_e^2$ is slightly greater than 1. Moreover, with the evolution of azimuthal instabilities, the cyclotron harmonic for exciting the linear azimuthal instabilities will shift downward due to the increase in electron temperature [18]. Recent literature [19] also emphasized that, through numerical simulations, the azimuthal instabilities proceed by developing a large coherent wave are driven by the free energy input from the fundamental cyclotron component n=1. Therefore, it is reasonable to only consider the case of n=1, the dispersion relation Eq. (2-4) can then be simplified as:

$$1 + k_y^2\lambda_D^2 - I_0(b)e^{-b} - \frac{k_y^2 C_s^2}{\omega^2} - \frac{2(\omega - k_y V_d)^2 I_1(b)e^{-b}}{(\omega - k_y V_d)^2 - \omega_{ce}^2} = 0. \tag{2-5}$$

Finally, the dispersion relationship Eq. (2-5) for clearly describing the propagation characteristics of the waves of HiPIMS plasma in the azimuth direction is obtained.

We are particularly concerned with two types of azimuthal waves that propagate along the $-y$ direction. One is the Doppler-shifted electron Bernstein (DSEB) wave [14]:

$$\omega_1 = k_y V_d - \sqrt{1+2\Delta}\omega_{ce} \tag{2-6}$$

where

$$\Delta = \frac{I_1(b)e^{-b}}{1+k_y^2\lambda_D^2 - I_0(b)e^{-b}} . \tag{2-7}$$

Another is the ion sound (IS) wave [20]:

$$\omega_2 = \frac{k_y C_s}{\sqrt{1+k_y^2\lambda_D^2}} . \tag{2-8}$$

In order to verify the accuracy of the proposed model, the experiment from Tsikata, S. *et al.* [21] are selected to compare. Their experimental values are given in Table 2-1 and are injected into the dispersion relationship Eq. (2-5) as typical HiPIMS parameters. It should be note that the magnetic field strength here is weaker than that of the general magnetron since the observation position in [21] is not tightly close to the target.

Table 2-1. Overview of parameters and the quantitative values adopted used to validate the coupling-induced wave model, from the HiPIMS plasma discharge in [21].

Symbol	Parameter	Value adopted
E	Mean electric field	10^4 V/m
B	Magnetic field strength	8.8 mT
V_d	Electron drift velocity	1×10^6 m/s
V_{the}	Electron thermal velocity	7×10^5 m/s
n_e	Plasma density	10^{18} m^{-3}
r_e	Electron Larmor radius	5×10^{-4} m
λ_D	Debye length	9×10^{-6} m
ω_{ce}	Electron cyclotron frequency	1.6×10^9 rad/s

Based on above experimental parameters, the numerical solution of the dispersion relation Eq.(2-5) is obtained by applying Lagrangian order reduction method [22]. The solution with positive imaginary part is selected. Its real part (frequency) and imaginary part (growth rate) are plotted in Fig. 2-2 as a function of azimuthal wavenumber k_y . Meanwhile, ω_1 and ω_2 are also plotted in Fig. 2-2 in order to explore the relationship between azimuthal waves and eigensolution of dispersion relation.

It can be clearly seen that the frequency begins at $k_{ys} = \omega_{ce} / V_d$ ($= 1389 \text{ rad/m}$) where the frequency value is very small. Then the frequency reaches maximum value at the wavenumber k_{ym} ($k_{ym} = 2581 \text{rad/m}$) where is close to the intersection of the DSEB (ω_1 – red dash line) wave and the IS (ω_2 – green dot line) wave, as shown in the inset of Fig. 2-2. Therefore, it is confirmed that the ECD instability originates from the coupling of the DSEB wave and IS wave in HiPIMS plasma. This condition is similar to the ion cyclotron drift instability [23].

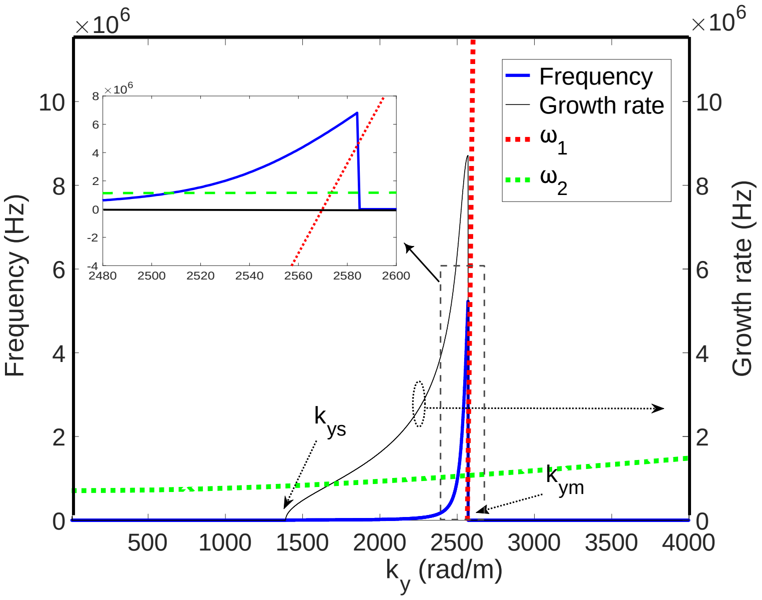

Figure 2-2. Frequency and growth rate as a function of wavenumber together with ω_1 and ω_2. The detail of the intersection region of ω_1 and ω_2 is shown in the inset.

As we further focus on the dispersion characteristic of frequency curve (the blue line, Fig. 2-2 – inset), two other new findings rise up.

(i) The first one concerns the most unstable wavenumber k_{ym} (*i.e.*, the wavenumber of maximum growth rate) and it can be determined very accurately since it obeys the resonance condition between DSEB wave and IS wave:

$$k_{ym}V_d - \sqrt{1+2\Delta}\omega_{ce} \approx \frac{k_{ym}C_s}{\sqrt{1+k_{ym}^2\lambda_D^2}} . \tag{2-9}$$

From Eq. (2-9), it comes that k_{ym} ($k_{ym} = 2581\,\mathrm{rad/m}$) is not close to the value of ω_{ce}/V_d ($=1389\,\mathrm{rad/m}$) which was generally considered as the excitation wavenumber of maximum growth rate for ECD instability [15][17]. In addition, this wavenumber does indicate the lower limits of the simulation box size which is very important for modeling the evolution of narrow spectrum instabilities through particle-in-cell (PIC) method [15][24].

(ii) The second finding is that the shape of the frequency curve is concave over the interval $k_{ys} < k_y < k_{ym}$. The slope of the connecting line from the origin to any point on frequency curve ($\omega(k)/k$) is less than the slope of the tangent at that point ($\partial\omega(k)/\partial k$). That is to say, the phase velocity of the unstable wave propagating in the HiPIMS plasma is smaller than the group velocity. It marks that the plasma exhibits anomalous dispersion characteristic during the azimuthal wave motion [25][26].

2.2.2 Establishment of Coupling-induced wave model

Let us consider the spokes, the well-identified plasma structures, characterized by propagation velocity and regular size (space-scale), as a manifestation of the coupling of DSEB wave and IS wave. The coupling evolution of the DSEB wave and IS wave along the azimuthal direction is analyzed in this section. It should be emphasized that the linear coupling approach is used in our model. Generally, when one considers the coupling of two waves in a dispersive medium, the second-order terms produce a nonlinear amplitude effect [27]. This nonlinear amplitude term acts as a distortion on the modulated wave amplitude during its propagation. In HiPIMS discharge, the effect of nonlinear amplitude term generated by the wave coupling is closely related to electron heating. Since the purpose of this study is to evoke an explanation for the spoke origin, its eventual consequences, such as electron heating, are not discussed here. Therefore, the linear coupling processing method is adopted.

The form of the perturbed electric field of DSEB wave is $E_1(y,t) \sim \cos(k_{y1}y - \omega_1 t)$ and of IS wave is $E_2(y,t) \sim \cos(k_{y2}y - \omega_2 t)$. The coupling occurs when the frequencies (and wavenumbers) of both waves are close to each other. It should be noted here that we do not study the case in which the frequencies of two waves are exactly equal, which leads to $\gamma_i \to \infty$ (γ_i is the growth rate) due to the intense resonance. This infinity growth rate is beyond the scope of linear analysis.

When the frequencies of the DSEB and IS waves are close, a new coupled wave is generated, and its perturbed electric field form can be expressed by

$$E(y,t) \sim \cos'(\frac{\Delta k_y}{2} y - \frac{\Delta\omega}{2} t)\cos(\frac{k_{y1}+k_{y2}}{2} y - \frac{\omega_1+\omega_2}{2} t) \tag{2-10}$$

where $\Delta k_y = k_{y1} - k_{y2}$ and $\Delta\omega = \omega_1 - \omega_2$. The form of the perturbed field (Eq. (2-10)) of coupled wave presents two components that correspond to two perturbed electric oscillations in the azimuthal direction. One is the $\cos$ term, defined as the sum frequency (SF) wave, moving with the phase velocity of the coupled wave $v_p = (\omega_1+\omega_2)/(k_{y1}+k_{y2})$. The other is the $\cos'$ term, defined as the difference frequency (DF) wave, and its velocity is the group velocity of the coupled wave $v_g = \Delta\omega/\Delta k_y$. Since the plasma exhibits anomalous dispersion characteristics, as proposed in the second finding (ii - section 2.1), the propagation velocity of DF wave is faster than that of SF wave.

For the sake of clarity, Fig. 2-3 shows the phase velocity v_p and group velocity v_g as a function of k_y. It can be seen that, in the vicinity of k_{ym}, the propagation velocity of DF wave is about 10^5 m/s which is one-tenth of the $\mathbf{E}\times\mathbf{B}$ drift velocity (Table 2-1). The propagation velocity of SF wave is about 3×10^3 m/s, which is slightly higher than the ion sound velocity $C_s = 1.9\times10^3$ m/s.

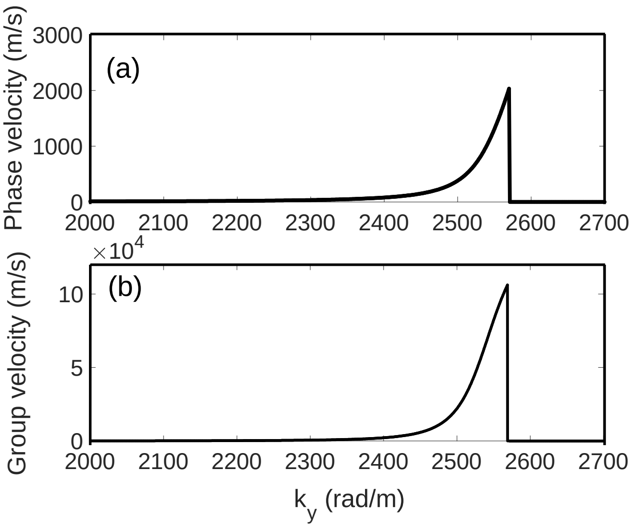

Figure 2-3. (a) Phase velocity and (b) group velocity as a function of wavenumber of the coupling wave, Eq. (2-10).

Indeed, in the range $k_{ys} < k_y < k_{ym}$ where the azimuthal instability occurs, multiple wave solutions of DSEB and IS waves co-exist and their frequencies and wavenumbers are close. However, regardless of how many wave solutions interact within $k_{ys} < k_y < k_{ym}$, their coupling results in only DF and SF components, no other macroscopically recorded oscillations are produced. If the macroscopic spoke (DF component) arises as a result of waves' interactions, they should have the same characteristics (*i.e.*, group velocity and wavelength), and whatever the waves that couple to each-other are, the result should yield the same manifestation of the plasma structure [28]. Moreover, the characteristics (wavenumber, propagation velocity) of the SF components are close, independent of the number of waves contributing to them, since the multiple wave solutions participating in the coupling have close wavenumbers and frequencies. It should be noted that in the case of multiple wave solutions coupling, the amplitude of the DF component would be enhanced, but its frequency and wavenumber are not affected. Therefore, the coupling of any two wave solutions of Eqs. (2-4) and (2-6) can be representative of the interaction of DSEB and IS waves. In the present work, we conduct our analysis on the two wave solutions and their coupling.

In the range of wavenumber $k_{ys} < k_y < k_{ym}$, we choose k_{y1}=2576 rad/m for

DSEB wave as a case to analyze the characteristics of frequency and wavenumber for the coupled wave Eq. (2-10). At $k_{y1}=2576\ \mathrm{rad/m}$, the $\omega_1 \approx 1.5\times 10^6\ \mathrm{Hz}$ can be obtained from Eqs. (2-6) and (2-7). The values of $v_p = 3\,\mathrm{km/s}$ and $v_g = 94\,\mathrm{km/s}$ are obtained from Fig. 2-3. Therefore, the $k_{y2} = 2537\,\mathrm{rad/m}$ and $\omega_2 \approx 1\times 10^6\ \mathrm{Hz}$ can be further calculated respectively based on the relations of $v_p = (\omega_1 + \omega_2)/(k_{y1} + k_{y2})$ and $v_g = (\omega_1 - \omega_2)/(k_{y1} - k_{y2})$. In the same way, when other values of k_{y1} within the range $k_{ys} < k_y < k_{ym}$ are selected, similar results of ω_1, ω_2, k_{y1}, and k_{y2} can also be obtained.

Based on above values, the electric field distributions of the coupled wave of Eq. (2-10) along the complete unfolding circular path of electron drift L (with a radius of $3\mathrm{cm}$) are plotted, as shown in Fig. 2-4. The top one represents the coupled wave in which the red wave trace corresponds to the DF wave and the blue high-frequency oscillation corresponds to the SF wave. For the detailed study, DF and SF waves are decomposed from the coupled waves and are displayed as the middle one and the bottom one, respectively.

In Fig. 2-4, the frequency of DF wave is $3\times 10^5\,\mathrm{Hz}$ and the frequency of SF wave is $1.2\times 10^6\,\mathrm{Hz}$. The wavenumber of DF wave is $19\,\mathrm{rad/m}$ and the wavenumber of SF wave is $2556\,\mathrm{rad/m}$. Consequently, the DF wave has a cm-scale wavelength of about 5.3 cm while the SF wave has a mm-scale wavelength of about 0.4 mm. The wavelength of DF wave is more than one order of magnitude of SF wave. The emergence of such long-wavelength DF wave has a remarkable significance since it means a long-scale electric field oscillation corresponding to the DF wave appears during the two waves coupling of DSEB and IS.

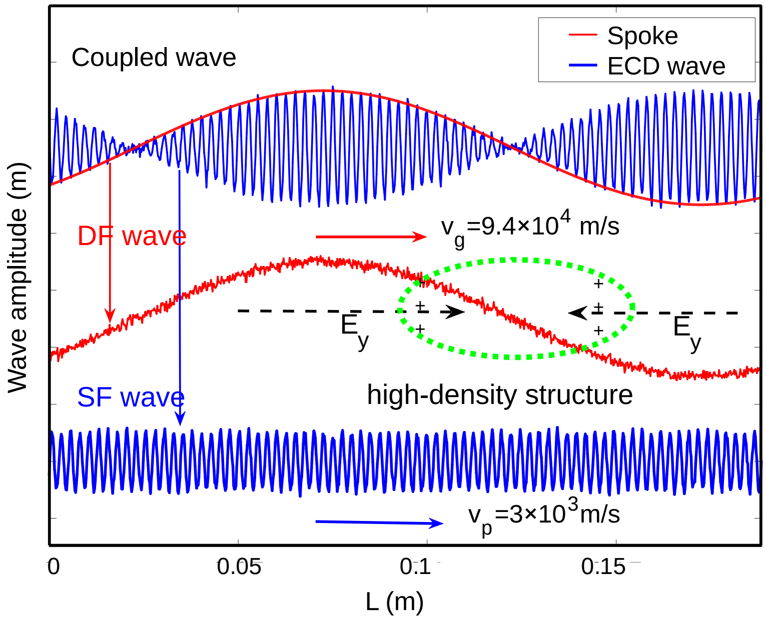

Figure 2-4. The electric field distributions for the DF wave (red middle) and SF wave (blue bottom) against the complete unfolding track of $\mathbf{E} \times \mathbf{B}$ drift, at $\mathrm{t} = 1.4\ \mu\mathrm{s}$. Coupled wave is shown in the upper part.

Comparing to the experimental measurements in [21], the frequency and wavelength of the DF wave deduced from our model is close to the low modulation frequency which is related to the spoke. The frequency, velocity, and wavelength of SF wave from our model are well consistent with those of azimuthal mode which is identified as the ECD instability. The difference between our theoretical results and measurements of [21] is that the dispersion relation of their observed wave is non-discrete. Several possible reasons can be incriminated for this discrepancy. In the proposed model, (i) the magnetic field is considered only along the *z*-axis, while in the real case it is bent in (*x*, *z*) plane. (ii) The radial wavenumber, which results in a smoothing out of the discrete resonances, is not considered. (iii) In the non-linear regime, turbulence can also smooth out the discrete resonances, leading to a transition to the ion acoustic instability.

Due to the long-scale modulation of the electric field $\mathrm{E_y}$ of the DF wave, the plasma ions rearrange themselves and form a long scale (about 5.3 cm) local high density structure at the position of the phase change (the electric field directions point toward each other) of DF wave, marked by the green dotted area in Fig. 2-4. The internal electric field distribution of this high density structure, points to the structure center, is similar to that of spoke in simulation [29].

With the gradual accumulation of ions at the position of the high density structure under the action of the electric field of DF wave E_y, the local electric potential of high density structure (which is represented as ϕ) is enhanced, called 'potential hump' [30]. It, in turn, leads to a phase change of the DF wave (*i.e.*, direction change of E_y) when the local electric potential ϕ satisfies the condition $|\nabla\phi| > |E_y|$. At this moment, the high density structure begins to split. This transition process from the ion accumulation to plasma splitting is depicted in Fig. 2-5. The electric field distribution of DF wave and the morphology of the high-density plasma structure in two different processes are shown. The upper part (red one) indicates the process of ion accumulation toward the position of high density structure. The lower part (purple one) represents the splitting process of high density structure after the phase change of DF wave.

During the splitting process of one structure (as shown in the purple mode), the E'_y provided by the phase change of the DF wave applies an acceleration $a = eE'_y / m$ to the leading edge. Then the leading edge moves forward along the $\mathbf{E}\times\mathbf{B}$ direction with the velocity $v_L = v_g + at$ (t represents the time) which is larger than v_g, and catches up with the preceding structure. For the trailing edge, the direction of acceleration $a = eE'_y / m$ provided by the phase change of DF wave E'_y is opposite to the direction of v_g (stems from the inertia of the previous state). Therefore, the trailing edge moves forward along the $\mathbf{E}\times\mathbf{B}$ direction but with the velocity $v_T = v_g - at$ that is smaller than v_g, and then encounters and merges with the leading edge of succeeding structure. In this dynamic process, from a microscopic perspective, the high density structure continuously adjusts itself (rotating, merging and splitting) to maintain a self-consistent interaction with the phase change of DF wave. From a macroscopic observation, the high density structure moves forward along the $\mathbf{E}\times\mathbf{B}$ direction with the group velocity.

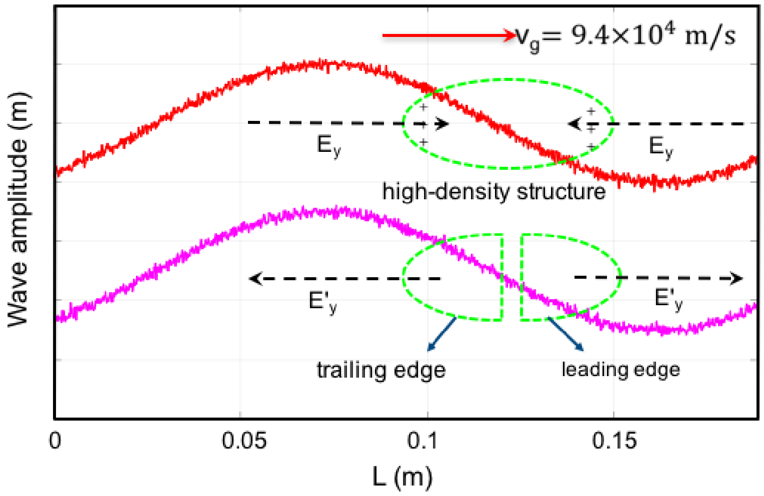

Figure 2-5. The electric field distribution of the DF wave and the morphology of the high density structure against the complete unfolding track of $\mathbf{E}\times\mathbf{B}$ drift, at two different processes.

The dynamic process of the high density structure discussed above is under the case where the plasma density n_e is constant. The number of the high density structures above the racetrack stays unchanged. In the real HiPIMS discharge, the n_e is variable during one pulse time-on. Thus, the E'_y and the acceleration it provides are also variable. It is expected that both the electric field of DF wave E'_y and the acceleration a decrease with the reducing plasma density n_e since both are self-consistent with the ion accumulation. When the plasma density n_e is small (*i.e.*, the acceleration a is small), the leading edge cannot get enough acceleration to catch up and merge with the trailing edge of the preceding structure. Consequently, the splitting of the high density structure may be greater than the merging, and the number of the high density structures above the racetrack is increased. Similarly, when the plasma density n_e is high (*i.e.*, the acceleration a is important), the merging of high density structure may dominate over the splitting, and the number of high density structures above the racetrack is reduced. Such qualitative changing feature of high density structure matches the dynamic change trend of the spoke observed in experiment [31].

Given the above, the DF wave has a frequency range of a few hundreds of KHz and cm-scale long wavelength, and its propagation speed is approximately one-tenth of electron $\mathbf{E}\times\mathbf{B}$ drift velocity. These characteristics of the DF wave are consistent with those of the spoke. The same frequency range of oscillation has also been recorded on the discharge current, correlated with spoke [13]. Concerning the SF wave, it has MHz-range frequency and mm-scale wavelength, and its propagation speed is close to the ion sound velocity. The characteristics of the SF wave are in agreement with those of the ECD instability.

These comparisons and consistencies allow us to propose the coupling-induced wave model as a theoretical explanation for the spoke origin. In HiPIMS plasma, the coupling of DSEB wave and IS wave will induce a long-scale electric field oscillation which is defined here as DF wave. The spoke is the collective behavior of ion rearrangement guided by the DF wave along the azimuthal direction. Meanwhile, we give new insight into the excitation of ECD instability. Except for the DF wave, this coupling also induces another high-frequency electric field oscillation which is defined as SF wave. It is suggested that the ECD instability is the collective behavior of electron rearrangement guided by the SF wave along the azimuthal direction.

2.3 Numerical example

In order to verify the accuracy and the comprehension of the physical phenomena captured by the coupling-induced wave model, the experimental data reported from HiPIMS discharge are compared with the prediction results of our theoretical model.

Let us choose the case in which the plasma is formed from the sputtering of the Ti target via argon gas from Fig. 4 of [34], which was also used in [32] for the measurement of spoke velocities. The experimental conditions of [34] are directly used as input for the coupling-induced wave model. Hence, the mean electric field strength $E \approx 10^4$ V, the magnetic field strength above the titanium target surface is about 60 mT, the radius of the target is 2.5 cm, and the effective area of the racetrack is 20 cm^2. Based on these parameters, the evolutions of spoke rotating velocity and mode number along the racetrack are computed.

2.3.1 Evolution of spoke rotating velocity and mode number with the discharge current

In the coupling-induced wave model, we substitute plasma density with discharge current for obtaining the evolution of spoke velocity as a function of the discharge current. Indeed, the relationship between plasma density in the ionization region and discharge current I_d between target and substrate is derived by assuming the Hall coefficient $\omega\tau$ being equal to 3 [12] and using the Eq. (2-11):

$$n_e = \frac{I_d \cdot \omega\tau}{S \cdot e \cdot V_d}. \tag{2-11}$$

Through the calculation of the model, the evolution of spoke rotating velocity as a function of discharge current is plotted in Fig. 2-6.

In Fig. 2-6, the square symbol represents the prediction results of the proposed model, while the triangle symbol represents the experimental results from [32]. The dashed blue line indicates the linear fit of the experimental results with an estimated error bar. The regime I corresponds to the increase of the spoke velocity, and the regime II corresponds to its saturation phase. In recent experimental reports of HiPIMS [34][35], the spoke is manifested as the stochastic light pattern at low discharge current. By increasing the discharge current, the spoke mode evolves from a stochastic plasma to a periodic spoke pattern exhibiting several local high density structures. Therefore, we calculate the evolution of spoke rotating velocity at discharge current greater than 20 A.

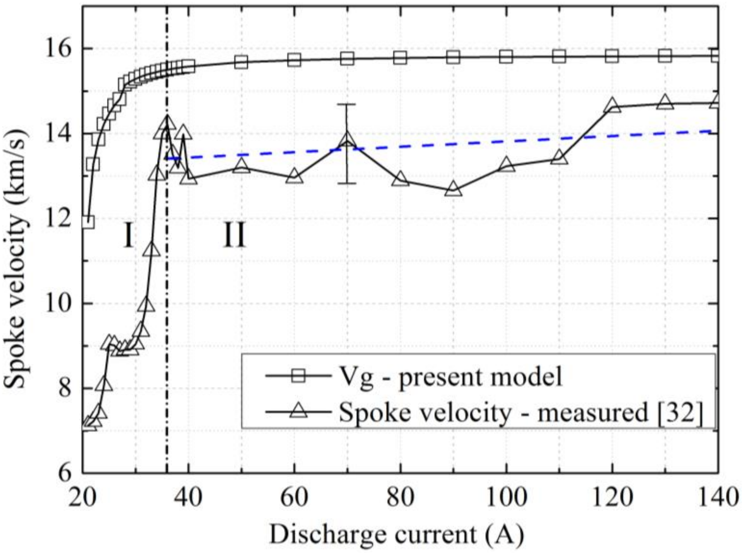

Figure 2-6. The spoke rotating velocity as a function of discharge current in the experiment [32] (triangle) and in the prediction results of the proposed model (square).

As Fig. 2-6 shows, the theoretical spoke rotating velocity from the proposed model increases with discharge current in the range from 20 A to 40 A. Beyond 40 A, the spoke rotating velocity slows down and stay almost flat (in the error limits) approaching a stable value of 15.8 km/s. A similar trend of spoke rotating velocity with discharge current has been experimentally recorded. In addition, two regimes, depending on the discharge current, are clearly identified from both model and experiment. The first regime (20 A < I < 36 A) corresponds to an acceleration of the spoke rotation, where the velocity increases with the increasing discharge current. The second regime (I > 36 A) is characterized by an asymptotic saturation of the spoke velocity. The group velocity from the proposed model overestimates experimental spoke velocity by at least 50% in the first regime, while the agreement between the experiment and the model is adequate in the saturation phase of the second regime. On the whole view, the mean relative error is less than 2 km/s, which represents ~13% in relative error. The reasons for this discrepancy have been discussed in Section 2.2 (from (i) to (iii)).

The calculation results show that the wavelength of spoke increases with discharge current. Namely, the spoke mode number above the racetrack decreases with increasing discharge current. The spoke with mode number of 4, 3, 2, and 1 at discharge currents of 50 A, 75 A, 100 A, and 130 A is in complete agreement with the experimental results of figure 4 in [34]. In addition, Fig. 2-7 also shows that the rotating velocity of spoke, which exhibits a slight upward trend as the discharge current increases.

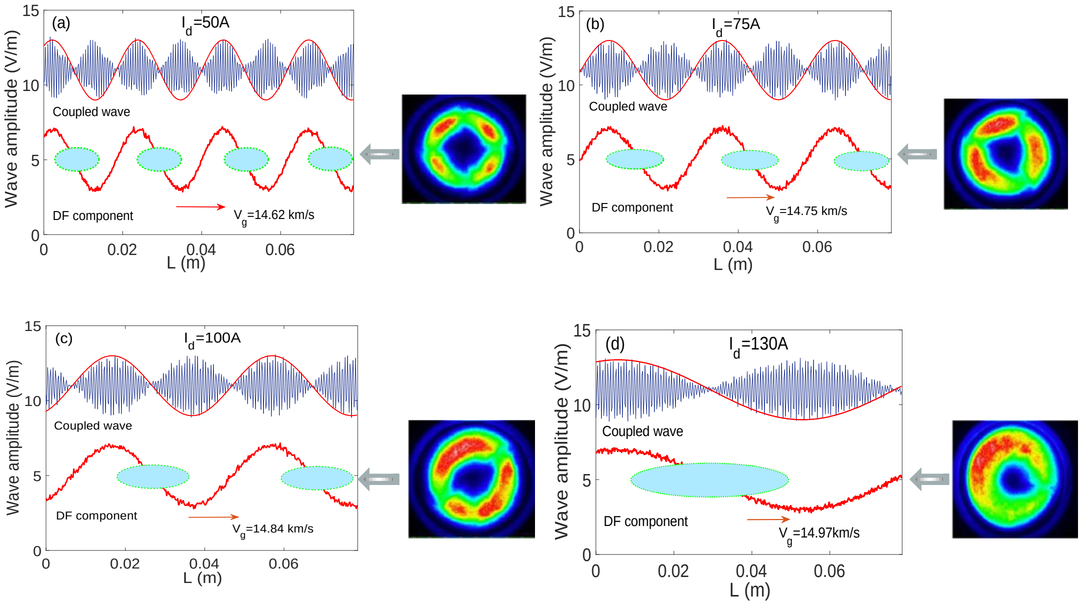

Figure 2-7. Influence of the different discharge currents on the spoke mode number: (a) $I_d = 50$ A ; (b) $I_d = 75$ A ; (c) $I_d = 100$ A ; (d) $I_d = 130$ A . The horizontal coordinate represents the unfolding racetrack of the $\mathbf{E} \times \mathbf{B}$ drift. Images of the spokes corresponding to the same discharge currents are taken from the figure 4 of [34].

2.3.2 Evolution of spoke rotating velocity and mode number with the magnetic field strength

According to Eqs. (2-6), (2-8) and (2-10) in which the origin of the spoke is associated with $V_d = E/B$, the spoke behavior depends obviously on the magnetic field strength. Therefore, the aim of this part is to take a closer look at the influence of magnetic field strength on the spoke behavior, including the spoke rotating velocity and mode number along the racetrack.

In the following description, the number of spoke waves is obtained by dividing the length (circumference) of the racetrack by the spoke wavelength. The quantitative influence of the magnetic field strength at different discharge currents on the spoke rotating velocity and number of spoke waves is shown in Fig. 2-8.

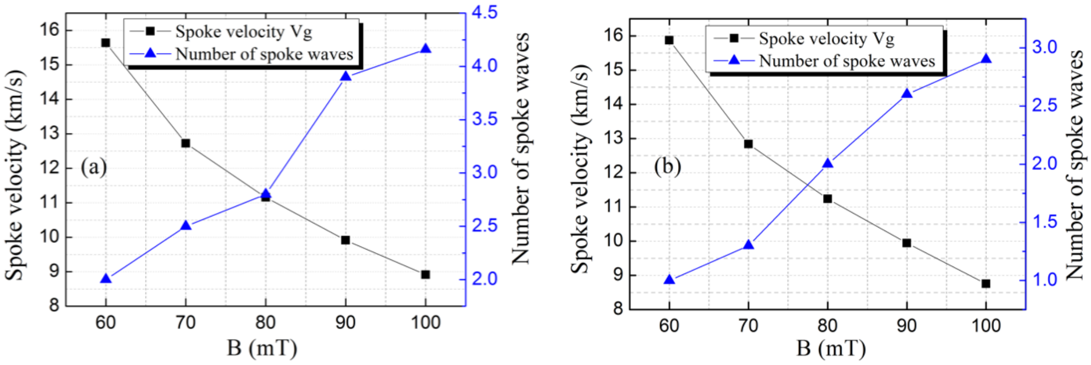

Figure 2-8. Influence of the magnetic field strength on the spoke rotating velocity and number of spoke waves along the racetrack for the discharge current of (a) 100 A and (b) 130 A.

Figure 2-8 shows that strengthening the magnetic field increases the number of spoke waves and decreases the spoke rotating velocity along the racetrack. At the discharge current of 100 A in Fig. 2-8(a), the spoke rotating velocity decreases from 15.6 km/s to 8.7 km/s, while the number of spoke waves increases from 2 to 4.2, when the magnetic field is strengthened from 60 to 100 mT. At a higher discharge current of 130 A (Fig. 2-8(b)), the spoke velocity is reduced from 15.8 km/s to 8.8 km/s, while the number of spoke waves increases from 1 to 2.9. This non-integer number of spoke waves indicates that there may be a ±1 fluctuation in the experimentally observed mode number at the same current region. Although the evolution of spoke rotating velocity and mode number along racetrack with the magnetic field strength is not measured in the chosen comparison group of [34], its changing trend is consistent with the experimental observations of [4]. Overall, the evolutions of spoke behavior following from the proposed model, including rotating velocity and mode number along the racetrack, match well with experimental findings, from the literature.

2.4 Conclusion

In this chapter, the coupling-induced wave model for the origin of the spoke in HiPIMS plasma is proposed by analyzing the dispersion relation of azimuthal waves. It reveals that during HiPIMS discharge, the coupling of Doppler-shifted electron Bernstein (DSEB) wave and ion sound (IS) wave induces a long-scale electric field (cm-size) oscillation waving at the frequencies difference, which is defined as the difference frequency (DF) wave, and a high-frequency short-scale electric field oscillation which is defined as the sum frequency (SF) wave. It is demonstrated that the collective behavior of ion rearrangement guided by the DF wave along azimuthal direction is associated with the observed spoke. The spoke location is defined by the phase change position of the DF wave, and its typical size is related to the wavelength. Besides, we give a new insight on the driving mechanism of the ECD instability. The collective behavior of electron rearrangement guided by the SF wave is considered as the ECD instability.

The characteristics of the spoke and ECD instability reproduced by the coupling-induced wave model, including frequency, velocity, wavelength, as well as the dynamic process and internal electric field distribution of the spoke, are strikingly similar to those reported in the literature. Moreover, the evolutions of spoke rotating velocity and mode number along the racetrack are considered. The numerical calculations from the theoretical model show that the spoke rotating velocity increases with the discharge current and decreases with the enhancement of the magnetic field strength. The spoke mode number along racetrack decreases with the increase of the discharge current, while it increases with the magnetic field strength. These calculated characteristics of the spoke from the coupling-induced wave model are in good agreement with those in the experimental measurements from the literature.

2.5 References

[1] Hecimovic, A., Böke, M., & Winter, J. (2014). The characteristic shape of emission profiles of plasma spokes in HiPIMS: the role of secondary electrons. Journal of Physics D: Applied Physics, 47(10), 102003.

[2] Anders, A., & Yang, Y. (2018). Plasma studies of a linear magnetron operating in the range from DC to HiPIMS. Journal of Applied Physics, 123(4), 043302.

[3] Lundin, D., Larsson, P., Wallin, E., Lattemann, M., Brenning, N., & Helmersson, U. (2008). Cross-field ion transport during high power impulse magnetron sputtering. Plasma Sources Science and Technology, 17(3), 035021.

[4] Ehiasarian, A. P., Hecimovic, A., De Los Arcos, T., New, R., Schulz-Von Der Gathen, V., Böke, M., & Winter, J. (2012). High power impulse magnetron sputtering discharges: Instabilities and plasma self-organization. Applied Physics Letters, 100(11), 114101.

[5] Anders, A., Ni, P., & Rauch, A. (2012). Drifting localization of ionization runaway: Unraveling the nature of anomalous transport in high power impulse magnetron sputtering. Journal of Applied Physics, 111(5), 053304.

[6] Winter, J., Hecimovic, A., De los Arcos, T., Böke, M., & Schulz-Von Der Gathen, V. (2013). Instabilities in high-power impulse magnetron plasmas: from stochasticity to periodicity. Journal of Physics D: Applied Physics, 46(8), 084007.

[7] Hecimovic, A. (2016). Anomalous cross-B field transport and spokes in HiPIMS plasma. Journal of Physics D: Applied Physics, 49(18), 18LT01.

[8] Ni, P. A., Hornschuch, C., Panjan, M., & Anders, A. (2012). Plasma flares in high power impulse magnetron sputtering. Applied Physics Letters, 101(22), 224102.

[9] Kozyrev, A. V., Sochugov, N. S., Oskomov, K. V., Zakharov, A. N., & Odivanova, A. N. (2011). Optical studies of plasma inhomogeneities in a high-current pulsed magnetron discharge. Plasma Physics Reports, 37(7), 621-627.

[10] Brenning, N., Lundin, D., Minea, T., Costin, C., & Vitelaru, C. (2013). Spokes and charged particle transport in HiPIMS magnetrons. Journal of Physics D: Applied Physics, 46(8), 084005.

[11] Gary, S. P., & Sanderson, J. J. (1970). Longitudinal waves in a perpendicular collisionless plasma shock: I. cold ions. Journal of Plasma Physics, 4(4), 739-751.

[12] Brenning, N., Merlino, R. L., Lundin, D., Raadu, M. A., & Helmersson, U. (2009). Faster-than-Bohm cross-B electron transport in strongly pulsed plasmas. Physical review letters, 103(22), 225003.

[13] Klein, P., Hnilica, J., Hubička, Z., Čada, M., Šlapanská, M., Zemánek, M., & Vašina, P. (2017). Cathode voltage and discharge current oscillations in HiPIMS. Plasma Sources Science and Technology, 26(5), 055015.

[14] Chen F F and Smith M D 2005 Plasma, Van Nostrand's Scientific Encyclopedia, 1 (Wiley online Library)

[15] Ducrocq, A., Adam, J. C., Héron, A., & Laval, G. (2006). High-frequency electron drift instability in the cross-field configuration of Hall thrusters. Physics of Plasmas, 13(10), 102111.

[16] Lafleur, T., Baalrud, S. D., & Chabert, P. (2016). Theory for the anomalous electron transport in Hall effect thrusters. II. Kinetic model. Physics of Plasmas, 23(5), 053503.

[17] Lampe, M., Manheimer, W. M., McBride, J. B., Orens, J. H., Papadopoulos, K., Shanny, R., & Sudan, R. N. (1972). Theory and simulation of the beam cyclotron instability. The Physics of Fluids, 15(4), 662-675.

[18] Muschietti, L., & Lembège, B. (2013). Microturbulence in the electron cyclotron frequency range at perpendicular supercritical shocks. Journal of Geophysical Research: Space Physics, 118(5), 2267-2285.

[19] Janhunen, S., Smolyakov, A., Sydorenko, D., Jimenez, M., Kaganovich, I., & Raitses, Y. (2018). Evolution of the electron cyclotron drift instability in two-dimensions. Physics of Plasmas, 25(8), 082308.

[20] Bussac, M. N., Edery, D., Pellat, R., & Soule, J. L. (1978). Stabilization of the linear drift tearing mode by coupling with the ion sound wave. Physical Review Letters, 40(23), 1500.

[21] Tsikata, S., & Minea, T. (2015). Modulated electron cyclotron drift instability in a high-power pulsed magnetron discharge. Physical review letters, 114(18), 185001.

[22] Bel, L., & Zia, H. S. (1985). Regular reduction of relativistic theories of gravitation with a quadratic Lagrangian. Physical Review D, 32(12), 3128.

[23] I. B., & Kulsrud, R. M. (1960). Ion wave instabilities. The Physics of Fluids, 3(6), 937-945.

[24] Shalaby, M., Broderick, A. E., Chang, P., Pfrommer, C., Lamberts, A., & Puchwein, E. (2017). Importance of resolving the spectral support of beam-plasma instabilities in simulations. The Astrophysical Journal, 848(2), 81.

[25] Rayleigh L. 1899 Nature LX, 64 (London)

[26] Rayleigh, L. (1917). XLVII. The theory of anomalous dispersion. The London, Edinburgh, and Dublin Philosophical Magazine and Journal of Science, 33(198), 496-499.

[27] Ostrovskii, L. A. (1967). Propagation of wave packets and space-time self-focusing in a nonlinear medium. Sov. Phys. JETP, 24(4), 797-800.

[28] Morin, D., “Dispersion,” Harvard University Physics Course. [Online]. Available: http://www.people.fas.harvard.edu/~djmorin/waves/dispersion.pdf

[29] Revel, A., Minea, T., & Tsikata, S. (2016). Pseudo-3D PIC modeling of drift-induced spatial inhomogeneities in planar magnetron plasmas. Physics of Plasmas, 23(10), 100701.

[30] Anders, A., Panjan, M., Franz, R., Andersson, J., & Ni, P. (2013). Drifting potential humps in ionization zones: the “propeller blades” of high power impulse magnetron sputtering. Applied physics letters, 103(14), 144103.

[31] Klein, P., Estrin, F. L., Hnilica, J., Vašina, P., & Bradley, J. W. (2016). Simultaneous electrical and optical study of spoke rotation, merging and splitting in HiPIMS plasma. Journal of Physics D: Applied Physics, 50(1), 015209.

[32] Hecimovic, A., Maszl, C., Schulz-von der Gathen, V., Böke, M., & von Keudell, A. (2016). Spoke rotation reversal in magnetron discharges of aluminium, chromium and titanium. Plasma Sources Science and Technology, 25(3), 035001.

[33] Yang, Y., Liu, J., Liu, L., & Anders, A. (2014). Propagation direction reversal of ionization zones in the transition between high and low current magnetron sputtering. Applied Physics Letters, 105(25), 254101.

[34] Hecimovic, A., Schulz-von der Gathen, V., Böke, M., von Keudell, A., & Winter, J. (2015). Spoke transitions in HiPIMS discharges. Plasma Sources Science and Technology, 24(4), 045005.

[35] Yang, Y., Zhou, X., Liu, J. X., & Anders, A. (2016). Evidence for breathing modes in direct current, pulsed, and high power impulse magnetron sputtering plasmas. Applied Physics Letters, 108(3), 034101.

[36] Anders, A. (2011). Discharge physics of high power impulse magnetron sputtering. Surface and Coatings Technology, 205, S1-S9.

Chapter 3 TaC/a-C:H films deposited in HiPIMS and DC magnetron sputtering

In this chapter, we focus on the study of transition metal carbide TaC/a-C:H films prepared by HiPIMS and DCMS. A series of TaC_x/a-C:H films across a fine range of $0.4<x<0.8$ were deposited in HiPIMS by varying the flow rate of acetylene (C_2H_2) from 10 to 18 standard cubic centimeters per minute (sccm). At each flow rate of C_2H_2, TaC/a-C:H films were deposited in three substrate bias modes: floating, -50 V, and -100 V. For comparison, TaC/a-C:H films at each C_2H_2 flow rate ranging from 10 to 18 sccm were also prepared in DC without the substrate bias. The chemical bonding state, structure, morphology, residual stress, mechanical properties, and tribological performance as well as oxidation resistance of all the films were characterized. By comparing the TaC/a-C:H films deposited in (i) different C_2H_2 flow rates and (ii) different deposition conditions (DC and HiPIMS with different substrate bias modes), the correlations between carbon content, deposition conditions and mechanical properties, tribological behavior and oxidation resistance were systematically discussed and established.

3.1 Research background and purpose

Transition metals in groups IVB and VB with carbon, together make strong solids in the rocksalt (NaCl) structure. The transition metal carbide film have been a hot topic for industrial applications and academic research for decades due to their high hardness [1][2][3], high melting point and excellent chemical stability [4][5][6][7]. Unlike the nitride system, the carbon-based transition metal film is characterized by the nanocomposite structure consisting of two separate phases, nanocrystalline grains of carbide and amorphous carbon matrix. Since this structure has the potential to improve the mechanical properties and wear resistance [8], the metal carbide/amorphous carbon nanocomposite films are widely used as protective coatings on the surfaces of precision steel components, cutting tools and machinery components [9]. Based on the above structural feature and application scope, a variety of transition metal carbide films have been investigated extensively, such as WC [10][11], TiC [8][12][13], NbC [14][15] and ZrC [16].

Among transition metal carbides, tantalum carbide (TaC) has attracted considerable attention since it has high hardness, good thermal stability, high melting temperature (3880 °C), low contact resistance and excellent tribological performance. Zhao, Z. *et al*. [17] fabricated TaC coatings on tantalum by interstitial carburization, and studied their mechanical properties and scratch resistance. Morris, R. *et al.* [18] prepared a series of TaC compositions by hot isostatic pressing (HIP) of Ta and TaC powder blends. The effect of phase transformations on the microstructure of the films was discussed and the precipitation sequence was found to be paramount in controlling the grain morphology. Hackett, K. *et al.* [19] studied the phase constitution and mechanical properties of Ta-C system via hot-pressing mixed powders of TaC and Ta in C/Ta atomic ratios of 1.0, 0.9, 0.8, 0.7, and 0.6 at 1800 °C for 2 h. It demonstrated that the grain size decreased with increasing carbon content, with a corresponding increase in Vickers hardness from 13.5 to 20 GPa. In addition, Evans, R. D. *et al.* [20][21] investigated the influence of deposition parameters on the composition and structure of the nanocomposite TaC/a-C:H films in the reactive DC magnetron sputtering, including acetylene flow rate, applied bias voltage, and substrate rotation rate. The results showed that (i) TaC crystallite size increased with substrate bias, (ii) an increase of sp^3-C bond with increasing C_2H_2 flux and (iii) the possibility of increased sp^2-C bond angle disorder with increasing C_2H_2 flux and substrate bias. Poladi, A. *et al.* [22] studied the effect of C content on the structural, mechanical, wear and corrosion properties of TaC films via DC magnetron sputtering. They showed that ceramic TaC films (20 at.% of C content) exhibit optimal mechanical properties and wear resistance, while metallic Ta(C) films (lower 5 at.% of C content) exhibit the best corrosion resistance.

Although a variety of advanced surface techniques have been applied to the preparation of tantalum carbide films [23][24][25], to the best of our knowledge, the TaC/a-C:H film prepared via HiPIMS has never been studied. The characteristics of high ionization rate and high bombardment energy of the HiPIMS plasma can not only tune (i) the grain size and (ii) the compactness of the film morphology, but also influence (iii) the volume ratio of amorphous matrix (a-C:H) and crystalline TaC phase, (iv) the ratio of sp^3/sp^2 -C bonds, (v) the mean grain separation and (vi) stoichiometric ratio x of TaC_x grain. The last four points have a crucial impact on the hardness, toughness and tribological properties of the film. Especially toughness, it is lacking in carbon-based transition metal films. And poor toughness is detrimental when subjected to high load and/or long-term friction conditions, since the possibility of fracture failure (which causes catastrophic damage to wear resistance). Therefore, the research on the nanocomposite structure and properties of TaC/a-C:H films deposited by HiPIMS is worth looking forward to. Moreover, when TaC/a-C:H film is used as the protective coating, the high-temperature environment cannot be avoided. At this point, the anti-oxidation capability of the film is critical as it limits the application scope and efficiency, as well as the service life. However, investigations into the oxidation resistance of TaC/a-C:H films are rarely explored. Besides, research on TaC/a-C:H films in published studies has mainly focused on the effect of carbon content varying over a wide range (from pure nanocrystalline TaC without amorphous carbon phase to almost pure amorphous diamond-like carbon (i.e., doped with Ta atoms)) on the properties of the film [26][27][28]. The disadvantage is that large changes in carbon content may mask other factors contributing to the film properties, such as minor changes in the stoichiometric ratio cause dramatic fluctuations in hardness. The effect of changing the carbon content within a narrow range on the structure and properties of the TaC/a-C:H films is rarely studied. Therefore, we focus on the study of TaC/a-C:H films in HiPIMS. The structure, mechanical properties, tribological properties and oxidation resistance of the films were analyzed systematically.

3.2 Deposition condition

The nanocomposite TaC/a-C:H films were prepared via HiPIMS (Hüttinger Elektronik 4002) by sputtering a tantalum target (150 mm in diameter and 8 mm in thickness, 99.9% purity) in Ar and C_2H_2 gas mixture. The cathode discharge parameters were set to: U = -600 V, I = 2.2 A (average current), t_{on} = 45 μs, f = 500 Hz. The potential of the substrate holder was operated at three modes: floating, -50 V, -100 V bias. The reference films were deposited by DC (Pinnacle Plus, Advanced Energy) with average current of 2.2 A, f = 50 KHz and T_{off} = 5 μs. Except for the power supply, other deposition parameters are the same as in HiPIMS. M2 HSS circular substrates (63 HRc, ∅=30 mm×8 mm), stainless steel slides (40 mm×20 mm×4 mm), silicon wafers (10 mm×10 mm) and iron sheets (400 mm×4 mm×0.25 mm) were selected as the substrates for testing mechanical properties, tribological performance, morphology, chemical bonding states and residual stress. The substrates of M2 and stainless steel were mirror polished with a diamond suspension of 1 μm of granulometry and degreased in ethanol afterward. Prior to film deposition, the vacuum chamber was pumped down to the base pressure ~10^{-4} Pa. The substrates were etched for ten minutes to remove adventitious contaminants attached to the surface. Subsequently, a tantalum interlayer of approximately 200 nm thickness was preliminarily deposited between the TaC/a-C:H film and the substrate to improve the film adhesion. During the deposition of all batches, the working pressure was 0.4 Pa. The distance D_{t-s} between the substrate holder and the target was 10 cm. The flow rates of working gas Ar and C_2H_2 were controlled by mass flow controllers. The flow rate of Ar was maintained at 200 sccm and C_2H_2 was varied from 10 sccm to 18 sccm with 2 sccm step increments. To obtain homogeneous films, the rotating substrate holder was fixed at 30 revolutions per minute (r.p.m).

3.3 Film characteristics

3.3.1 Chemical bonding state

Fig. 1 shows high resolution spectra of XPS C 1s for TaC/a-C:H films deposited in DC and HiPIMS (shown in (a) and (b)) and deposited in different substrate bias (in HiPIMS) (shown in (c)). The C 1s peak exhibits five main components, which distribute at 282.8 eV (Ta-C), 284.5 eV (sp^2-C), 285.3 eV (sp^3-C) and 286.8 eV (C-O) respectively. Table 3-1 lists the stoichiometric ratio *x* of TaC$_x$ crystallites calculated from XPS, with the specific values of the bonding fractions for Ta-C, sp^2-C, sp^3-C. According to the value of C_2H_2 flow rate, the samples were named as TaC10, TaC12, TaC14, TaC16, TaC18, respectively. The fractions of these bonds were determined by the relative peak areas of the fitted peaks. Overall, two different variation trends can be observed in Fig. 3-1 for the proportion between the carbide Ta-C and amorphous carbon.

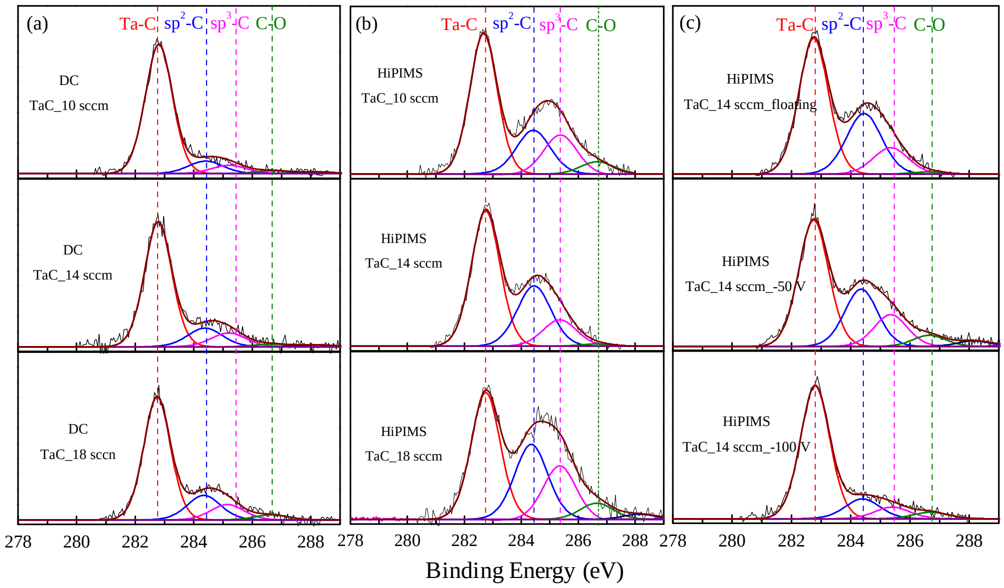

Figure 3-1. High resolution XPS spectra C 1s for the surface of TaC/a-C:H films: (a) DC; (b) HiPIMS with floating substrate; (c) HiPIMS with substrate bias.

As the C_2H_2 flow rate grows, a decrease of the Ta-C bond and a gradual increase of the amorphous carbon content (sp^2-C and sp^3-C bonds) are observed in both DC and HiPIMS films. Further information on the amorphous carbon phase is the continuous increments in sp^2-C bond and the seemingly random variation of the sp^3-C bond in parallel with the increase in C_2H_2 flow rate. For DC deposited films, as the C_2H_2 flow rate increases, the Ta-C bond decreases from 77.4 to 69.29 at.%, and the sp^2-C bond rises from 16.2 to 20.6 at.%. For HiPIMS deposited films, with C_2H_2 flow rate increases from 10 to 18 sccm, the Ta-C bond decreases from 55.3 to 44.4 at.%, while the sp^2-C bond rises from 21.3 to 30.6 at.%. There is no regular change in the content of sp^3-C bond as the C_2H_2 increases, either in DC or in HiPIMS deposited films. It fluctuates randomly within a small range and maintains a stable content of nearly 9.1 at.% and 22.4 at.% for DC films and HiPIMS films, respectively. The stoichiometric ratio of the TaC/a-C:H film (the *x* in TaC_x/a-C:H) increases with the C_2H_2 in both DC and HiPIMS. From 10 to 18 sccm, *x* increases from 0.45 to 0.69 for DC deposited films and from 0.65 to 0.78 for HiPIMS deposited film. Comparing the C 1s peak of DC deposited films and HiPIMS deposited films, the incorporation of C in the HiPIMS deposited film is higher, characterized by the higher stoichiometric ratio and the higher amorphous carbon content. It is related to the higher energy density and higher ionization rate of the HiPIMS plasma, which enhances the reactivity between Ta and C during discharge process and at the growing interface of the film, thus leading to higher incorporation of C content in the growth of the film [29]. The similar results have also been observed by Souček, P. *et al.* in [30], showing that deposition of the TiC/a-C:H coatings with the same carbon composition required approximately 2–3 times higher acetylene flow rate in DCMS as in HiPIMS.

As the substrate bias increases from floating to -100 V in HiPIMS, the content of Ta-C bond increases, while the contents of sp^2-C and sp^3-C bonds decrease. Take the films deposited at 16 sccm C_2H_2 as an example, the content of Ta-C bond rises from 50.4 to 78 at.%, while the sp^2-C and sp^3-C bonds decrease from 29 to 13.9 at.% and from 20.6 to 8.1 at.%. It is consistent with the result in [21]. The increased content of Ta-C bond is because Ta ions obtain more kinetic energy from the acceleration of the biased substrate (due to their own mass advantages) when they eject from target to bombard the substrate. The higher kinetic energy results in Ta and C to react as completely as possible at the growing interface of the film and thus an increase in Ta-C content. As a result, the stoichiometric ratio of the TaC grain also increases with the substrate bias. Typically, the enhanced bombardment energy of the film-forming plasma causes a higher crystallinity, larger grain sizes and higher sp^3-C content in the amorphous carbon matrix. However, the content of sp^3-C bond is lowered in our case. Although the enhanced bombardment energy provided by substrate bias induces the subsurface penetration and compressive stress which facilitates the formation of sp^3-C, it also can initiate the thermal activation that converts sp^3-C to sp^2-C [31][32]. The influence of these two aspects on the content of sp^3-C is mutually constrained. Since the ionization rate of HiPIMS is very high, a large amount of high-speed ion bombardment onto the substrate may be more prone to developing thermal activation. This is confirmed by the coarsening of the grains as the substrate bias increases obtained in the subsequent XRD. Therefore, the growth of sp^3-C content is offset by the graphitization (induced via thermal activation) and the content of sp^3 bond is reduced. Note that although the graphitization is more pronounced, the sp^2-C content does not increase. It may be because the greatly increased Ta-C bond occupy too much C source, and the remaining carbon is not enough to support the increase of sp^2-C content. Based on the above analysis, it can be concluded that the evolution of chemical bonding state is not only related to the composition of the plasma which has been reported several times in the literature [27][33], but also strongly depends on the ionization rate and bombardment energy of the reactive plasma.

Table 3-1. The tendencies for bonding fractions of the Ta-C, sp^2-C and sp^3-C in the films, the bonding fractions determined by the relative peak areas of the fitted peaks C 1s.

Batch no.	Composition [at.%]		Types of bonding for C 1s XPS [at.%]			Stoichiometric ratio (TaC_x)
	Ta	C	C-Ta	sp^2-C	sp^3-C	
			DC			
TaC10	63.5	36.5	77.4	16.2	6.4	0.45
TaC12	59.9	40.1	75.1	14.3	10.6	0.50
TaC14	55.3	44.7	71.3	17.7	11.0	0.58
TaC16	52.5	47.5	72.8	20.0	7.2	0.66
TaC18	50.2	49.8	69.3	20.6	10.1	0.69
			HiPIMS_floating substrate			
TaC10	46.2	53.8	55.3	21.2	23.5	0.65
TaC12	44.0	56.0	55.2	24.1	20.7	0.70
TaC14	41.6	58.4	53.0	24.7	22.3	0.74
TaC16	39.7	60.3	50.4	29.0	20.6	0.77
TaC18	36.3	63.7	44.4	30.6	25.0	0.78
			HiPIMS_substrate bias			
TaC12	44.0	56.0	55.2	24.1	20.7	0.70
TaC12-50V	48.7	51.3	67.4	15.2	17.4	0.71
TaC12-100V	52.9	47.1	82.0	12.1	5.9	0.73
TaC14	41.6	58.4	53.0	24.7	22.3	0.74
TaC14-50V	44.3	55.7	55.1	25.7	19.2	0.69
TaC14-100V	48.7	51.3	73.6	13.9	12.5	0.77
TaC16	39.7	60.3	50.4	29.0	20.6	0.77
TaC16-50V	42.6	57.4	58.5	21.9	19.6	0.79
TaC16-100V	49.0	51.0	78.0	13.8	8.2	0.81

3.3.2 Morphology

Fig. 3-2 exhibits the SEM micrographs of the fracture cross-sections and of the top surfaces (inserted in the upper right corner) for the TaC/a-C:H films deposited at different C_2H_2 flow rates. Among them, the upper row and the lower row represent the results of DC deposited films and of HiPIMS (floating) deposited films, respectively. As the C_2H_2 flow rate increases, all the DC deposited films exhibit a glassy morphology, while all the HiPIMS deposited films display a character of columnar structure. The columns of the HiPIMS deposited films do not change with increasing C_2H_2 flow rate, showing very similar density. This difference in cross-sectional morphology between DC and HiPIMS deposited films is contrary to what is commonly reported in the literature [34][35]. In the HiPIMS deposition condition, the film-forming plasma has high ionization rate. The motion path of ions is highly oriented and almost perpendicular to the substrate surface due to the attraction of substrate floating potential. Under this plasma characteristic, the film is grown by the rapid, continuous and normally incident species, thereby forming a dense columnar structure perpendicular to the substrate [37].

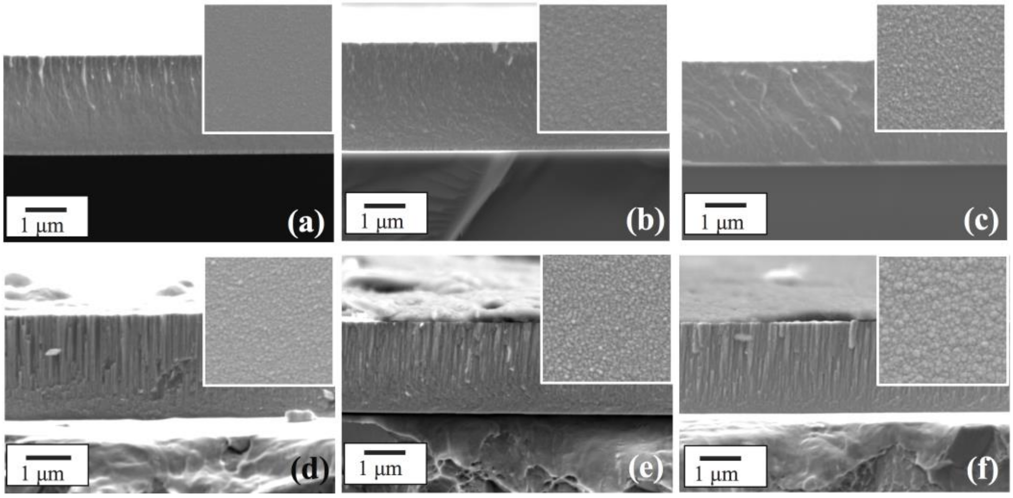

Figure 3-2. SEM micrographs of cross-section and top surface (inset in the upper right corner) of TaC/a-C:H films deposited in DC (upper row, a-c) and in HiPIMS (lower row, d-f) with various C_2H_2 flow rates: (a, d) 10 sccm, (b, e) 14 sccm and (c, f) 16 sccm.

The surface morphologies exhibit granular structure in both DC and HiPIMS deposited films. As the C_2H_2 flow rate increases, the average size of these granules increases. The surface morphology gradually becomes rough. Moreover, the roughness of HiPIMS deposited films is higher than that of DC deposited films, which is caused by the columnar growth of the HiPIMS film that leads to rough surface naturally. Besides, the rougher surface of the HiPIMS deposited film also stems from higher substrate temperature, a by-product of higher bombardment energy, of HiPIMS discharge process. It adjusts the diffusion process of condensed atoms at the growing interface and forces them to aggregate into larger sized clusters, creating a rougher surface on the HiPIMS deposited film.

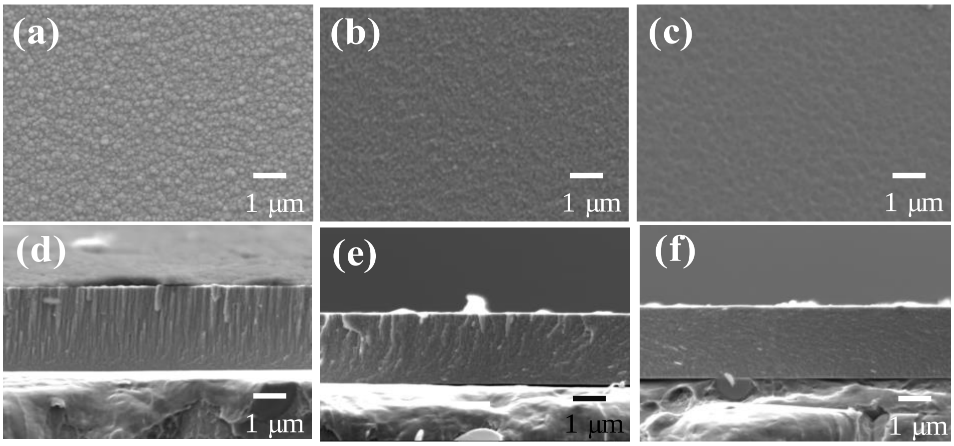

Figure 3-3. SEM micrographs of top surface (a-c) and of cross-section (d-f) of HiPIMS deposited TaC/a-C:H films at 16 sccm C_2H_2 with different substrate bias: (a)floating, (b) -50 V, (c) -100 V.

Take the films deposited at 16 sccm C_2H_2 as an example, the SEM micrographs of TaC/a-C:H films with different substrate biases prepared in HiPIMS are presented in Fig. 3-3. It can be seen that when the substrate bias is applied, the columnar structure previously seen is interrupted and replaced by a denser and less structured morphology (see Fig. 3-3e) and then, when the bias voltage increases to -100 V, the columnar growth disappears completely, evolving to a glassy morphology (Fig. 3-3f). Moreover, the top surface tends to be smoother with substrate bias and exhibits a character of slight etching at - 100V bias. These denser cross-section and smoother surface are due to the high kinetic energy of ion bombardment, which impacts a few atomic layers beneath the growing interface and delivers sufficient mobility for atomic rearrangement.

3.3.3 Microstructure

Fig. 3-4 shows a series of X-ray diffractograms for TaC/a-C:H films with different C_2H_2 flow rates. The left side and right side represent the diffraction patterns of DC and HiPIMS deposited films, respectively.

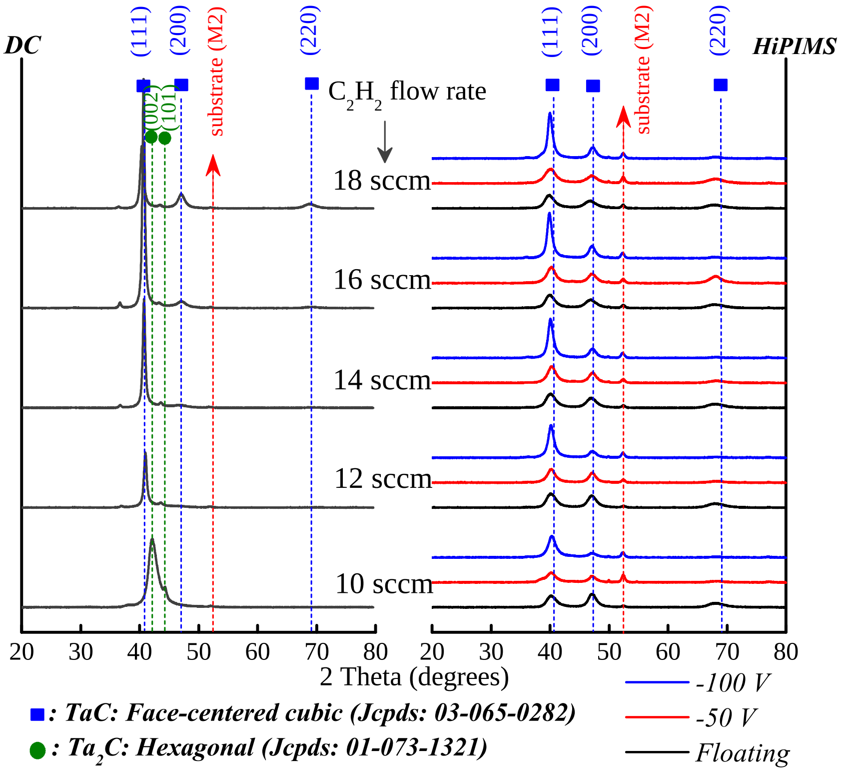

Figure 3-4. X-ray diffractograms of TaC/a-C:H films deposited in DC (left) and in HiPIMS (right).

For DC deposited film at 10 sccm C_2H_2 flow rate, the diffraction peaks observed at $2\theta \approx 42.5°$ and $44.5°$ can be ascribed to (002) and (101) for hexagonal Ta_2C. When C_2H_2 flow rate increases from 12 to 14 sccm, a strong peak at $2\theta \approx 40.65°$ and a very weak peak at $2\theta \approx 47.29°$ occur. They are assigned to (111) and (200) for face-centered cubic TaC. It indicates that DC deposited films at 12 and 14 sccm exhibit (111) preferred orientation. As C_2H_2 flow rate increases to 16 and 18 sccm, the diffraction peaks at $2\theta \approx 40.65°$, $47.29°$ and $69.12°$ coexist, which correspond to (111), (200) and (220) planes for fcc TaC.

For HiPIMS films (without substrate bias) deposited with C_2H_2 flow rate from 10 to 18 sccm, the diffraction peaks distribute at $2\theta \approx 40.65°$, $47.29°$ and $69.12°$ corresponding to (111), (200) and (220) planes of face-centered cubic TaC, respectively. These diffraction peaks exhibit similar intensities with a slight left-shift with increasing C_2H_2 flow rate. Generally, the shift of the diffraction peak toward a low angle is related to lattice expansion and/or compressive stress. From Fig. 3-7(b), the compressive stress of HiPIMS (floating) deposited films (black line with ball) remains almost unchanged. Therefore, it can be inferred that the left shift of the peak position derives from lattice expansion caused by the stoichiometric change of the TaC grains [38][39]. As the substrate bias increases in HiPIMS, the full width at half maximum (FWHM) of (111) peak decreases monotonically with the increase in intensity, which corresponds to microstructure coarsening. It is provided by the enhanced substrate temperature due to high energy ion bombardment effect of the substrate bias.

The mean grain size of TaC/a-C:H films as a function of the C_2H_2 flow rate under various deposition conditions are presented in Fig. 3-5. It is calculated from XRD diffraction spectra using the Scherrer formula, where the total broadening of the FWHM is attributed to the grain size and the strain broadening is ignored. It can be found that the grain size of the HiPIMS deposited films is smaller than that of DC deposited films at each C_2H_2 flow rate. This is achieved through the higher nucleation density induced by the HiPIMS plasma and the higher amorphous carbon content in the HiPIMS deposited films. On the one hand, the high ionization rate of the HiPIMS plasma will interrupt the growth of TaC grain and thus force newly arriving TaC-forming species to renucleate. On the other hand, higher amorphous carbon content is more effective in inhibiting grain growth. Therefore, the grain size of the HiPIMS deposited films is smaller than that of the DC deposited films. For the grains that gradually coarsen as the substrate bias increases in HiPIMS, the fundamental driving mechanism is enhanced ion bombardment since the elevated ion velocity and energy serve the same role as substrate heating. Moreover, the less amorphous carbon content with the substrate bias provides a weaker growth-inhibiting effect on the TaC grains. The TaC grains are thus coarsened with the application of the substrate bias.

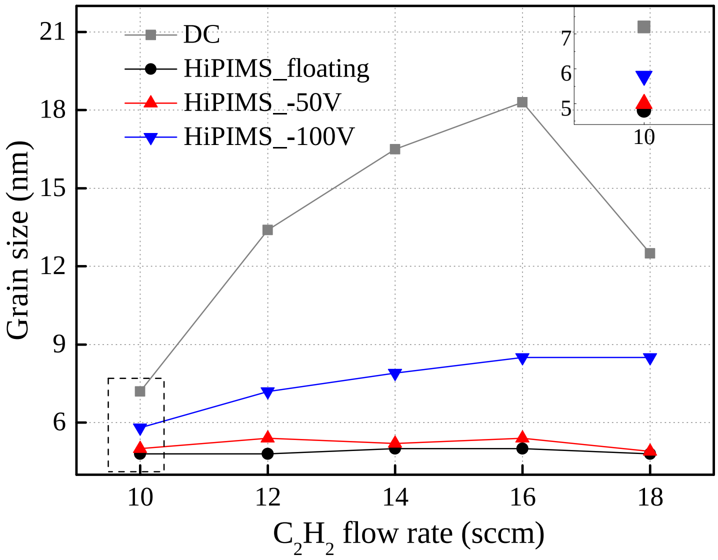

Figure 3-5. The grain size of TaC/a-C:H films with various C_2H_2 flow rates.

The grain size shows a different evolution with C_2H_2 flow rate under different deposition conditions. For DC deposited films, the grain size first increases and then decreases, with the turning point at 16 sccm of C_2H_2. From 10 to 16 sccm of C_2H_2 flow rate, the increase in carbon source provides a favorable growth condition for the phase of tantalum carbide, which gradually coarsens the TaC grain and reaches the maximum size of 18.3 nm. When the further increase of C_2H_2 flow rate exceeds 16 sccm, the amorphous carbon matrix surrounding the TaC grains may reach an appropriate amount capable of isolating each TaC grain, thereby hindering the growth of TaC grains via its encapsulation role and forcing the newly arrived species to renucleate. Similar evolution of grain refinement as carbon content increases in nc-MeC/a-C:H (Me stands for transition metal) films prepared by DC magnetron sputtering have been reported in [40][41].

For films deposited in HiPIMS with floating substrate and -50 V bias, the grain size remains unchanged, which is consistent with the results in [27][30]. The evolution of TaC grain is governed by the competition between the grain growth and the hindering effect of amorphous carbon matrix. Since the grain size is finer and the content of amorphous carbon is higher in HiPIMS (indicated by XPS) compared to that in DC, the hindering effect of the sufficient amount of amorphous carbon acted on grown grains is more pronounced than that in DC deposited films. The grain coarsening with C_2H_2 flow rate (as occurred in DC deposited film) is thus suppressed to some extent. Consequently, it can be inferred that in HiPIMS with floating and -50 V bias, the constant trend of grain size may be an almost balanced result of the competition between the hindering effect of amorphous carbon and growth of grains.

For films deposited in HiPIMS with -100 V bias, the grain size increases slightly in the range of $5.8 \rightarrow 8.4$ nm from 10 to 18 sccm of C_2H_2. The growing grain size with increasing carbon content is also observed in [34] where the deposition system used was HiPIMS with -150 V substrate bias. This increased tendency of grain size is attributed to the fact that at high bias condition, the ion bombardment effect dominates the chemical bond of the film, manifesting as a reduction in the amorphous carbon content. The sealing and suppressing action of less amorphous carbon matrix on the TaC grain growth is thus weakened. Therefore, the grain growth effect may win in the aforementioned competition and the grain size gradually increases with the C_2H_2 flow rate.

3.4 Film properties

3.4.1 Mechanical properties

The hardness H and effective Young’s modulus E^* of the TaC/a-C:H films with various C_2H_2 flow rates are plotted in Fig. 3-6. The evolutions of hardness and effective Young’s modulus are similar for films prepared in both DC and HiPIMS (without substrate bias).

As the C_2H_2 flow rate increases from 10 to 16 sccm, the hardness and effective Young's modulus increases correspondingly. They reach maximum values at 16 sccm

C_2H_2 flow rate. The hardness and effective Young's modulus of 35.0 GPa and 423 GPa are obtained for DC deposited film and of 40.6 GPa and 470 GPa are achieved for HiPIMS deposited film. Once the C_2H_2 flow rate further increases to 18 sccm, the evolutions of hardness and effective Young's modulus reverse and begin to decrease.

In the case of carbon-based nanocomposite films, the grain size, mean grain separation, stoichiometric ratio, matrix properties, and morphology are important factors in determining the mechanical properties. For DC deposited films, the morphology (indicated by the SEM) is very similar under different C_2H_2 flow rates. Meanwhile, the sp^3/sp^2 -C ratio, which acts to harden the carbon matrix, gradually reduces since sp^2-C increases and sp^3-C floats randomly in a small range (obtained from XPS) as the C_2H_2 flow rate increases. It can therefore be stated that the two factors of morphology and matrix properties (sp^3/sp^2 -C) do not contribute to the mechanical properties of the DC deposited films. The grain size of the DC deposited films first increases and then decreases with C_2H_2 flow rate from 12 to 18 sccm. Note that the film deposited at 10 sccm C_2H_2 exhibits Ta_2C phase. Here we only consider the influence of the TaC phase. According to the Hall & Petch relation, this trend of grain size suggests that the hardness first decreases and then increases, which is contrary to what we observed. However, for carbon-based nanocomposite film, the increased content of amorphous carbon matrix may cause the grains to be gradually separated despite the continued increase in grain size. Therefore, with C_2H_2 flow rate increase from 12 to 16 sccm, there may be a narrow separation space between the grains. It will restrict the deformation under applied load caused by dislocation movement and decrease cracks propagation in the amorphous carbon matrix [30][38], resulting in an increase in the hardness. At 18 sccm C_2H_2 flow rate, the grain size suddenly decreases while the amorphous carbon content continues to increase. The mean grain separation is thus further broadened. The wider grain separation, filled by the amorphous carbon matrix, not only promotes the influence of the amorphous carbon phase on the film behavior but also provides more space for nano-crack initiation and propagation, therefore causing a decrease in hardness [42].

Besides, as C_2H_2 flow rate increases from 12 to 18 sccm, the stoichiometric ratio of TaC grain increases from 0.5 to 0.69. It is known that the exceptional properties of face-centered cubic TaC stem from their electronic structure and prevalent bonding states with a mixed metallic-covalent character. Carbon vacancies influence the electronic structure (interactions between atoms in the lattice and valence electron concentration), and can thus be used to tune the Fermi level, the position of which, with respect to the pseudogap between bonding and antibonding states, is decisive for the bond strength. Therefore, depending on the carbon vacancies, substoichiometric condition could make the hardness and thermal stability of films exhibit unusual behavior [1][3]. Riedl, H. *et al.* [3] reported that for the single-phase fcc structured TaC_x coatings, the $TaC_{0.78}$ film exhibited the highest hardness. When x is greater than 0.78, the hardness begins to decrease. Hong, Q. *et al.* [43] demonstrated through electronic structure calculation that the population at the Fermi level is indication of the hardness and thermal stability. Although a perfect symmetry between the bonding and antibonding states within the pseudogap is favorable for highest values, the maximum hardness and melting temperature are observed for $x \leq 0.85$ in the TaC_x system. For the TaC/a-C:H films in our case, although XPS technology being used to obtain stoichiometric ratio has measurement errors, we suspect that $x=0.69$ is still less than the critical value of the substoichiometric ratio for driving maximum hardness. Therefore, the increase in the stoichiometric ratio in DC deposited films (from 12 to 18 sccm) continues to increase the hardness. The reduced hardness at 18 sccm is dominated by the wide mean grain separation, and here the stoichiometry hardening is offset.

For HiPIMS (without substrate bias) deposited films, as C_2H_2 flow rate increases, the trends of morphology and ratio sp^3/sp^2 -C are similar to those of DC deposited films. These two factors are also independent of the evolution of mechanical properties, as they did in DC deposited films. As C_2H_2 flow rate increases, the grains that remain constant in size can be separated by the growing content of the amorphous carbon matrix, and the spacing is getting larger. From 10 to 16 sccm of C_2H_2, such a nanocomposite structure can hinder the dislocation operation caused by grain boundary sliding and induce the grain incoherence strains, thus enhancing the resistance to plastic deformation [47]. However, as C_2H_2 flow rate continues to increase to 18 sccm, the larger separation spacing may provide too much space to make the grains easier to slip and rotate, thereby worsening the hardness of the film. In addition, the stoichiometric ratio of HiPIMS deposited films increase from 0.65 to 0.78 as C_2H_2 flow rate increases from 10 to 18 sccm. It can be determined that the increase in the stoichiometric ratio favors the rise of hardness in the segment of 10 to 18 sccm. The observed reduced hardness at 18 sccm is the result of the competition between stoichiometric hardening and softening of the excessive mean grain separation, which is similar to that in DC deposited film. In summary, it can be concluded that the evolutions of the hardness for DC and HiPIMS (without substrate bias) deposited films are dominated by two factors, mean grain separation and stoichiometric ratio of TaC grain.

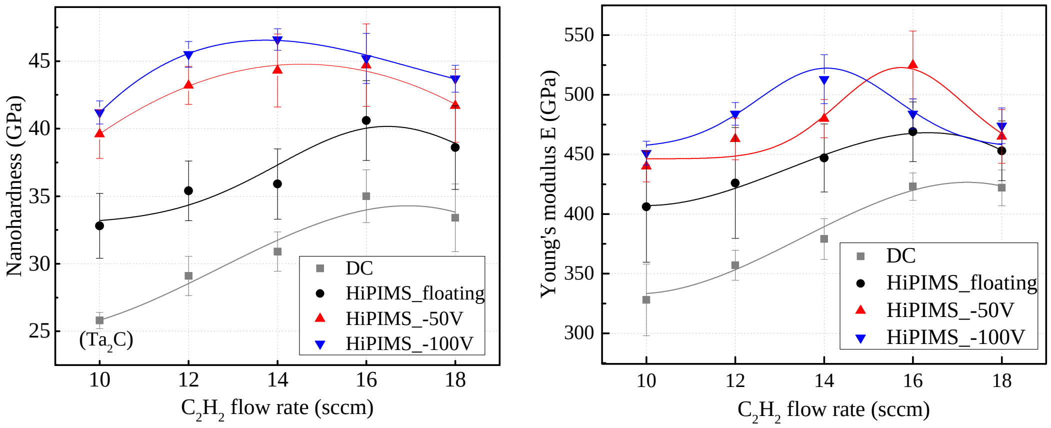

Figure 3-6. Hardness H and effective Young's modulus E^* of TaC/a-C:H films with various C_2H_2 flow rates.

Comparing the mechanical properties of DC and HiPIMS deposited films, at all C_2H_2 flow rates, the hardness and Young's modulus of the HiPIMS deposited films are higher than that of the DC deposited films. It is attributed to the finer grain size, higher stoichiometric ratio, and higher compressive stress (as indicated by Figure 3-7(b)) of the HiPIMS deposited films.

As the substrate bias increases in HiPIMS, the hardness of TaC/a-C:H films increases at each C_2H_2 flow rate. The compressive stress also increases with the substrate bias, shown in Fig. 3-7. Interestingly, the hardness increases dramatically in the segment of floating to -50 V bias, and increases slightly in the segment of -50 V to -100 V bias. This growth ratio of hardness in different bias segment is completely opposite to that of compressive stress, which increases slightly in the floating to -50 V, and increases drastically in the -50 V to -100 V. Although it is widely held that higher compressive stress in film gives rise to higher hardness, the compressive stress hardening here is obviously not the main factor for increasing hardness. Moreover, the content of the amorphous carbon matrix decreases while the grains coarsen as the substrate bias increases. That is, under the same C_2H_2 flow rate, the mean grain separation spacing is reduced with the application of the substrate bias. It is indicative of lower hardness, as opposed to the measured hardness trend. Besides, the sp^3-C content decreases as the substrate bias increases. Therefore, the changes in mean grain separation and matrix property do not contribute to the enhanced hardness. Based on above, it can be inferred that enhanced hardness is attributed to the stoichiometric ratio. According to XPS calculations, the stoichiometric ratio of TaC grain increases with the substrate bias. Taking the films deposited at 12 sccm C_2H_2 as an example, it rises from 0.7 to 0.73, which is consistent with the increase in hardness. In addition, the denser morphology with the substrate bias also contributes in part to the increased hardness.

When we observe the overall trend of film hardness as a function of C_2H_2 under the three bias modes (in HiPIMS) in Fig. 3-6, it can be found that the maximum hardness gradually shifts to the left with the increase of the substrate bias from floating to -100 V, and occurs at 14 sccm with -100 V bias. Comparing the TaC/a-C:H films deposited at 14 and 16 sccm C_2H_2 under the bias of -100 V, their morphologies are similar in density and the film deposited at 16 sccm has higher compressive stress (which indicates a higher hardness). Meanwhile, the stoichiometric ratio of the film deposited at 14 sccm is 0.77 and of the film deposited at 16 sccm is 0.81, shown in Table 3-1. It can thus be speculated that the lower hardness of the film at 16 sccm is caused by the stoichiometric ratio of 0.81, which may exceed the threshold for determining the maximum hardness in the carbon-based nanocomposite film. Therefore, in the case of the substrate bias, the mean grain separation and compressive stress are subordinate to stoichiometric ratio and morphology with regards to influencing film hardness. Moreover, the substoichiometric ratio for obtaining the maximum hardness appears at x≈0.77, which is close to the results observed in [3].

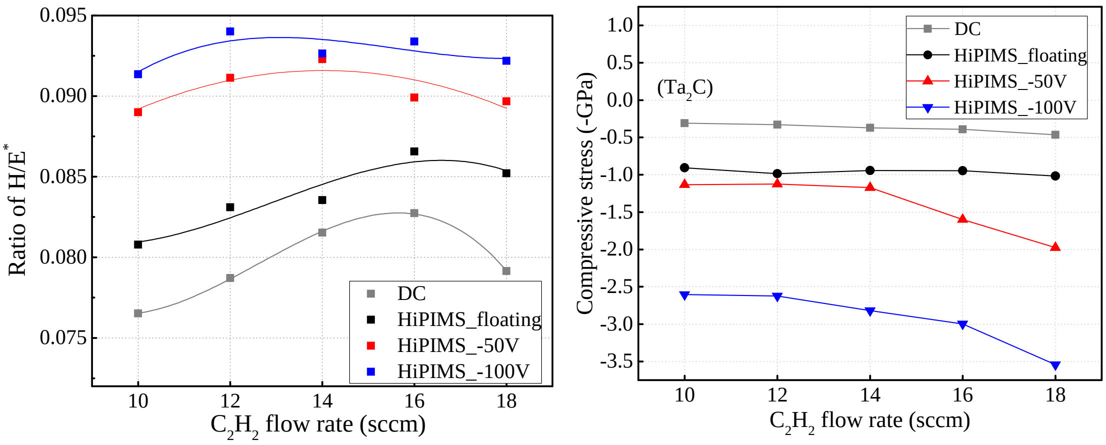

Figure 3-7. Ratio H/E^* and compressive stress of TaC/a-C:H films as a function of C_2H_2 flow rate.

The mechanical behavior of TaC/a-C:H films is also characterized by the ratio H/E^*, which reflects the toughness of the film characterizing the film ability to absorb energy and plastically deform without fracturing [44][45]. Hard nanocomposite film with enhanced toughness is desirable since it greatly contributes to the optimization of tribological performance. However, the superhard nanocomposite film is considered to be lack toughness [46]. In our case of TaC/a-C:H films, the H/E^* ratio as a function of C_2H_2 flow rate are shown in Fig. 3-7(a). For DC and HiPIMS (without substrate bias) deposited films, their H/E^* ratios exhibit a trend consistent with the evolution of hardness. The H/E^* ratios of DC deposited films are lower than those of HiPIMS deposited films in all C_2H_2 flow rates. For the films deposited in HiPIMS with substrate bias, H/E^* ratio is substantially promoted with bias value at each C_2H_2 flow rate. It stems from the large increase in hardness H and the slight rise in effective Young's modulus E^* along with the substrate bias. Generally, toughness can be improved in two ways, one is by adding a second metal element as the ductile phase; the other is by regulating the nanostructure (grain size and distribution of amorphous carbon). Despite the means of toughening, it is still not easy to achieve toughening while holding the hardness due to the high requirements for precise adjustment of the nanocomposite structure. In the present work, HiPIMS deposition conditions including floating and biased substrate are indicated to be promising synthetic methods for regulating nanocomposite structure to enhance toughness.

The improved toughness in HiPIMS conditions is interpreted as the random orientation of the grains (indicated via XRD), the smaller grain size, and the higher content of amorphous carbon of the HiPIMS deposited films. The random orientation (i.e., high angle grain boundaries) can minimize grain incoherence strain and promote grain boundary sliding in the nanocomposite film [47]. The smaller grain size creates a large volume of grain boundaries and diminishes the size of the initial crack. The higher content of amorphous carbon can absorb the elastic energy released under load due to its relative physico-chemical inert. The synergy of these factors are thus capable of (i) releasing the strain by easier grain boundary sliding under the load exceeding elastic strength, and (ii) terminating the propagation of cracks through deflection effect at high volume grain boundaries and through dispersion and absorption of strain energy within amorphous carbon matrix. Both of them are responsible for improving toughness, thus the higher toughness is achieved in HiPIMS deposited films.

3.4.2 Tribological behavior

The tribological performance of the films was carried out by pin-on-disk Tribometer from CSM (Switzerland). All the measurements were done via unlubricated sliding against 6 mm WC/Co balls in ambient air at a relative humidity about 40%. Test parameters were set to 5 N applied normal load, 10 cm/s sliding speed, 3 mm contact track radius and 10000 sliding laps. After the tribology tests, the cross-sectional profiles of the wear tracks were characterized by using Altysurf profilometer equipped with inductive probe. The normalized wear rates (W_r) were calculated using equation $W_r=V/(L\times S)$, where V is the wear volume of the films, L is the applied normal load, and S is the sliding distance.

Carbon-based nanocomposite films not only exhibit excellent mechanical properties, but is also accompanied by the promising tribological performance due to the amorphous carbon phase. Fig. 3-8 summarizes the friction coefficient and wear rate of the TaC/a-C:H films prepared in DC and HiPIMS. It shows a gradual reduction in friction coefficient and wear rate as the C_2H_2 flow rate increases in both DC and HiPIMS deposited films.

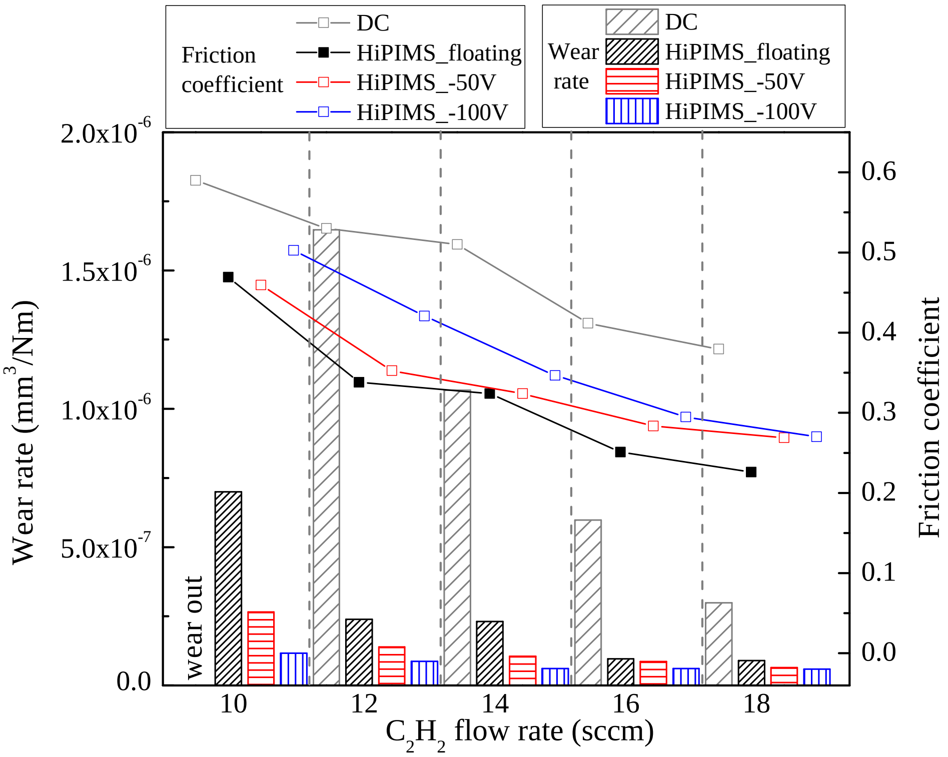

Figure 3-8. Friction coefficient (lines) and wear rate (columns) of TaC/a-C:H films as a function of C_2H_2 flow rate.

For the friction coefficient, as C_2H_2 flow rate increases from 10 to 18 sccm, it decreases from 0.6 to 0.37 for DC deposited films and decreases from 0.47 to 0.23 for HiPIMS (without bias) deposited films. Such reduced tendency is attributed to the increase in sp^2-C content with the increase of C_2H_2 flow rate. When the C_2H_2 flow rate increases to 18 sccm, the sp^2-C content reaches 20.6 at.% and 30.6 at.% in the films deposited in DC and HiPIMS, corresponding to the friction coefficient of 0.37 and 0.23 (the minimum), respectively. Moreover, the friction coefficient of HiPIMS deposited films is lower than that of DC deposited films, which is determined by the higher sp^2-C content of the HiPIMS deposited film. The application of the substrate bias in

HiPIMS from floating to -100 V results in an increase in the friction coefficient at all C_2H_2 flow rates. It is because the sp^2-C content decreases as the substrate bias increases, as evidenced by the XPS results, which weakens the self-lubricating effect on the film surface. The friction behavior that evolves with the substrate bias is consistent with the literature [36][48][12]. Combining the friction coefficient of the films under different deposition conditions, it is concluded that the friction coefficient of the TaC/a-C:H films is primarily controlled by the sp^2-C content. Since the sp^2-C phase enhances the formation of easily sheared graphitic tribolayer, the film with higher content of sp^2-C exhibits superior friction performance.

The wear rate, shown as columns in Fig. 3-8, exhibits a tendency consistent with the friction coefficient of DC and HiPIMS (without substrate bias) deposited films. As C_2H_2 flow rate increases, it gradually decreases in the range of $7.0 \times 10^{-7} \rightarrow 8.9 \times 10^{-8}\ \mathrm{mm^3/Nm}$ for HiPIMS films and decreases in the range of $1.7 \times 10^{-6} \rightarrow 2.6 \times 10^{-7}\ \mathrm{mm^3/N}$ for DC deposited films. Note that the wear rate of the DC film deposited at 10 sccm C_2H_2 is not shown in Fig. 3-8 since this film is completely worn through. Moreover, it can be observed that applying substrate bias in HiPIMS can further promote a reduction in wear rate, contrary to its effect on the friction coefficient. For a more detailed analysis of the wear behavior, Fig. 3-9 exhibits the SEM images of the wear tracks on the DC and HiPIMS deposited films. In addition, the HiPIMS films deposited under 12 sccm C_2H_2 with different substrate biases are taken as an example to analyze the influence of the substrate bias on the wear behavior. The evolution of the top view and cross section of the wear track is shown in Fig. 3-10.

From Fig. 3-9, it can be observed that in both DC and HiPIMS (without substrate bias) deposited films, the wear track becomes narrower and shallower as C_2H_2 flow rate increases, consistent with the evolution of friction coefficient. At 12 sccm C_2H_2 flow rate, the wear track of the DC deposited film is locally damaged, showing significant delamination, accumulated wear debris, grooves and cracks at the boundary of the film breakage. For the HiPIMS deposited film at the same C_2H_2 flow rate, there are no detected failure, agglomerated debris and cracks on the wear track. The obvious grooves parallel to the sliding direction are observed on this wear track via the corresponding enlarged image. These results of DC and HiPIMS films deposited at 12 sccm C_2H_2 stem from the poor hardness and toughness. The lower hardness leads to a larger sliding contact surface between the counterpart ball and the film and a deeper penetration distance under applied load, which generates wider wear track and higher wear rate. Moreover, the lower hardness has less resistant against abrasion (of wear debris) during the test, resulting in a more pronounced groove [44][49]. The poor toughness does not effectively prevent crack propagation and then causes delamination and failure to take place after sliding multiple times. Therefore, higher wear rate (for HiPIMS film) and local failure (for DC film) appear at 12 sccm C_2H_2. Besides, the severe wear of the film at 12 sccm C_2H_2 is another reason for the high value of friction coefficient (i.e., a large sliding resistance) in addition to the low sp^2-C content.

As the C_2H_2 flow rate increases to 16 sccm, the wear tracks become smoother and narrower and the grooves become shallower in both DC and HiPIMS deposited films. It indicates improved wear resistance, whic is attributed to the continued increase in hardness, toughness and sp^2-C content. Moreover, less debris and narrower wear track are observed in HiPIMS deposited film compared to those in DC deposited film. As C_2H_2 flow rate further increases to 18 sccm, the wear tracks are slightly narrower in both DC and HiPIMS. The accumulated debris on the wear track of DC deposited film are greatly reduced. However, on the wear track of HiPIMS deposited film, the grooves become deeper again and the distinct tribolayer appears revealed by EDS maping analysis. The reappearance and deepening of grooves is due to the decrease in hardness after the C_2H_2 flow rate exceeds 16 sccm. Since the wear debris act as grinding particles during test process and abrade the film surface, the reduced hardness weakens the resistance of the film against abrasion. Thus the groove distribution on the wear track appears again. It is worth noting that although the hardness is reduced and the grooves are deepened, the wear rate of the film at 18 sccm C_2H_2 does not deteriorate rather than still decreases with increasing C_2H_2 flow rate. This is due to the lowest friction coefficient and the formation of tribolayer, which reduces the sliding resistance and acts as a protective layer to reduce the direct contact between the counterpart ball and the film surface to some extent, thereby contributing to the diminution of wear rate.

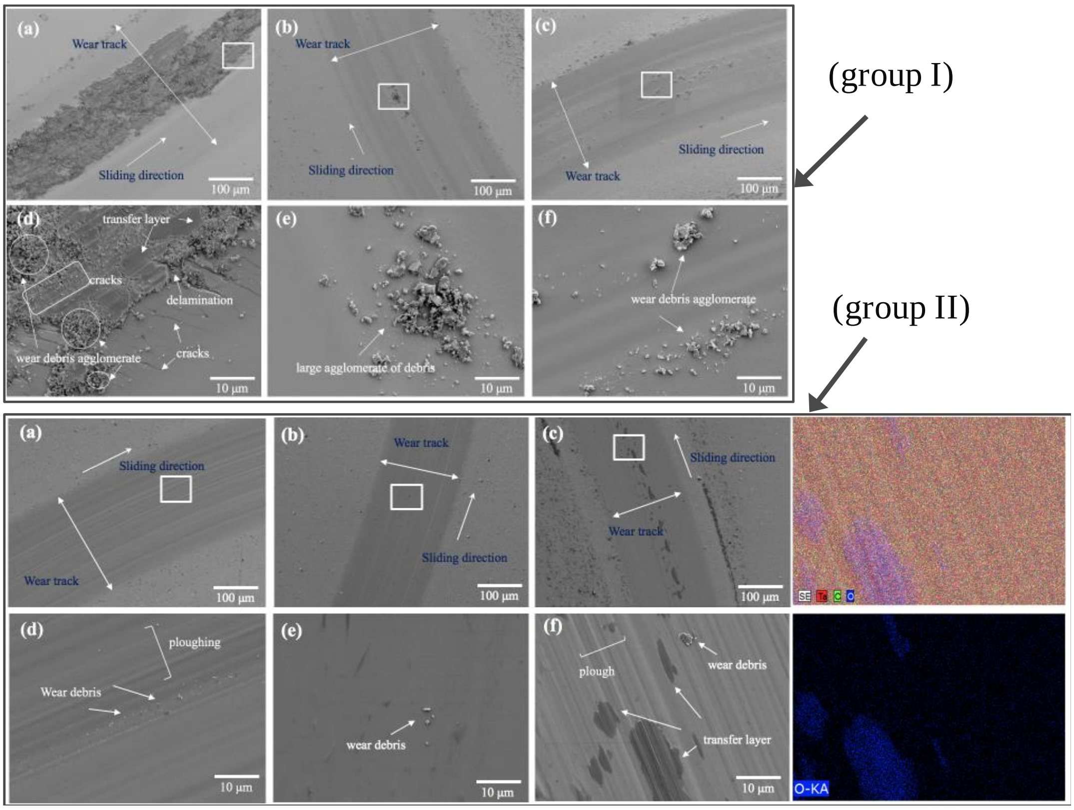

Figure 3-9. Wear tracks of the TaC/a-C:H films deposited in DC (group I) and in HiPIMS (group II). In both group, (a), (b) and (c) represent the films prepared at 12 sccm, 16 sccm and 18 sccm of C_2H_2 flow rate, (d), (e), (f) are the magnified views of the white squared regions in (a), (b), (c), respectively. The EDS maping of the subgraph (f) is displayed on the right side of group II.

By comparison, the friction and wear performances of the HiPIMS deposited films are superior to those of the DC deposited films, exhibiting smaller values of friction coefficient and wear rate, narrower and shallower wear tracks and less wear debris. There are three reasons for driving better tribological performance for the HiPIMS deposited films. First, HiPIMS discharge results in higher content of sp^2-C inside the film. Second, the higher bombardment energy of HiPIMS plasma produces greater compressive stress, which helps to terminate crack nucleation and propagation and thus improves the wear resistance. Third, the hardness and toughness of HiPIMS deposited films are higher. Not only do they contribute to improved wear resistance, but they also reduce the possibility of friction interlocking during multiple sliding processes, which results in less wear debris.

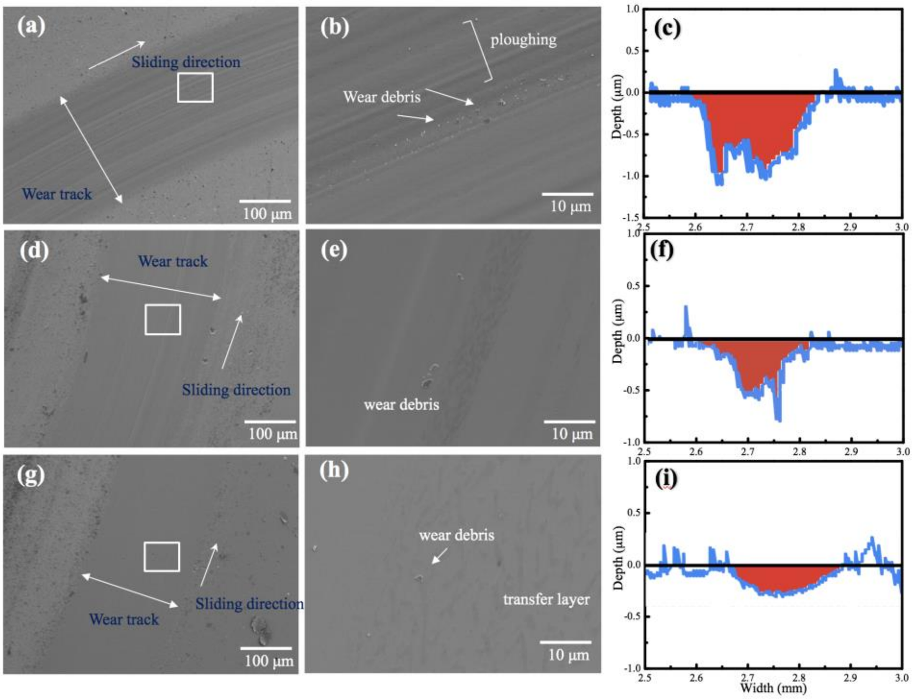

Figure 3-10. SEM images and cross profiles of wear tracks for HiPIMS TaC/a-C:H films deposited at 12 sccm C_2H_2 with different substrate bias: (a-c) floating, (b-f) -50 V, (g-i) -100 V.

It can be observed that as the substrate bias increases in HiPIMS, the wear track of the film becomes narrower and smoother. It is contrary to the evolution of the friction coefficient. The film with floating substrate is characterized by the obvious plowing grooves and wear debris, confirmed by the corresponding enlarged SEM image and cross profile of the wear track. With the substrate bias increases to -100 V, the wear track becomes narrower, the groove distribution becomes shallower as well as the wear debris decreases. Meanwhile, the cross profiles of the wear track also confirm the shallower and the fewer grooves. These results suggest a better resistance against wear debris damage as the substrate bias increases, which is supported by the increased hardness, toughness and compressive stress. With the substrate bias rises from floating to -50 V to -100 V, the hardness increases from 35.4 to 43.2 to 45.5 GPa, and the compressive stress increases from -0.98 to -1.12 to -2.61 GPa. At the same time, the wear rate (columns in Fig. 3-8) decreases linearly. It can thus be stated that from the floating to -50 V bias, the reduction in wear rate is mainly due to the enhanced hardness, while from -50 V to -100 V bias, it is attributed to the compressive stress. The contribution of compressive stress to wear rate is consistent with that in [50].

In summary, there are two factors that determine the wear behavior of the TaC/a-C:H films. On the one hand, under DC and HiPIMS deposition conditions without substrate bias, the tribochemical nature of the sp^2-C content dominates the wear behavior (the higher the sp^2-C content, the lower the wear rate), despite the decrease in hardness properties. This is because the presence of rich sp^2-C facilitates easy shearing of the two sliding surfaces. Moreover, the specific interface (interphase boundary), provided by the carbon matrix dispersed in the TaC grains, can dissipate and absorb the elastic energy released during the test and then divert and terminate the propagating cracks, which improves the wear resistance. The consistent wear behavior has also been reported in [8][14] in Nb- and Ti- carbide/amorphous carbon nanocomposite films. On the other hand, under HiPIMS deposition with different substrate bias, the wear behavior of the films is controlled by mechanical properties and compressive stress. Although the content of sp^2-C is lowered as the substrate bias increases, which causes shear sliding becomes difficult, the hardness, toughness and compressive stress are greatly increased. According to the delamination theory of wear proposed by Suh [51], the wear process consists of three stages: plastic deformation accumulation, crack nucleation and crack propagation. In the case of applying substrate bias, the high hardness (resisting plastic deformation), high toughness (enhancing load-bearing capability) and high compressive stress (preventing and slowing crack expansion) can improve the wear resistance of the film. This trend is consistent with the result of [48].

3.4.3 Oxidation resistance

Annealing treatment was performed under air atmosphere at different temperatures (from 200 °C up to 700 °C with an incremental step of 100 °C) with a dwell time of 2 h to test the oxidation resistance of TaC/a-C:H films. Subsequently, all films experienced a natural cooling process. The oxidation degree of the film after annealing was estimated by XRD and energy dispersive X-ray spectroscopy (EDS).

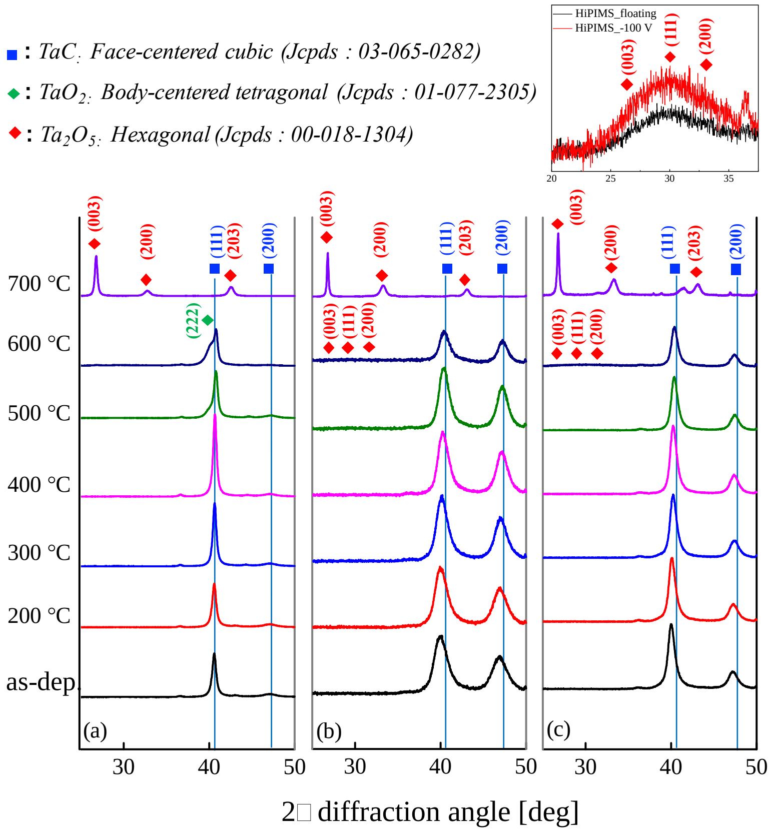

Figure 3-11. X-ray diffractograms of the TaC/a-C:H films deposited in (a) DC, in (b) HiPIMS with floating substrate and in (c) HiPIMS with -100 V bias as a function of

The oxidation resistance test was carried out on all TaC/a-C:H films. The results show that the oxidation resistance of the films remains almost unchanged with varying C_2H_2 flow rate, but the significant differences can be detected under different deposition conditions. In this section, the films deposited at 16 sccm C_2H_2 are used as the representative to analyze the effect of deposition condition on the oxidation resistance. The structural evolution of TaC/a-C:H films (at 16 sccm C_2H_2) with different annealing temperatures is illustrated in Fig. 3-11, in which (a), (b) and (c) represent the results of the films deposited in DC, HiPIMS with floating substrate and HiPIMS with -100 V bias, respectively.

As the annealing temperature rises to 700 °C, the gradual right shift of the diffraction peaks appears on all TaC/a-C:H films, which corresponds to the relaxation of compressive stress. After annealing at 400 °C, the diffraction peaks become narrower and more intense for the film deposited in DC and in HiPIMS with -100 V bias, which is explained by the slight coarsening of microstructure. After annealing at 500 °C, for the DC deposited film, the intensities of TaC peaks (111) and (200) begin to decrease while the (222) peak of the body-centered tetragonal TaO_2 phase begins to appear. For the films deposited in HiPIMS with -100 V bias, a slight decrease in the intensity of the TaC peaks (111) and (200) is also observed, but no significant peaks of tantalum oxide are detected. It should be noted that for the film deposited in HiPIMS with floating substrate, no change in intensity or width of the TaC peaks is detected.

After annealing at 600 °C, two phases, TaC and TaO_2, coexist in DC deposited film. Moreover, the intensity of the TaO_2 peak reaches a level comparable to that of (111) peak of the TaC phase. It reflects a gradual phase transformation from TaC to TaO_2. For the film deposited in HiPIMS with -100 V bias, the small peaks appear, identified as the (003) and (111) planes of the Ta_2O_5 phase, which confirms the beginning of oxidation. For the film deposited in HiPIMS with floating substrate, these Ta_2O_5 peaks can also be observed, but their intensities are relatively weak. After annealing at 700 °C, no TaC peaks can be detected in all films, indicating that the films are completely oxidized regardless of the deposition conditions. Through this structural development at different oxidation temperatures, it is proved that the film deposited in HiPIMS with floating substrate has stronger antioxidant capacity compared to that deposited in DC and in HiPIMS with -100 V bias. However, it is difficult to state the specific oxidation degree of the films based on the XRD results alone. For a more detailed study and comparison, the cross-sections of the films after annealing at 600 °C were analyzed by SEM and EDS scanning map, as shown in Fig. 3-12.

From Fig. 3-12, it can be observed that the thickness of 1.27 μm，0.72 μm and 1.22 μm of oxide layers (zone 1) are formed on the surfaces of the films deposited in DC, HiPIMS with floating substrate and HiPIMS with -100 V bias, respectively. It indicates that the film deposited in HiPIMS with floating substrate is less oxidized, consistent with the XRD results. In addition, after annealing at 600 °C, none of the films show any cracks on the surface or cross section. The cracks, if happening after annealing and/or cooling of the films, are associated with the mismatch of the thermal expansion coefficients between the substrate and the film. In our case, the pre-deposition of Ta interfacial layer between the TaC/a-C:H film and the substrate absorbs this mismatch. Moreover, the compressive stress present in the films may also prevent cracking of the film after annealing.

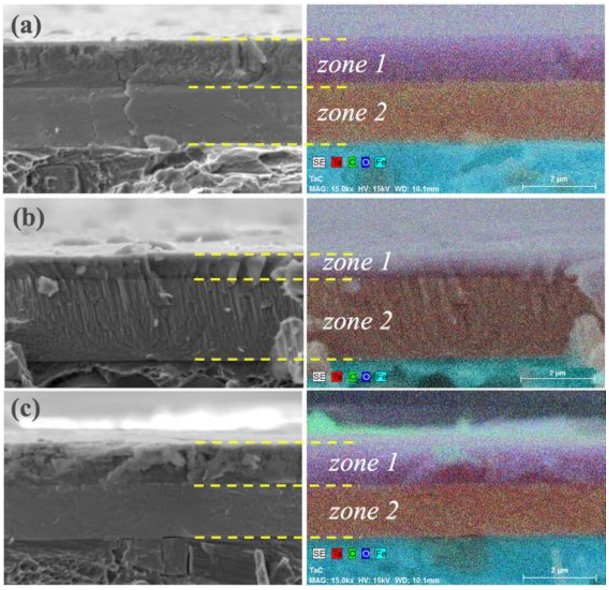

Figure 3-12. SEM/EDS images of cross-sections of the TaC/a-C:H films after annealing temperature at 600 °C: (a) DC, (b) HiPIMS with floating substrate and (c) HiPIMS with -100 V bias.

The better oxidation resistance of the film deposited in HiPIMS with floating substrate is related to the grain size. We know that the oxidation resistance of carbon-based nanocomposites can be achieved by oxidizing "crystalline grains" dispersed therein to form a barrier layer [52]. When the carbon-based nanocomposite film is exposed to a high-temperature oxidizing environment, the carbon on its surface is first oxidized, and then a decarburized layer composed of oxide grains is formed. As the oxidation continues and the reaction time prolongs, an oxide layer on the surface of the decarburized layer is formed. It can serve as a barrier layer to reduce the diffusion flux of oxygen and thereby protect the underlying material. In this process, the grain size and oxidation rate of the crystalline phase are important factors affecting the oxidation resistance of the film. For the film deposited in HiPIMS with floating substrate, the amorphous carbon is first oxidized (at >400 °C [53]) and the TaC grains are subsequently oxidized during the oxidation process. Since small-sized grains can be rapidly oxidized, the tantalum oxide layer can be formed at a faster rate on the film surface. This means that the rate of diameter reduction of the channels required for oxygen diffusion is also fast, which is the key to limiting the rate of oxygen diffusion toward the film. Meanwhile, the rapid formation of the oxide layer consumes a large amount of oxygen that will diffuse into the interior of the film, thereby slowing down the oxidation rate of the film. Therefore, the oxidation resistance of the film deposited in HiPIMS with floating substrate is higher. Besides, the oxidation resistance of the film appears to be independent of whether the morphology of the film is dense. As our results show, films prepared in the conditions of DC and HIPIMS with -100 V bias have denser morphologies (indicated by the SEM images in Fig. 3-2) but poorer oxidation resistance.

3.5 Conclusion

Nanocomposite TaC/a-C:H films were deposited utilizing DC magnetron sputtering and HiPIMS (operated at three substrate bias: floating, -50 V and -100 V) in C_2H_2/argon mixed atmosphere. The results reveal that the chemical bonding state, structure, morphology and various properties of the film are not only (i) modulated by the carbon content, but also (ii) strongly dependent on the deposition conditions.

Regardless of the deposition condition, as the carbon content increases, the hardness of the film increases first and then reaches a maximum with the typical nanocrystalline grains encapsulated by amorphous carbon matrix, followed by a decrease with further increase in carbon content. The tribological performance is gradually improved, while the oxidation resistance remains almost unchanged, as the C content increases.

Comparing the properties of films under DC and HiPIMS (without substrate bias) deposition conditions, it can be found that the HiPIMS deposited films have higher hardness and toughness, lower friction coefficient and wear rate, as well as stronger oxidation resistance. It is attributed to the higher volume fraction of amorphous carbon matrix, finer grains, higher stoichiometric ratio of TaC grains and greater compressive stress of the HiPIMS deposited films. These features responsible for better performance are supported by the greater degree of plasma reaction between Ta and C_2H_2 induced by the high energy density and high ionization rate of the HiPIMS discharge. In addition, the film grown in high-density continuous bombardment of HiPIMS plasma has a close columnar morphology while the DC deposited films exhibit a glassy morphology. The oxidation resistance of the film is found to be independent of the density of the macroscopic morphology.

As the substrate bias increases in HiPIMS, the mechanical properties and the wear rate of the deposited films are improved, while the friction coefficient and the oxidation resistance are deteriorated. These performance adjustments result from the enhanced ion bombardment effect. On the one hand, it causes the mobility of Ta ions and the degree of reaction with C to be enhanced at the growing interface of the film. The volume fractions of sp^2-C and sp^3-C are thus lowered and the carbide volume fraction is increased, which corresponds to the degradation of the friction coefficient. On the other hand, it results in the increased stoichiometric ratio of TaC grains, enhanced compressive stress, densification of the morphology, and coarsened grain. The first three promote optimization of mechanical properties and wear resistance while the latter one inhibit antioxidant ability of the film. It is demonstrated that HiPIMS provides a better strategy to tune the nanocomposite structure of TaC/a-C:H film in a way favorable for improving mechanical properties, tribological performance, and oxidation resistance.

3.6 References

[1] Lasfargues, H., Glechner, T., Koller, C. M., Paneta, V., Primetzhofer, D., Kolozsvári, S., Holec, D., Riedl, H., Mayrhofer, P. H. (2017). Non-reactively sputtered ultra-high temperature Hf-C and Ta-C coatings. Surface and Coatings Technology, 309, 436-444.

[2] Jhi, S. H., Louie, S. G., Cohen, M. L., Ihm, J. (2001). Vacancy hardening and softening in transition metal carbides and nitrides. Physical Review Letters, 86(15), 3348.

[3] Riedl, H., Glechner, T., Wojcik, T., Koutná, N., Kolozsvári, S., Paneta, V., Holec, D., Primetzhofer, D., Mayrhofer, P. H. (2018). Influence of carbon deficiency on phase formation and thermal stability of super-hard TaCy thin films. Scripta Materialia, 149, 150-154.

[4] Storms, E. K. (2016). The Refractory (Vol. 2). Elsevier.

[5] Wang, S. L., Li, K. Z., Li, H. J., Zhang, Y. L., & Feng, T. (2014). Structure evolution and ablation behavior of ZrC coating on C/C composites under single and cyclic oxyacetylene torch environment. Ceramics International, 40(10), 16003-16014.

[6] Wang, Y., Li, H., Fu, Q., Wu, H., Yao, D., Li, H. (2012). SiC/HfC/SiC ablation resistant coating for carbon/carbon composites. Surface and Coatings Technology, 206(19-20), 3883-3887.

[7] Pu, H., Niu, Y., Hu, C., Wang, G., Li, H., Zeng, Y., Zheng, X. (2015). Ablation of vacuum plasma sprayed TaC-based composite coatings. Ceramics International, 41(9), 11387-11395.

[8] Sánchez-López, J. C., Dominguez-Meister, S., Rojas, T. C., Colasuonno, M., Bazzan, M., Patelli, A. (2018). Tribological properties of TiC/aC: H nanocomposite coatings prepared via HiPIMS. Applied Surface Science, 440, 458-466.

[9] Peng, Z., Miao, H., Qi, L., Yang, S., Liu, C. (2003). Hard and wear-resistant titanium nitride coatings for cemented carbide cutting tools by pulsed high energy density plasma. Acta Materialia, 51(11), 3085-3094.

[10] Abad, M. D., Muñoz-Márquez, M. A., El Mrabet, S., Justo, A., Sánchez-López, J. C. (2010). Tailored synthesis of nanostructured WC/aC coatings by dual magnetron sputtering. Surface and Coatings Technology, 204(21-22), 3490-3500.

[11] El Mrabet, S., Abad, M. D., Sánchez-López, J. C. (2011). Identification of the wear mechanism on WC/C nanostructured coatings. Surface and Coatings Technology, 206(7), 1913-1920.

[12] Zehnder, T., Schwaller, P., Munnik, F., Mikhailov, S., Patscheider, J. (2004). Nanostructural and mechanical properties of nanocomposite nc-TiC/a-C: H films deposited by reactive unbalanced magnetron sputtering. Journal of applied physics, 95(8), 4327-4334.

[13] Martínez-Martínez, D., López-Cartes, C., Fernández, A., Sánchez-López, J. C. (2009). Influence of the microstructure on the mechanical and tribological behavior of TiC/aC nanocomposite coatings. Thin Solid Films, 517(5), 1662-1671.

[14] Zhang, K., Wen, M., Cheng, G., Li, X., Meng, Q. N., Lian, J. S., Zheng, W. T. (2014). Reactive magnetron sputtering deposition and characterization of niobium carbide films. Vacuum, 99, 233-241.

[15] Nedfors, N., Tengstrand, O., Lewin, E., Furlan, A., Eklund, P., Hultman, L., Jansson, U. (2011). Structural, mechanical and electrical-contact properties of nanocrystalline-NbC/amorphous-C coatings deposited by magnetron sputtering. Surface and Coatings Technology, 206(2-3), 354-359.

[16] He, X. M., Shu, L., Li, H. B., Li, H. D., Lee, S. T. (1998). Structural characteristics and hardness of zirconium carbide films prepared by tri-ion beam-assisted deposition. Journal of Vacuum Science & Technology A: Vacuum, Surfaces, and Films, 16(4), 2337-2344.

[17] Zhao, Z., Hui, P., Liu, F., Wang, X., Li, B., Xu, Y., Zhong, L., Zhao, M. (2019). Fabrication of TaC coating on tantalum by interstitial carburization. Journal of Alloys and Compounds, 790, 189-196.

[18] Morris, R. A., Wang, B., Matson, L. E., & Thompson, G. B. (2012). Microstructural formations and phase transformation pathways in hot isostatically pressed tantalum carbides. Acta Materialia, 60(1), 139-148.

[19] Hackett, K., Verhoef, S., Cutler, R. A., Shetty, D. K. (2009). Phase constitution and mechanical properties of carbides in the Ta–C system. Journal of the American Ceramic Society, 92(10), 2404-2407.

[20] Evans, R. D., Howe, J. Y., Bentley, J., Doll, G. L., & Glass, J. T. (2005). Influence of deposition parameters on the composition and structure of reactively sputtered nanocomposite TaC/aC: H thin films. Journal of materials research, 20(9), 2583-2596.

[21] Evans, R. D., Doll, G. L., Meng, W. J., Mei, F., & Glass, J. T. (2007). Effects of applied substrate bias during reactive sputter deposition of nanocomposite tantalum carbide/amorphous hydrocarbon thin films. Thin solid films, 515(13), 5403-5410.

[22] Poladi, A., Semnani, H. M., Emadoddin, E., Mahboubi, F., & Ghomi, H. R. (2019). Nanostructured TaC film deposited by reactive magnetron sputtering: Influence of gas concentration on structural, mechanical, wear and corrosion properties. Ceramics International, 45(7), 8095-8107.

[23] Balani, K., Gonzalez, G., Agarwal, A., Hickman, R., O'Dell, J. S., & Seal, S. (2006). Synthesis, microstructural characterization, and mechanical property evaluation of vacuum plasma sprayed tantalum carbide. Journal of the American Ceramic Society, 89(4), 1419-1425.

[24] Ali, M., & Ürgen, M. (2012). Tantalum carbide-graphite composite film synthesized by hot-filament chemical vapor deposition. Pure and Applied Chemistry, 84(12), 2499-2506.

[25] Cotton, D., Jacquet, P., Faure, S., Vignal, V. (2017). Epitaxial growth of tantalum carbides by low carbon flow carburizing. Materials Chemistry and Physics, 192, 170-180.

[26] Gassner, G., Patscheider, J., Mayrhofer, P. H., Šturm, S., Scheu, C., Mitterer, C. (2007). Tribological properties of nanocomposite CrC x/aC: H thin films. Tribology Letters, 27(1), 97-104.

[27] Shuo, W., Kan, Z., Tao, A., Chaoquan, H., Qingnan, M., Yuanzhi, M., Mao, W., Weitao, Z. (2015). Structure, mechanical and tribological properties of HfCx films deposited by reactive magnetron sputtering. Applied Surface Science, 327, 68-76.

[28] Gulbiński, W., Mathur, S., Shen, H., Suszko, T., Gilewicz, A., Warcholiński, B. (2005). Evaluation of phase, composition, microstructure and properties in TiC/aC: H thin films deposited by magnetron sputtering. Applied Surface Science, 239(3-4), 302-310.

[29] Voevodin, A. A., Capano, M. A., Safriet, A. J., Donley, M. S., Zabinski, J. S. (1996). Combined magnetron sputtering and pulsed laser deposition of carbides and diamond-like carbon films. Applied physics letters, 69(2), 188-190.

[30] Souček, P., Daniel, J., Hnilica, J., Bernátová, K., Zábranský, L., Buršíková, V., Stupavská, M., Vašina, P. (2017). Superhard nanocomposite nc-TiC/aC: H coatings: The effect of HiPIMS on coating microstructure and mechanical properties. Surface and Coatings Technology, 311, 257-267.

[31] Ren, X., Zhu, H., Liu, N., Wei, Q., Pu, J., Ma, L., Wang, Y., Xie, Y., Wei, B., Yu, Z., Zhou, K. (2019). Hydrogenated diamond-like carbon film prepared by RF bias assisting magnetron sputtering. Materials Research Express, 6(7), 076403.

[32] Hirvonen, J. P., Koskinen, J., Kaukonen, M., Nieminen, R., Scheibe, H. J. (1997). Dynamic relaxation of the elastic properties of hard carbon films. Journal of applied physics, 81(11), 7248-7254.

[33] Jiang, K. M., Zhao, D. Q., Jiang, X., Huang, Q., Miao, L. J., Lu, H. M., Li, Y. (2018). Electronic-structure, corrosion and mechanical properties of nc-CrC/aC: H films deposited by multi-arc ion plating. Journal of Alloys and Compounds, 750, 560-569.

[34] Samuelsson, M., Sarakinos, K., Högberg, H., Lewin, E., Jansson, U., Wälivaara, B., Ljungcrantz. H., Helmersson, U. (2012). Growth of Ti-C nanocomposite films by reactive high power impulse magnetron sputtering under industrial conditions. Surface and Coatings Technology, 206(8-9), 2396-2402.

[35] Alami, J., Persson, P. Å., Music, D., Gudmundsson, J. T., Bohlmark, J., Helmersson, U. (2005). Ion-assisted physical vapor deposition for enhanced film

properties on nonflat surfaces. Journal of Vacuum Science & Technology A: Vacuum, Surfaces, and Films, 23(2), 278-280.

[36] Pei, Y. T., Galvan, D., De Hosson, J. T. M. (2005). Nanostructure and properties of TiC/aC: H composite coatings. Acta materialia, 53(17), 4505-4521.

[37] Oliveira, J. C., Ferreira, F., Anders, A., Cavaleiro, A. (2018). Reduced atomic shadowing in HiPIMS: Role of the thermalized metal ions. Applied Surface Science, 433, 934-944.

[38] Benavides, V. J., Salazar, C. D., Espitia, M. E., Devia, D. M., Devia, A. (2008). Study of TiC/aC thin films growth by cathodic arc discharge varying the substrate temperature. Physica Scripta, 2008(T131), 014021.

[39] Lewin, E., Persson, P. Å., Lattemann, M., Stüber, M., Gorgoi, M., Sandell, A., ... & Ulrich, S. (2008). On the origin of a third spectral component of C1s XPS-spectra for nc-TiC/aC nanocomposite thin films. Surface and Coatings Technology, 202(15), 3563-3570.

[40] Galvan, D., Pei, Y. T., & De Hosson, J. T. M. (2006). Influence of deposition parameters on the structure and mechanical properties of nanocomposite coatings. Surface and Coatings Technology, 201(3-4), 590-598.

[41] Hu, Y., Li, L., Cai, X., Chen, Q., Chu, P. K. (2007). Mechanical and tribological properties of TiC/amorphous hydrogenated carbon composite coatings fabricated by DC magnetron sputtering with and without sample bias. Diamond and related materials, 16(1), 181-186.

[42] Patscheider, J. (2003). Nanocomposite hard coatings for wear protection. MRS bulletin, 28(3), 180-183.

[43] Hong, Q. J., & van de Walle, A. (2015). Prediction of the material with highest known melting point from ab initio molecular dynamics calculations. Physical Review B, 92(2), 020104.

[44] Musil, J. (2012). Hard nanocomposite coatings: Thermal stability, oxidation resistance and toughness. Surface and Coatings Technology, 207, 50-65.

[45] Blažek, J., Musil, J., Stupka, P., Čerstvý, R., & Houška, J. (2011). Properties of nanocrystalline Al–Cu–O films reactively sputtered by DC pulse dual magnetron. Applied Surface Science, 258(5), 1762-1767.

[46] Voevodin, A. A., Zabinski, J. S. (1998). Load-adaptive crystalline–amorphous nanocomposites. Journal of materials Science, 33(2), 319-327.

[47] Voevodin, A. A., Zabinski, J. S. (2000). Supertough wear-resistant coatings with 'chameleon'surface adaptation. Thin Solid Films, 370(1-2), 223-231.

[48] Zhang, K., Wen, M., Meng, Q. N., Hu, C. Q., Li, X., Liu, C., & Zheng, W. T. (2012). Effects of substrate bias voltage on the microstructure, mechanical properties and tribological behavior of reactive sputtered niobium carbide films. Surface and Coatings Technology, 212, 185-191.

[49] Musil, J., Kunc, F., Zeman, H., Polakova, H. (2002). Relationships between hardness, Young's modulus and elastic recovery in hard nanocomposite coatings. Surface and Coatings Technology, 154(2-3), 304-313.

[50] Musil, J., Jirout, M. (2007). Toughness of hard nanostructured ceramic thin films. Surface and Coatings Technology, 201(9-11), 5148-5152.

[51] Suh, N. P. (1977). An overview of the delamination theory of wear. Wear, 44(1), 1-16.

[52] Li, H. J., Fu, Q. G., Shi, X. H., Li, K. Z., & Hu, Z. B. (2006). SiC whisker-toughened SiC oxidation protective coating for carbon/carbon composites. Carbon, 3(44), 602-605.

[53] Osswald, S., Yushin, G., Mochalin, V., Kucheyev, S. O., Gogotsi, Y. (2006). Control of sp2/sp3 carbon ratio and surface chemistry of nanodiamond powders by selective oxidation in air. Journal of the American Chemical Society, 128(35), 11635-11642.

Chapter 4 HfC/a-C:H films deposited in HiPIMS and DC magnetron sputtering

For the study of transition metal carbide films prepared by HiPIMS, TaC/a-C:H films were systematically investigated in the previous chapter. It has been demonstrated that the plasma characteristics of HiPIMS discharge can effectively improve the hardness, toughness, tribological performance and oxidation resistance of the TaC/a-C:H films. In this chapter, the hafnium carbide film, serves as another hotspot in transition metal carbon-based nanocomposites, is explored. HfC/a-C:H films are deposited by HiPIMS and DC magnetron sputtering in the mixed gas environment of Ar/C_2H_2. The C_2H_2 was used as the carbon source and regulated between 10 sccm and 20 sccm with a step size of 2 sccm. The chemical bonding state, structure, and morphology are characterized. The residual stress, mechanical properties, tribological performance, thermal stability as well as oxidation resistance of HfC/a-C:H films are carried out. Moreover, the properties of HfC/a-C:H films deposited under different carbon contents and different deposition conditions, DC and HiPIMS, are compared and analyzed.

4.1 Research background and purpose

Among a variety of transition metal carbides, HfC is characterized by the highest melting temperature (3959 °C), high mechanical properties, good resistance to chemical attack and ablation, and high temperature phase stability [1][2][3][4]. G. Li *et al.* [5] investigated the structure and mechanical properties of hafnium carbide coatings as a function of carbon content synthesized by reactive magnetron sputtering. Y. L. Wang *et al.* [6] studied the phase composition, microstructure and ablation properties of the HfC coating prepared by low pressure chemical vapor deposition (LPCVD). The results showed that the HfC coating with compact structure exhibits dense surface and excellent ablation resistance. H. I. Yoo *et al.* [7] reported the morphology, growth behavior and ablation behavior of HfC films deposited by vacuum plasma spray systems. S, Wang *et al.* [8] studied the structure, mechanical and tribological properties of HfC films deposited by reactive magnetron sputtering with -150 V substrate bias voltage. However, published studies on HfC/a-C:H films have mainly focused on exploring ablation behavior. The research on the microstructure, mechanical and tribological properties of HfC/a-C:H films is still scarce. Also, to our knowledge, no study has been conducted on the thermal stability and oxidation resistance of HfC/a-C:H films. The operating conditions can easily make the protective films work at very high temperature, which impair the performence of the protective films. Moreover, current environmental conditions limit the use of lubricants and coolant liquids. Therefore, investigating and optimizing the thermal stability of the film (making it function normally in high temperature environments) is urgently needed and critical for extending the service life of the film. Meanwhile, the high temperature oxidation environment is also an inevitable condition for HfC/a-C:H film. It is thus vitally important to clarify how does the thermal performance, thermal stability and oxidation resistance, in the HfC/a-C:H films.

Magnetron sputtering is a mature film preparation technology widely used at present. The growth process of thin films supported by magnetron sputtering, especially the atomistic process during the nucleation stage, is not only controlled by thermodynamics but also by kinetics, and greatly deviates from equilibrium conditions. Among them, the kinetic control can be effectively tailored by deposition parameters, such as by varying working pressure and applying substrate bias, thereby tuning the phase composition and nanocomposite structure of the film. High power impulse magnetron sputtering (HiPIMS) technology is a recently emerged advanced fabrication approach in the field of thin films, characterized by the high ionization rate and impulse power supply mode. Benefiting from these features, the uniqueness of HiPIMS lies in that it provides a more flexible and multi-dimensional control means on atomic-scale manipulations (toward some specific requirements) over the film growth process, compared with traditional direct current magnetron sputtering. For example, by employing the auxiliary magnetic field configuration or substrate bias in HiPIMS, the kinetic energy of film-forming ions can be changed during the film growth. Ions with enhanced bombardment energy will impact a few atomic layers beneath the growing interface and delivers sufficient mobility for atomic rearrangement. Correspondingly, the structure, growth morphology, and most relevant properties of the film can be tailored. Therefore, HiPIMS technology is expected to have extraordinary potential in optimizing the performance of HfC/a-C:H films. Unfortunately, the investigation of HfC/a-C:H film prepared by HiPIMS has not yet been reported anywhere up to now. Trying to clarify above points, nanocomposite HfC/a-C:H films deposited by HiPIMS in the mixed gas environment Ar/C_2H_2 is investigated.

4.2 Film characteristics

4.2.1 Chemical bonding state

Fig. 4-1 displays the XPS C 1s spectra for HfC/a-C:H films with different C_2H_2 flow rates deposited in DC and HiPIMS conditions. It can be observed that for both DC and HiPIMS deposited films, there are four main types of carbon present in different chemical surroundings.

The obvious peak at 281.2 eV is identified as C-Hf bond (hafnium carbide phase), and the peaks at 284.5 eV and 285.4 eV correspond to sp^2-C and sp^3-C bonds (amorphous carbon phase), respectively. The peak at 286.8 eV represents O-C bond. Note that the peak at 282.5 eV between the C-Hf peak and the amorphous carbon peak is labeled as the C-Hf*, which is ascribed to the interface bonding between amorphous carbon phase and metal carbide phase. This similar peak in the HfC/a-C:H film had been observed in [8]. It pointed out that the C-Hf* peak originates from the core electrons at the interface between the carbide and the amorphous carbon, and the induced vacancy density could strengthen the hardness. Besides, this type of peak in nc-MeC/a-C:H films (Me=Cr, Zr, Ti) have been reported several times [9][10][11]. Here we consider the fraction of hafnium carbide bond as the sum of C-Hf and C-Hf* bonds. The fractions of hafnium carbide bond (C-Hf and C-Hf*) and amorphous carbon bond (sp^2-C and sp^3-C), the amorphous carbon content as well as the stoichiometric ratio of HfC grains, obtained by comparing the fitting areas of different peaks in corresponding C 1s spectra (presented in Fig. 4-1), were listed in Table 4-1.

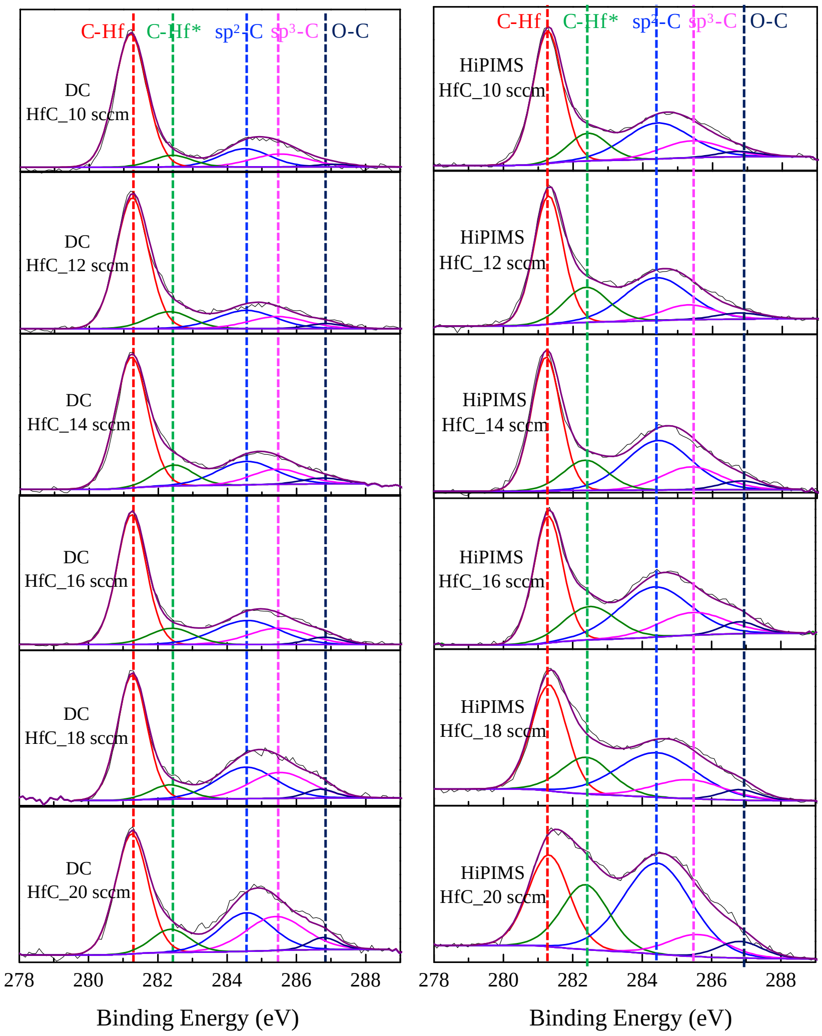

Figure 4-1. High resolution XPS spectra C 1s of HfC/a-C:H films deposited in (a) DC and (b) HiPIMS as a function of C_2H_2 flow rate.

As C_2H_2 flow rate grows, for both DC and HiPIMS deposited films, the carbide fraction (the sum of C-Hf and C-Hf*) shows a decreasing trend while the sp^2-C fraction presents a rising trend. From 10 to 20 sccm of C_2H_2, the fraction of hafnium carbide bond decrease from 73.4 to 50.4 at.% for DC deposited films and decrease from 60.2 to 43.2 at.% for HiPIMS deposited films. The sp^2-C fraction increases from 12.9 to 25.6 at.% for DC deposited films and increases from 27.2 to 40.8 at.% for HiPIMS deposited films. Note that with the increase of C_2H_2 flow rate, the evolution of sp^3-C fraction has deposition condition-dependence. In DC condition, the fraction of sp^3-C bond gradually increases with the increase of C_2H_2 flow rate. However, in HiPIMS condition, it first increases as C_2H_2 goes from 10 sccm to 16 sccm and then begins to decrease as C_2H_2 exceeds 16 sccm. This may be related to the weakening of the energy transferred from the bombarding plasma to the growing film. Strong bombardment energy is well known to promote the formation of sp^3-C fraction in the amorphous carbon matrix during the growth of the film. However, as the increasing C_2H_2 flow rate is introduced into the reaction chamber, collision events between particles are also increased. When C_2H_2 flow rate exceeds 16 sccm, an enhanced collision event may cause loss of partial energy of the film-forming species, the kinetic energy of the species bombarding the substrate is thus lost and the sp^3-C fraction is lowered.

In addition, the amorphous carbon content (a-C:H content) and the stoichiometric ratio of the HfC grain, shown in Table 4-1, increase with C_2H_2 flow rate in both DC and HiPIMS depositd films. The a-C:H content increases from 10.60 to 28.23 at.% in DC deposited film and from 21.05 to 36.18 at.% in HiPIMS deposited film as C_2H_2 flow rate rises from 10 to 20 sccm. The stoichiometric ratio increases in the range of (0.58, 0.75) for DC deposited films and in the range of (0.76, 0.88) for HiPIMS deposited films. In addition, the a-C:H content and stoichiometric ratio of HiPIMS deposited films are greater than those of DC deposited films at each C_2H_2 flow rate.

Overall, the HiPIMS deposited HfC/a-C:H films have higher carbon incorporation in both amorphous carbon phase and carbide phase, confirmed by the higher a-C:H content and higher stoichiometric ratio. This higher C element incorporation in the film prepared by HiPIMS is consistent with the results observed in TaC/a-C:H films in Chapter 3, explaining by the higher reactivity between target element and C_2H_2 during the plasma discharge and at the growing interface (due to the higher ionization rate and higher bombardment energy). Moreover, it is worth noting that in the C_2H_2 interval of 10 to 20 sccm, the incremental span of the carbon content in the DC deposited film (from 43.4 to 59.1 at.%) is large than that in the HiPIMS deposited films (from 55.1 to 66.1 at.%) despite its lower total content. It is characterized by the larger growth rate of stoichiometric ratio and a-C:H content. From 10 to 20 sccm of C_2H_2 flow rate, the a-C:H content in the DC deposited film increases by 17.62 at.% (from 10.6 to 28.22 at.%)

and the stoichiometric ratio increment is 0.17 (from 0.58 to 0.75). While in the HiPIMS deposited films, the content of a-C:H increases by 15.13 at.% (from 21.05 to 36.18 at.%), the stoichiometric ratio increases by 0.12 (from 0.76 to 0.88).

Table 4-1: The relative amount of chemical bonds of C-Hf, C-Hf*, sp^2-C and sp^3-C, and stoichiometric ratio *x* of HfC grains and a-C:H content in the HfC/a-C:H films deposited in DC and HiPIMS conditions with different C_2H_2 flow rates.

Batch no.	Composition [at.%]		Types of bonding for C 1s XPS [at.%]					a-C:H [at.%]	HfC_x
	Hf	C	C-Hf	C-Hf*	sp^2-C	sp^3-C	C-O		
				DC					
10	56.6	43.4	61.8	11.6	12.9	10.9	2.8	10.60	0.58
12	53.8	46.2	60.4	12.5	14.9	9.7	2.5	11.69	0.64
14	51.5	48.5	56.1	12.4	18.0	10.6	2.9	14.31	0.67
16	47.7	52.3	52.1	9.8	21.2	13.4	3.5	18.74	0.70
18	42.6	57.4	45.5	7.1	24.7	19.6	3.1	26.23	0.73
20	40.9	59.1	40.2	10.2	25.6	20.5	3.5	28.22	0.75
				HiPIMS					
10	44.9	55.1	46.5	13.7	27.2	10.1	2.5	21.05	0.76
12	42.2	57.8	42.2	15.7	30.0	9.6	2.5	23.47	0.81
14	39.5	60.5	38.7	14.1	31.5	12.3	3.4	27.40	0.84
16	38.1	61.9	34.7	16.6	33.0	14.7	1.0	29.78	0.84
18	36.4	63.6	32.5	15.9	35.6	12.3	3.7	31.63	0.88
20	33.9	66.1	23.0	20.2	40.8	11.5	4.5	36.18	0.88

This is understood by the notion that the discharge process of the HiPIMS technology is more stable. We know that in addition to the reactivity of the plasma and the bombardment energy of the adatoms at the growing interface, the composition of the deposited film also depends on the coverage degree of the target surface by the corresponding compound during the reactive sputtering process. As the flow rate of the reaction gas increases to a certain extent, the target surface will be converted from metal to compound, thus causing the reaction gas species to be more doped into the film, which is referred to as transition region [12]. It has been demonstrated that the transition region is unstable in DC condition, that is, the sudden change in target coverage and rapid drift and/or hysteresis in deposition parameters (target voltage, reactive gas partial pressure, etc.) induced by the small change in reaction gas flow are often observed [12][13]. It will lead to a dramatic variation in the film composition. However, in HiPIMS condition, the transition region is considered to be less likely to occur, and if it occurs, it is more stable and less abrupt, due to the high energy density and low duty cycle during the plasma discharge process. The high energy density during the pulse time-on causes intense target etching and the rarefaction of the reactive gas. Moreover, the plasma reactivity is quite low in the pulse time-off. Both of then inhibit the formation and attachment of compound species on the target surface [14][15]. This feature has been experimentally observed and discussed in previous work [13][16][17]. For the HfC/a-C:H films in our case, it can be considered that in the C_2H_2 interval of 10 to 20 sccm, the transition of (target) metal sputtering to the compound sputtering mode in DC condition occurs with greater probability and is less stable (with dramatic change in parameter drift or in target coverage) than that in HiPIMS. As a result, the incremental span of C content carried in the species for growing DC film (sputtered from the target surface before the reaction with the reactive gas) is larger. Therefore, in the same interval of the C_2H_2 flow rate, the span of C content in the DC deposited film is wider. It is consistent with the results observed in [18].

4.2.2 Microstructure

The X-ray diffractograms of HfC/a-C:H films deposited by DC and HiPIMS with different C_2H_2 flow rates are presented in Fig. 4-2. For DC deposited films, the diffraction peaks at $2\theta \approx 39.2°$, $45.5°$ and $66.4°$ are observed, which are assigned to (111), (200) and (220) for face-centered cubic HfC (Jcpds: 03-065-8751). From 10 to

16 sccm of C_2H_2, the crystalline HfC phase exhibits a strong texture (111). As C_2H_2 flow rate further raises to 18 and 20 sccm, the crystalline phase transfers to a random orientation in which the diffraction peaks contain (111), (200), and (220) planes.

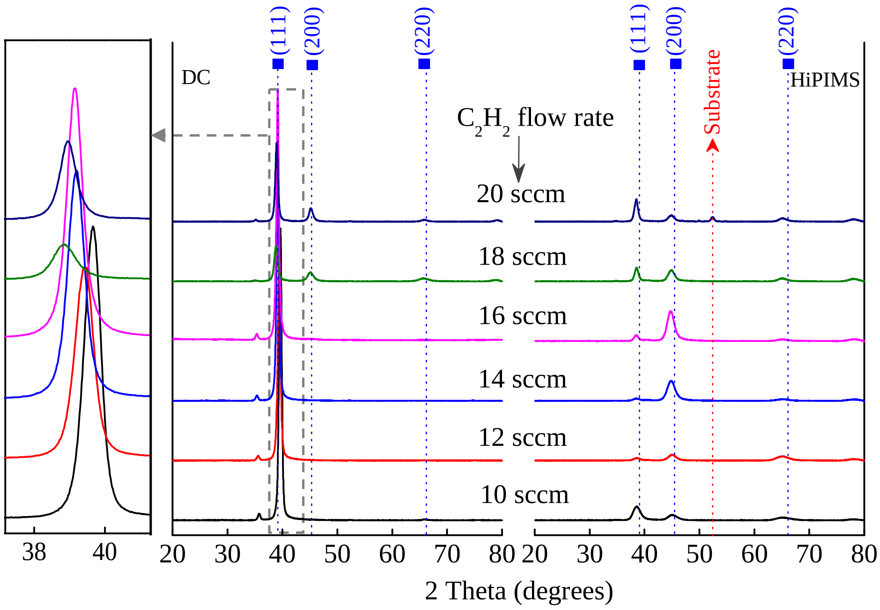

Figure 4-2. X-ray diffractograms of HfC/a-C:H films deposited in DC (left) and in HiPIMS (right) with different C_2H_2 flow rates.

For HiPIMS deposited film at 10 sccm C_2H_2, a strong peak at $2\theta \approx 39.2°$ and a relatively weak peak at $2\theta \approx 45.5°$ occur, which are assigned to (111) and (200) planes for fcc HfC (Jcpds: 03-065-8751). When C_2H_2 flow rate increases from 12 to 16 sccm, the (111) plane is suppressed while the (200) plane is promoted with the gradual increase in intensity, exhibiting a (200) preferred orientation. As C_2H_2 flow rate reaches 18 sccm, a randomly oriented crystal phase appears again, and then the (111) plane gradually becomes dominant at 20 sccm C_2H_2 flow rate. It is known that the (200) lattice plane has a higher surface free energy in fcc structure. Such a transition of phase composition from (200) preferred orientation to random orientation and then to (111) plane in HiPIMS films may derive from the reduced kinetic energy of the bombardment plasma caused by the enhanced collision events under high C_2H_2 flow rate. Reduced bombardment energy weaken the average energy received per unit area of the substrate, which cannot continue to support the growth of crystal planes with high surface free energy, thereby driving the growth of (111) plane. It is worth noting that this transition of the crystalline phase corresponds to the decrease of the sp^3-C fraction in the film after C_2H_2 flow rate exceeds 16 sccm (indicated by XPS result). Both of them confirm the inference that the bombardment energy of the film-forming species is weakened at high C_2H_2 flow rate. Furthermore, whether in DC or in HiPIMS conditions, the diffraction peaks gradually shift toward the lower angle as the C_2H_2 flow rate increases. This corresponds to the occurrence of compressive stress inside the HfC/a-C:H films and/or the lattice expansion caused by the stoichiometric change of the HfC grains.

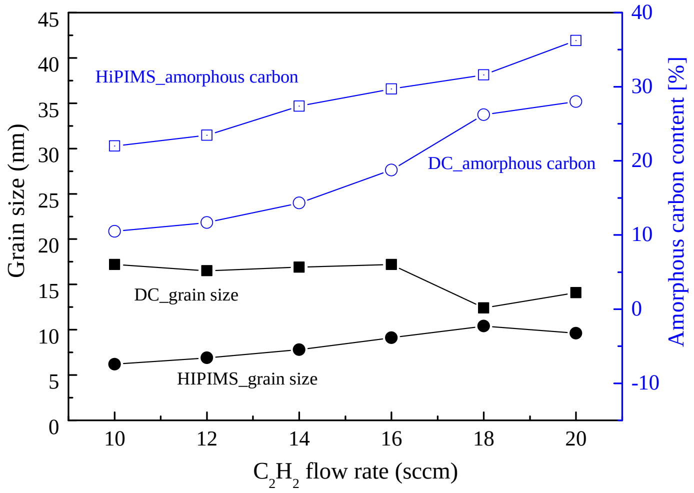

Figure 4-3. Grain size (black lines) and amorphous carbon content (blue lines) of HfC/a-C:H films deposited in DC and in HiPIMS with different C_2H_2 flow rates.

The average grain size of the HfC/a-C:H films deposited in DC and HiPIMS, calculated using the Scherrer’s formula from the full width at half maximum (FWHM) of the diffraction peak, is displayed in Fig. 4-3. It can be observed that the grain size of DC deposited film remains almost unchanged at 17 nm in the interval of 10 to 16 sccm of C_2H_2 flow rate, and then starts to decrease to 12.4 nm when C_2H_2 flow rate reaches 18 sccm. For the films deposited from 10 to 16 sccm C_2H_2, the constant grain size is maintained by the low energy density of the DC plasma. Since the ionization rate and energy of the film-forming species (Hf and C) during DC discharge process are insufficient, the degree of reaction is inadequate in the plasma and at the growing interface. It is thus easier to form amorphous carbon phase instead of growing carbide

HfC grains. Moreover, the kinetic energy of the film-forming species would be further reduced due to the greater collision probability with increasing C_2H_2, which causes the carbide grain to be more difficult to grow even if the carbon source increases. Therefore, from 10 to 16 sccm C_2H_2 flow rate, the content of amorphous carbon is gradually increased while the size of the HfC grain remains unchanged. The drop in grain size at 18 sccm C_2H_2 flow rate is due to the sudden increase in amorphous carbon content (from 18.74 to 26.24 at.%, indicated by XPS spectrum) of the film. A larger amount of amorphous carbon matrix encapsulates HfC grains more completely and thus inhibits their growth. Consequently, the grain growth is suppressed in the competition of amorphous carbon formation and grain growth.

For HiPIMS deposited films, the grain size first increases from 6.2 nm to 10.4 nm in the C_2H_2 interval of 10 to 18 sccm, and then decreases to 9.6 nm with C_2H_2 flow rate reaching 20 sccm. The gradual coarsening of the grains is due to the slower growth rate of amorphous carbon content with the increasing C_2H_2 flow rate (compared to that of DC film). The slower the growth of the amorphous carbon content, the less significant the inhibitory effect on grain growth. Moreover, the bombardment energy of the species in HiPIMS is stronger than that in DC. Therefore, the grain size of the HiPIMS film is not suppressed but is promoted instead. Similar to the drop in grain size of the DC film, the grain refinement of the HiPIMS deposited film occurring at 20 sccm C_2H_2 is also caused by the large increase in the amorphous carbon matrix. Meanwhile, it is also contributed by the film-forming species with reduced bombardment energy, caused by the higher density of reactive gas.

Comparing the evolution of the grain size of the films deposited by DC and HiPIMS, it can be found that the turning point (starting refinement) in the grain size development of the HiPIMS films lags behind that of the DC films (which occurs at 16 sccm C_2H_2 flow rate). One reason is that the sharp increase in the amorphous carbon content of the HiPIMS film occurs after 18 sccm, which falls behind that of the DC film. The inhibition of grain growth by amorphous carbon is accordingly delayed. Another reason is that under the same C_2H_2 flow rate, the bombardment energy of the film-forming species in the HiPIMS discharge is stronger (which is conducive to the growth of crystal grains in the film). Therefore, for HiPIMS discharge, to achieve a lower bombardment energy level that is insufficient to drive grain growth, more collisions induced by a higher C_2H_2 flow rate are required. The turning point of grain refinement of the HiPIMS film is thus delayed and occurs at a higher C_2H_2 flow rate. In addition, it has been found that the inhibition effect of the amorphous carbon matrix on the grain growth in HiPIMS deposited film is weaker than that in DC deposited film, even though the HiPIMS film holds higher amounts of amorphous carbon and finer grains. This is primarily due to the stronger bombardment energy of the HiPIMS plasma. Different from the DC discharge characteristics, the bombardment energy of HiPIMS plasma is not lost too much by the collision events, even at high C_2H_2 flow rate. The bombardment energy of HiPIMS plasma is not only derived from the energy delivered by the sputtering process on the target surface, but also from the self-biasing potential due to the high ionization rate. After losing some of the kinetic energy in the enhanced collision events, the HiPIMS plasma can regain energy from the electric field. In this case, the degree of reaction of the Hf particles reaching the substrate with carbon at the growing interface is higher than that of DC deposited film. Therefore, the grain growth is promoted to be superior in the competition (between amorphous carbon inhibition and grain growth) in the HiPIMS deposited films.

4.2.3 Morphology

Fig. 4-4 exhibits the SEM micrographs of the fracture cross-section for the HfC/a-C:H films deposited in DC and HiPIMS with different C_2H_2 flow rates. Among them, the upper row and the lower row represent the results of DC deposited films and of HiPIMS deposited films, respectively.

From Fig. 4-4, both DC and HiPIMS deposited films exhibit a character of columnar structure throughout the whole film thickness with a growth direction orthogonal to the substrate surface. At low C_2H_2 flow rate of 10 sccm, a relatively loose columnar structure with a visible inter-column gap is observed in the DC deposited film, whereas a finer columnar structure and an inconspicuous column gap are observed in the HiPIMS deposited film. As C_2H_2 flow rate increases from 12 to 20 sccm, the columnar crystals of both DC and HiPIMS deposited films begin to refine and the morphologies become more compact. Particularly for HiPIMS deposited films, the boundaries between adjacent columns are significantly tighter than those of DC deposited films. Moreover, the duplex morphology consisting of stacking and dense glassy layer and followed compact columnar crystal layer appears in HiPIMS film deposited at 20 sccm C_2H_2 (shown in Fig. 4-4(h)). It indicates that the morphology of the HfC/a-C:H film is gradually densified with the C content. Moreover, the HiPIMS deposition condition is conducive to higher compactness. This higher densification in HiPIMS condition is ascribed to two aspects. On the one hand, the higher energy of the HiPIMS plasma increases the mobility of the adatoms and drives them to fill the micro-voids in the film, which makes the micro-morphology of the film denser. On the other hand, it is determined by the higher content of amorphous carbon of the HiPIMS deposited films. Apart from distribution between HfC grains, amorphous carbon is also concentrated on the columnar boundaries (as demonstrated by elemental mapping with energy filtering TEM in [19]). The filling of the columnar boundaries by amorphous carbon makes the boundaries less visible.

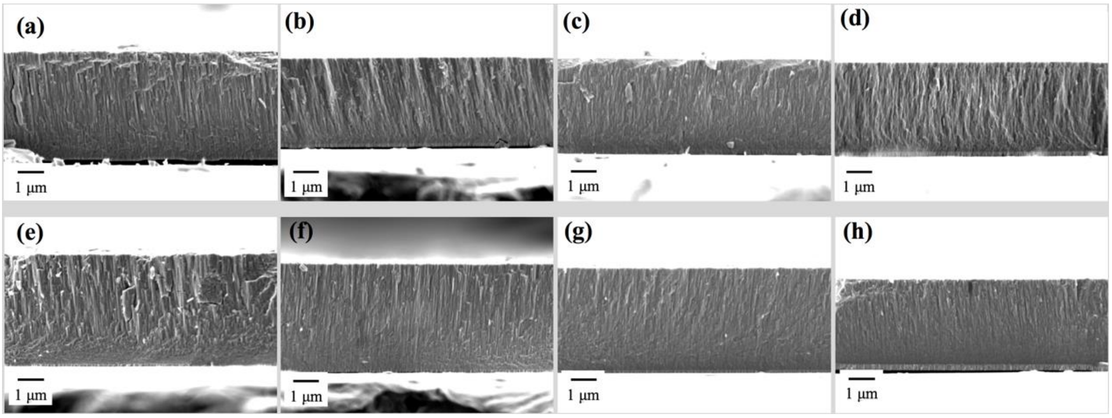

Figure 4-4. SEM micrographs of cross-section of HfC/a-C:H films deposited in DC (upper row, a-d) and in HiPIMS (lower row, e-h) with various C_2H_2 flow rate: (a, e) 10 sccm, (b, f) 14 sccm, (c, g) 18 sccm, and (d, h) 20 sccm.

4.3 Film properties

4.3.1 Mechanical properties

Fig. 4-5 shows the hardness and effective Young’s modulus of the HfC/a-C:H films with maximum indentation depth of less than 10% of the film thickness. It was found that the variations of the hardness and effective Young’s modulus are related to the C_2H_2 flow rate and deposition conditions. For films deposited in different deposition conditions, the hardness shows a similar trend with the increase of C_2H_2 flow rate, while the evolution of effective Young’s modulus is different (i.e., deposition system dependence).

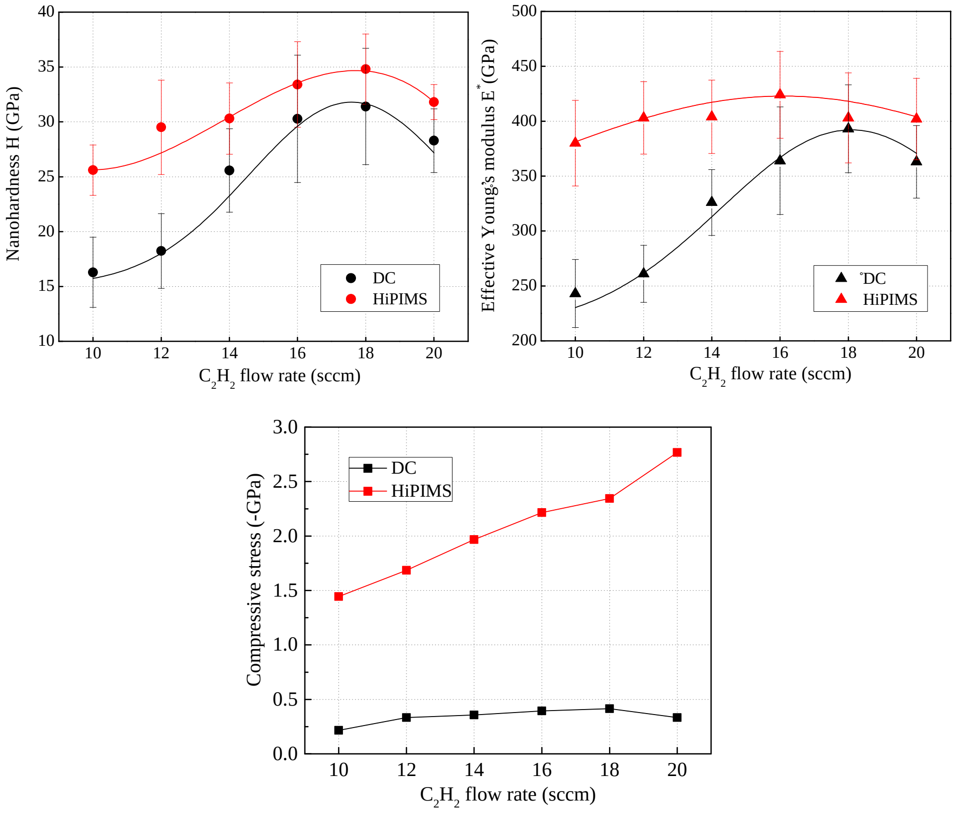

Figure 4-5. The hardness H, effective Young’s modulus E^* and compressive stress of the HfC/a-C:H films deposited in DC (black) and HiPIMS (red) with various C_2H_2 flow rates.

For DC deposited films, hardness and effective Young’s modulus show the same evolution trend. From 10 to 20 sccm of C_2H_2 flow rate, they increase first and then decrease. The maximum values are obtained at 18 sccm of C_2H_2. The hardness increases from 16.3 to 31.3 GPa and then decreases to 28.2 GPa, while effective Young's modulus increases from 242.9 to 392.3 GPa and then decreases to 362.7 GPa. In the interval of 10 to 16 sccm, the grain size of the film remains substantially unchanged, while the amorphous carbon content gradually increases. The mean grain separation is thus gradually increased, which induces grain incoherent strain and effectively restricts the deformation caused by dislocation movement, thereby increasing hardness. When C_2H_2 flow rate reaches 18 sccm, the mean grain separation continues to widen due to the smallest grain size and the large increase in amorphous carbon, resulting in further improved hardness. Moreover, from 10 to 18 sccm, the increase in hardness is also contributed by increased content of sp^3-C (for hardening amorphous carbon network), larger stoichiometric ratio of HfC grains, and stronger compressive stress. As C_2H_2 flow rate further increases to 20 sccm, the mean grain separation may begin to narrow due to the re-coarsened grains and the slightly increased amorphous carbon content (compared to that at 18 sccm). Therefore, the deformation due to dislocation motion may not be effectively prevented, thus degrading the film hardness. In addition, note that the compressive stress decreases at 20 sccm of C_2H_2, the similar phenomenon has been reported in [8]. The higher compressive stress in the film usually occurs through energetic ion bombardment assisting in crystalline size reduction and grain boundary densification. However, the enhancement of the collision event at 20 sccm C_2H_2 may cause the energy of the ion bombardment to be partially weakened, the compressive stress is thus reduced. This reduction in compressive stress in the film also contributes to the deterioration of hardness here. Besides, although the stoichiometric ratio and sp^3/sp^2 -C value continue to increase and the morphology of the columnar crystal is more compact at 20 sccm C_2H_2, they have no positive effect on hardness. Therefore, it can be concluded that for DC deposited films, the factors that dominate the mechanical properties of the film are mean grain separation and compressive stress.

For HiPIMS deposited films, hardness and effective Young's modulus show different trends with increasing C_2H_2 flow rate. The hardness gradually increases from 25.6 to 34.8 GPa as the C_2H_2 flow rate increases from 10 to 18 sccm. It is derived from the monotonic increase in mean grain separation, the densification of morphology, the increases in compressive stress and sp^3-C content, and the enhanced stoichiometric ratio of HfC grains. Substoichiometric hardening mechanism has been mentioned in Chapter 3 for TaC/a-C:H films, illustrating that non-metal deficiency is the major source of substoichiometric, and the induced vacancies act as pinning centers, thereby inhibiting dislocation motion and thus improving mechanical properties. When C_2H_2 flow rate exceeds 18 sccm, the hardness begins to decrease. It is due to the combined effect of excessively broad mean grain separation and significantly reduced ratio of sp^3/sp^2 -C. This excessively wide average grain separation is formed by the refined grain size and the surge of the amorphous carbon content occurring at 20 sccm C_2H_2, which enhances the proportion of the amorphous carbon phase in the two-phase (hard phase HfC grains and soft amorphous carbon phase) affecting the film mechanical properties and provide space for micro-crack nucleation, thus degrading the hardness. The evolution of effective Young’s modulus is relatively flat. It exhibits a very slight upward trend first in the range of (380, 424) GPa and then decreases to 402 GPa. The maximum value of 424 GPa is achieved at 16 sccm of C_2H_2 flow rate. Such a trend may be related to the fraction of $C\text{-}Hf^*$ bond present in the HfC/a-C:H films. The $C\text{-}Hf^*$ bond is attributed to the valence charge transfer at the interface between crystalline phase HfC and amorphous carbon phase. Through the *ab* initio density functional theory (DFT) calculations [20][21] and X-ray and ultraviolet photoelectron spectroscopies [9], it has been proven that the increase in valence charge transfer not only strengthens the covalent bonds across the interface, but also makes some of the carbide bonds more ionic. Both of them can increase the bonding energy and strengthen the chemical bonds in the film. Since effective Young’s modulus of the film is intrinsically related to the chemical bonds, the increase in valence charge transfer is conducive to the enhancement of effective Young’s modulus, especially for the HfC/a-C:H films deposited at low flow rate of C_2H_2 (which have weaker chemical bond strength due to higher C vacancies). Consequently, from 10 to 16 sccm of C_2H_2, effective Young’s modulus does not exhibit a similar evolution to that of DC deposited film, but achieve a higher value. The decrease in effective Young’s modulus at 18 sccm and 20 sccm may be associated with the lower level of C-Hf* bond and the reduced hardness [22], respectively.

Furthermore, the mechanical properties of HiPIMS deposited films surpass those of DC deposited films at all C_2H_2 flow rates. The finer grains and higher amorphous carbon content (which make nanostructures more resistant to dislocation movement), stronger compressive stress, higher stoichiometric ratio of HfC grains, and more compact morphology of the HiPIMS deposited films are responsible for this better performance. The essential cause supporting the above characteristics of HiPIMS films is the high energy and high density bombardment characteristics of the HiPIMS plasma.

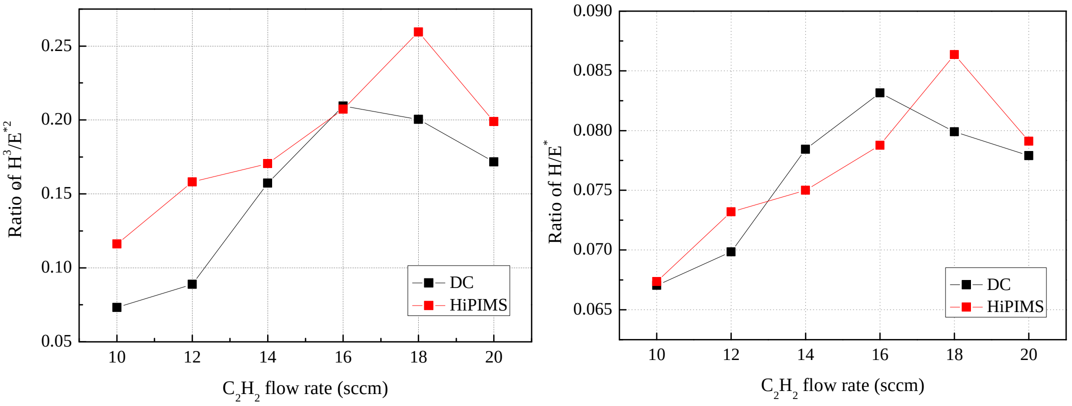

Figure 4-6. Ratios of H^3/E^{*2} and H/E* for HfC/a-C:H films deposited in DC (black) and HiPIMS (red) conditions with various C_2H_2 flow rate.

Despite the high hardness of suchlike MeC/a-C:H films, their inherent brittleness is disadvantageous when subjected to high loads or long-term friction since catastrophic fracture and film failure may occur. Therefore, the discussion of the mechanical behavior, characterized by the ratios H/E* and H^3/E^{*2}, of such films is necessary. The failure of the elastic strain of film depends on the ratio H/E* that characterizes the resistance of the material to elastic deformation, while the material's ability to dissipate energy during plastic deformation is characterized by the ratio H^3/E^{*2}. It has been demonstrated that HiPIMS condition strongly influences the chemical bonding state, grain size, morphology, residual stress, ratio sp^3/sp^2 -C and stoichiometric ratio of the HfC/a-C:H film. These film features modulated by HiPIMS condition are desirable since they have the potential to improve toughness and resistance of the material against plastic deformation (i.e., higher values of H/E^* and H^3/E^{*2}), which are crucial for improving the tribological performance of the film. Therefore, the ratios H/E^* and H^3/E^{*2} of the HfC/a-C:H films deposited in DC and HiPIMS are shown in Fig. 4-6.

It can be observed that the HiPIMS deposited film has a higher H^3/E^{*2} ratio than that of DC deposited film at each C_2H_2 flow rate, which suggests that films prepared in HiPIMS have a stronger resistance to plastic deformation. For the ratio H/E^*, it is lower in HiPIMS deposited film than that in DC deposited film at 14 and 16 sccm C_2H_2, and it is comparable in DC and HiPIMS deposited films at 10 and 20 sccm C_2H_2. Only at 18 sccm C_2H_2, it is higher in HiPIMS deposited film than that in DC deposited film. It indicates that HiPIMS condition facilitates the preparation of tougher HfC/a-C:H films at 18 sccm C_2H_2. In general, it is expected that the HiPIMS deposited films exhibit better toughness because they contain favorable conditions for achieving higher toughness, such as finer grains, stronger compressive stress, and higher stoichiometric ratio. However, the high level of $C\text{-}Hf^*$ bond enhances the strength of covalent bond across the interface in the HfC/a-C:H films and thus increases the effective Young's modulus. It results in a reduction in the absorption and dispersion of strain energy by the film under a certain load, and thus the toughness is lowered. However, although HiPIMS deposited films present similar toughness to that of DC deposited films, their hardness is slightly higher.

4.3.2 Tribological behavior

Fig. 4-7 illustrates the variation of the friction coefficient as a function of sliding laps for eight representative films deposited at 10, 14, 18 and 20 sccm of C_2H_2 in DC and HiPIMS. The friction coefficient value and the wear rate of the HfC/a-C:H films were summarized in Fig. 4-8.

As C_2H_2 flow rate increases from 10 to 20 sccm, the friction coefficient decreases in both DC and HiPIMS deposited films, but with different decline rates depending on deposition conditions. For DC deposited films, the values of friction coefficient get steady at 0.74, 0.69, 0.31 and 0.29 under the C_2H_2 flow rate of 10, 14, 18 and 20 sccm, respectively. It corresponds to the increases in amorphous carbon and sp^2-C contents (from 10.6 to 28.22 at.% and from 12.91 to 25.6 at.%, respectively) in the DC deposited films, which enhance the formation of the easily sheared graphitic tribolayer acting as the solid lubricant.

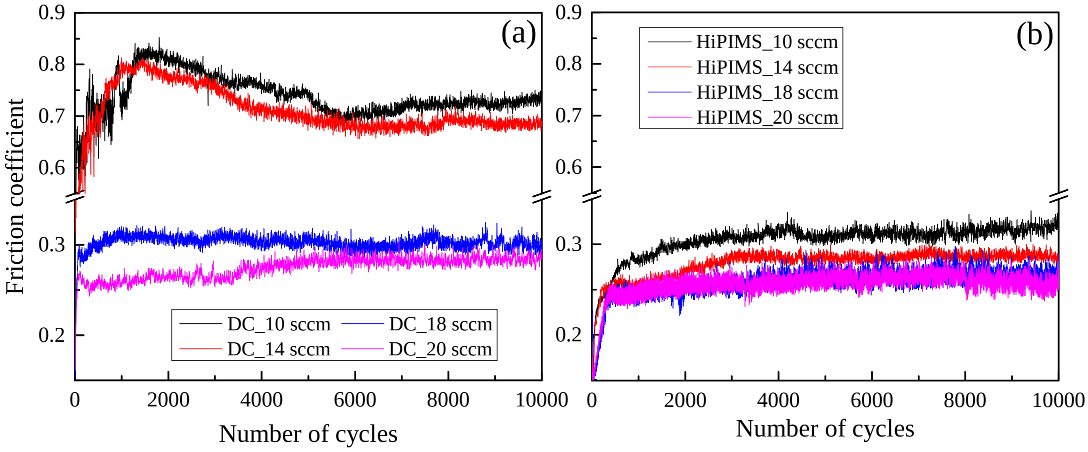

Figure 4-7. Friction coefficient curves of the HfC/a-C:H films deposited in DC and HiPIMS with 10, 14, 18 and 20 sccm C_2H_2.

For HiPIMS deposited films, as C_2H_2 flow rate increases from 10 to 20 sccm, the friction coefficient also presents a gradual reduction trend. After the short run-in period, the friction coefficient is stable at 0.32, 0.28, 0.26 and 0.257 under the C_2H_2 flow rate of 10, 14, 18 and 20 sccm, respectively. However, although the overall low friction coefficients are observed, there is no significant decline rate of friction coefficient with increasing C_2H_2 flow rate. It should be noted that such minor decline rate depends on the total carbon content in the film. It has been reported that for the transition metal carbon-based nanocomposite film, the distribution of the friction coefficient can be distinguished into three zones based on C content [23][24][25], and the correlation between friction coefficient and C content is independent of hydrogen content and deposition system. Below ~55 at.% of C content, the films with friction coefficient larger than 0.4 are observed, which is classified as the first region. In this region, the increase in C content plays a significant role in optimizing the friction coefficient. Over this limit and up to 70 at.% of C content, the second zone is found where the friction coefficient is stationary distributed in the range of (0.2, 0.3), and the changes in C content have a weak effect on the friction coefficient. For high values of C content above 70 at.%, the friction coefficient of the films distribute in the third region, showing smaller values between 0.1 and 0.2. In the case of HfC/a-C:H films deposited in HiPIMS, the C content increases from 55.1 to 66.1 at.% as C_2H_2 flow rate increases from 10 to 20 sccm (Table 1). Obviously, they correspond to the plateau distributed friction coefficient located in the second zone. Therefore, the friction coefficient of the HiPIMS deposited film is low overall but the decrease rate is weak with increasing C_2H_2 flow rate. Based on this point, look again at the C content of the DC deposited films. It increases from 43.4 to 59.1 at.%, which spans two zones where the friction coefficient develops with different trend. Hence the friction coefficient of DC film decreases significantly from 10 to 20 sccm of C_2H_2. In addition, as can be seen from the development of the friction curve, lower C_2H_2 flow rate results in longer running-in period, as indicated by the friction curves of DC and HiPIMS films deposited at 10 sccm and 14 sccm of C_2H_2.

Comparing the frictional performance of DC and HiPIMS deposited films as a whole, it can be concluded that the friction coefficient of HiPIMS films outperforms that of DC films. The friction coefficient of the HiPIMS film deposited at 10 sccm C_2H_2 is even comparable to that of the DC film deposited at 18 sccm. This is provided by the higher content of amorphous carbon and sp^2-C content in the HiPIMS deposited films.

Fig. 4-8 displays the specific values of the wear rate for HfC/a-C:H films grown in DC and HiPIMS together with the values of friction coefficient. The wear rates of the DC films deposited at 10 and 12 sccm of C_2H_2 are not given since these two films were completely worn through after the tribological test. As the C_2H_2 flow rate increases, the wear rate gradually decreases in the range of $2.06 \times 10^{-5} \rightarrow 6.82 \times 10^{-6}\ \mathrm{mm^3/Nm}$ for DC deposited films, consistent with the development of the friction coefficient. For HiPIMS deposited films, it decreases first from $1.33 \times 10^{-5}\ \mathrm{mm^3/N}$ to $6.39 \times 10^{-6}\ \mathrm{mm^3/N}$ and then rises to $8.11 \times 10^{-6}\ \mathrm{mm^3/N}$. The lowest wear rate is obtained at 18 sccm C_2H_2. Note that for the HiPIMS deposited film, the trend of the wear rate is different from that of the friction coefficient. It can be inferred that the wear rate of the HiPIMS deposited films mainly depends on mechanical properties (i.e., physical factor) rather than tribochemical factor. To provide an in-depth discussion for the tribological properties of the film, SEM images of the wear tracks for the DC and HiPIMS deposited films are exhibited in Fig. 4-9.

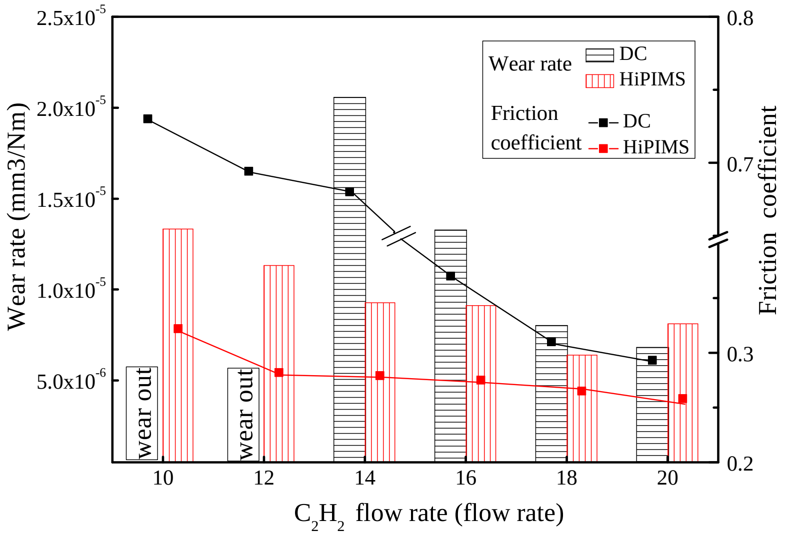

Figure 4-8. Friction coefficient (lines) and wear rate (columns) of HfC/a-C:H films deposited in DC and HiPIMS with different C_2H_2 flow rates.

From Fig. 4-9, it can be observed that with the increase of C_2H_2 from 10 to 20 sccm, the surface of the DC deposited film transitions from complete damage failure to a stable wear track, while for the HiPIMS deposited film, the wear track on the surface becomes narrower and shallower accompanied by fewer furrows. At 10 sccm C_2H_2, the wear track of the DC deposited film is completely damaged, showing significant delamination and cracks at the boundary of the wear track. There are no observed failures and cracks on the wear track of the HiPIMS deposited film at the same C_2H_2 flow rate. However, the distinct furrows parallel to the sliding direction are distributed over the wear track, revealed through the corresponding enlarged SEM image. The poor wear resistance in both DC and HiPIMS films deposited at low C_2H_2 flow rate is due to the severely inadequate hardness and toughness and less content of amorphous carbon.

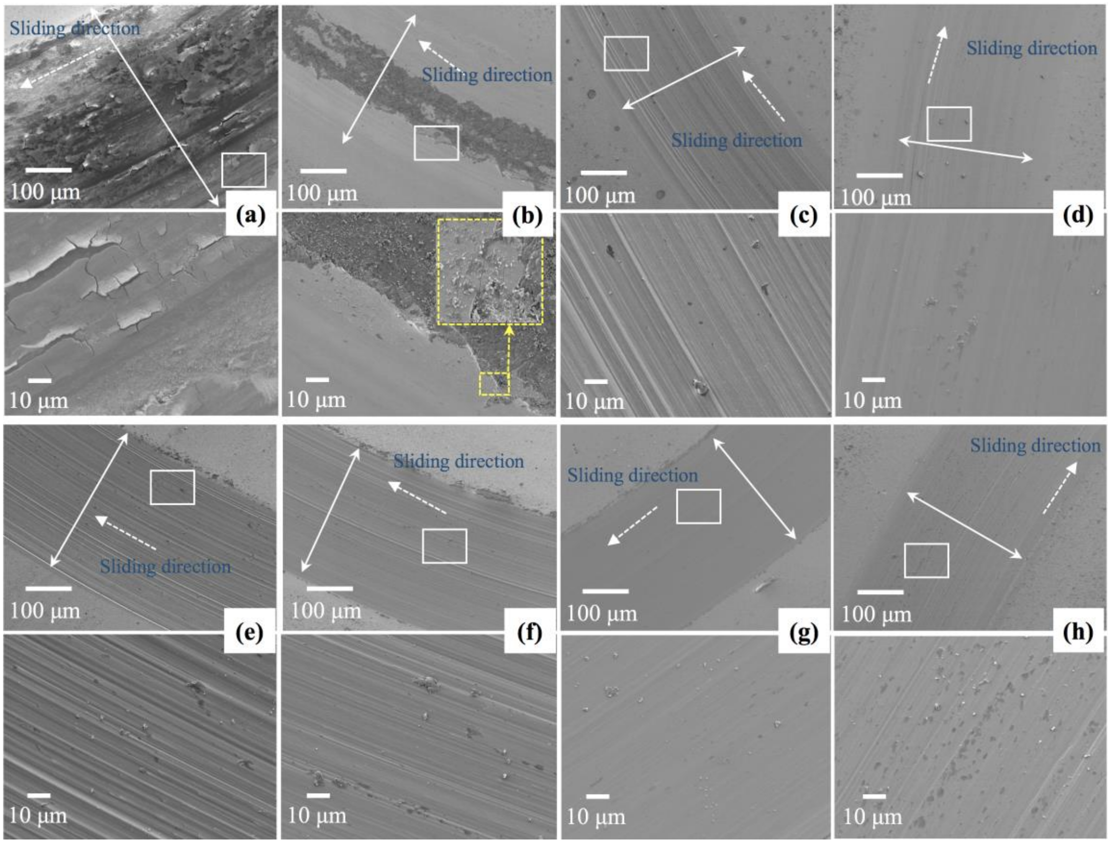

Figure 4-9. SEM images of wear tracks of HfC/a-C:H films deposited in DC (a-e) and HiPIMS (f-h) with different C_2H_2 flow rates: (a, e) 10 sccm, (b, f) 14 sccm, (c, g) 18 sccm, (d, h) 20 sccm.

As C_2H_2 flow rate increases to 14 sccm, the center area of the wear track of the DC deposited film is peeled off from M2 substrate. Meanwhile, through the enlarged picture in the yellow dotted region, it can be seen that there are several microcracks perpendicular to the sliding direction at the fracture edge, i.e., fish-scale-like cracks. It indicates severe shear deformation and breakage of the film during the sliding test. This relatively weak wear resistance is due to the combined effect of (i) lower hardness and toughness, (ii) lack of lubricated amorphous carbon and sp^2-C contents, and (iii) stick-slip adhesion wear mechanism. The low toughness of DC deposited film causes the large particles are detached during the running-in period. These particles would act as wear debris in the sliding contact area and are oxidized to form an adhesion layer on both film and ball surfaces. However, due to the strong shear force (caused by the less amorphous carbon content) that the counterpart ball imposes on the film and the poor hardness feature of the film, a stick-slip adhesion process would take place, damaging part of the film surface and triggering delamination. Subsequently, the lower toughness and looser inter-columnar structure of the film, which are not enough to resist the crack propagation along the less compact inter-column boundaries during multiple load cycles, give rise to the fish-scale-like cracks. For the HiPIMS deposited film at 14 sccm C_2H_2, the width of the wear track is slightly narrowed and the furrows distributed thereon are greatly reduced. It is attributed to the increased hardness. The formation of the furrow is caused by the wear of the abrasive particles formed from the breakage of the atomic bonds of the film or from the external environment. Since the increased hardness enhances the resistance of the film to plastic deformation, the formation of furrows is suppressed. Besides, the failure and partial delamination of DC films deposited at 10 and 14 sccm are another factors for their high values of friction coefficient (shown in Fig. 4-7).

When C_2H_2 flow rate reaches 18 sccm, the wear track of DC deposited film remains intact without any damage, accompanied by some noticeable furrows and a small amount of wear debris. The wear track of HiPIMS deposited film becomes very smooth, and the distributed furrows become shallower and hardly visible. These indicate a significant increase in wear resistance in both DC and HiPIMS deposited films. It is explained by the fact that at 18 sccm of C_2H_2, both DC and HiPIMS deposited films achieve the optimum mechanical properties and are accompanied by sufficient amorphous carbon and sp^2-C contents. They (i) lead to smaller sliding contact surface and shallower penetration distance (between the counterpart ball and the film under applied load), (ii) increase the film resistance against abrasion and inhibit the microcracks initiation and propagation, and (iii) facilitate the easy shearing of the two sliding surfaces. As C_2H_2 flow rate further increases to 20 sccm, the wear track appearing on the DC film is continuously optimized, the distributed furrows continue to be less and shallower. However, the width of the wear track on the HiPIMS film does not change significantly and the furrows which are almost invisible at 18 sccm become deeper again. Meanwhile, the dark-spotted areas distributed on the wear track begin to appear, which suggests the oxidation of the third body on the wear track. The deepened furrows correspond to the increase in the wear rate of the HiPIMS film deposited at 20 sccm C_2H_2 (shown in Fig. 4-8). Although here the compressive stress and the contents of amorphous carbon and sp^2-C in the film is high, which favors the termination of the crack propagation and the formation of the graphite-like tribolayer, the impaired hardness weakens the resistance of the film against plastic deformation under continual periodic load, thereby deepening the furrows and degrading the wear resistance. It indicates that the wear behavior of HiPIMS deposited film is dominated by mechanical properties.

Overall, in the cases where the C_2H_2 flow rate is less than 18 sccm, the wear behavior of DC and HiPIMS deposited films has the same trend and is continuously improved with the increase of C_2H_2 flow rate, which is supported by the simultaneous increase in both amorphous carbon, sp^2-C contents and mechanical properties. However, when C_2H_2 flow rate exceeds 18 sccm, the wear behavior of the DC film and the HiPIMS film is different. The wear behavior of DC film is controlled and optimized by tribochemical factors (i.e., amorphous carbon and sp^2-C contents), although hardness, toughness, and compressive stress develop toward the way degrading the wear resistance of the film. Conversely, the wear behavior of HiPIMS films is primarily dependent on mechanical properties. Although the evolutions of compressive stress, amorphous carbon content, and sp^2-C content tend to improve wear resistance, the degree of wear caused by the reduced hardness cannot be offset and compensated completely.

Looking back at the discussion of the ratios H/E^* and H^3/E^{*2} for characterizing mechanical behavior, it can be inferred that for HiPIMS deposited HfC/a-C:H films, the ratios H/E^* and H^3/E^{*2} can be used as suitable parameters to reflect and predict the friction and wear behaviors, which is consistent with the results in [26][27][28][29]. Besides, both the friction coefficient and wear rate of the HiPIMS deposited film are superior to those of the DC deposited film as a whole.

4.3.3 Thermal stability

The excellent properties of carbon-based nanocomposite film are mainly attributed to the nanocomposite structure consisting of hard crystalline grains dispersed in the amorphous carbon matrix. However, this nanostructure may be metastable [30]. Once the ambient temperature reaches or exceeds the threshold temperature, the film begins to transform into a conventional crystalline material due to grain growth. It thus results in the destruction of the nanocomposite structure, thereby destroying the excellent properties. However, high temperature conditions are unavoidable in industrial applications of the HfC/a-C:H films, especially in extreme environments. Therefore, it is necessary to clarify the thermal stability of the HfC/a-C:H film and whether the excellent mechanical properties can be maintained after high temperature annealing.

In this section, the thermal stability of the HfC/a-C:H film was investigated through (i) structural evolution (illustrated by XRD) and (ii) hardness evolution with the increasing annealing temperatures under the vacuum condition. The evolution of XRD for eight representative films deposited in DC and HiPIMS with different C_2H_2 flow rates of 10, 14, 18, and 20 sccm as a function of vacuum annealing temperature is shown in Fig. 4-10. All HfC/a-C:H films deposited in DC and HiPIMS exhibit a face-centered cubic HfC structure regardless of the annealing temperature. Moreover, both the intensity and position of the XRD peak change as the annealing temperature increases.

For the intensity evolution of the XRD peak, the DC deposited film is more sensitive to the annealing temperature than the HiPIMS deposited film. In the case of DC deposited film, the maximum growth in peak intensity is observed in the film deposited at 10 sccm C_2H_2, followed by the DC films deposited at 14, 18, and 20 sccm C_2H_2. At 10 and 14 sccm C_2H_2, the peak intensities of deposited films increase first from as-deposited state to annealing treatment at 500 °C, and then decrease after annealing at 600 °C. Here, it is also worth noting that the decrease in peak intensity is accompanied by a phase transition, which will be analyzed below. At 18 and 20 sccm C_2H_2, the XRD peaks of deposited films exhibit slight sharpening as the annealing temperature increases to 800 °C. In the case of HiPIMS deposited film, as the annealing temperature improves to 800 °C, the intensity of the XRD peak increases to a small extent and the peak shape become sharper slightly at 10 and 14 sccm C_2H_2. For the films deposited at 18 and 20 sccm C_2H_2, the intensity of the XRD peak remains almost unchanged.

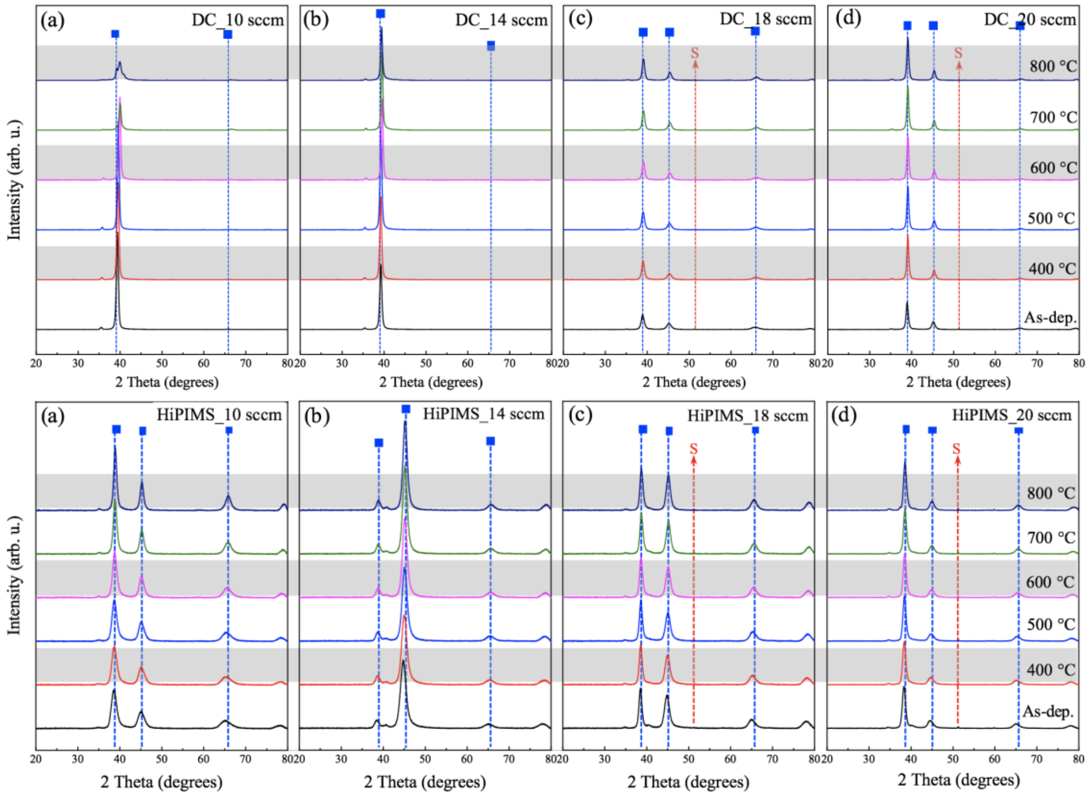

Figure 4-10. X-ray diffractograms of the HfC/aC:H films deposited in DC (a-d) and HiPIMS (e-h) after vacuum annealing treatments at different temperatures. Reference XRD peak positions for fcc-HfC (marked by the filled blue squares, Jcpds: 03-065-8751) and substrate M2 are indicated.

Since the intensity enhancement and sharpening of the XRD peak suggest the increase in crystallinity (i.e., grain growth), the intensity evolution of the XRD peak described above indicates that the phase of HiPIMS deposited film is more stable than that of DC deposited one. It is because the HiPIMS deposited film contains a higher amorphous carbon content, which more effectively encapsulates and hinders the recrystallization of HfC grains, thereby facilitating the stabilization of the HfC phase during the annealing treatment. Moreover, in both DC and HiPIMS conditions, the higher the flow rate of C_2H_2, the less visible the change in XRD peak intensity with increasing annealing temperature. That is, the stability of the HfC/a-C:H film becomes stronger as C content increases. It is also supported by the encapsulation and protection of the amorphous carbon matrix (on the HfC grains).

In order to clearly analyze the phase transition presenting in the DC films deposited at 10 and 14 sccm C_2H_2 after annealing treatments at 800 °C, the X-ray diffractogram of the DC film deposited at 10 sccm C_2H_2 is shown as a representative in Fig. 4-11. It can be observed that two new phases are formed and coexist with the original HfC phase (that appear in as-deposited film and marked by the orange triangles). The formation of the shoulder peak (located at $2\theta \approx 39.16°$) on the left side of (111) of the original HfC phase and the small peak at 66.36°, marked by the filled blue square, are assigned to the stoichiometric fcc HfC phase (Jcpds: 03-065-8751). The emerging hexagonal Hf peaks (Jcpds: 01-070-2820), the positions of which are shifted to the left as a whole, marked by the green circles, corresponding to the formation of the Hf(C) solid solution phase in the HfC/a-C:H film. These two newly formed phases are attributed to the segregation of HfC grains (actually it is substoichiometric, $HfC_{0.57,}$ calculated by XPS) into Hf atoms and higher stoichiometric HfC grains after annealing treatment. The segregated Hf atoms are subsequently crystallized and doped with free carbon, thus forming a Hf(C) solid solution phase. Simultaneously, the stoichiometric ratio of the remaining HfC grains becomes higher, reaching the stoichiometric ratio of 1. Therefore, the Hf(C) solid solution phase and the stoichiometric HfC phase are detected by XRD. A similar phase transition has been reported in the TiC/a-C:H coatings prepared by magnetron sputtering [31]. In their work, it was detected that the segregation of sub-stoichiometric TiC grains into Ti grains and more stoichiometric TiC grains occurred. Besides, it should be noted that under the deposition condition of DC with 10 and 14 sccm C_2H_2, the Hf atoms do not completely react with the C atoms during film grown, thereby causing partial Hf being present in the as-deposited film in the form of metallic state ultimately. They are susceptible to recrystallization under high temperatures and may interfere with the phase stability of the film. Therefore, in addition to the segregation of Hf atoms from the HfC grains, the metallic Hf presented at the boundary between the crystal phase and the amorphous phase may also participate in recrystallization, thereby also contributing to the observed obvious solid solution phase of Hf(C).

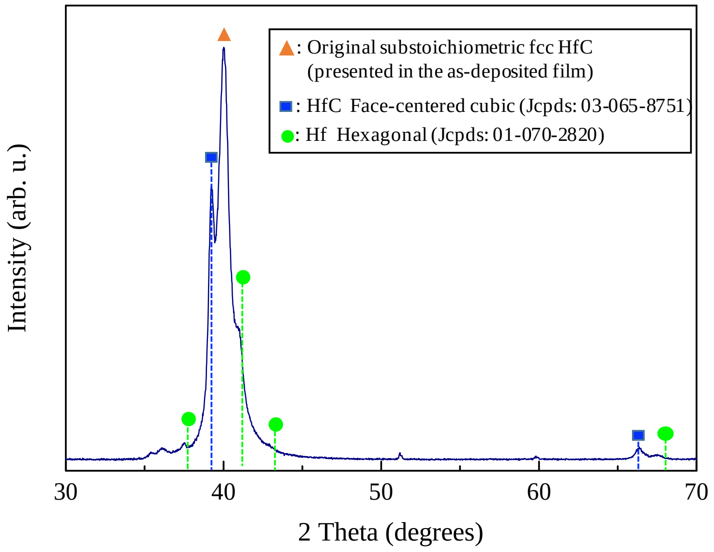

Figure 4-11. X-ray diffractogram of HfC/aC:H film deposited in DC with 10 sccm C_2H_2 after vacuum annealing treatment at 800 °C.

Throughout the XRD spectra of all tested films, this phase transition phenomenon is only detectable in the DC films deposited at 10 and 14 sccm C_2H_2. It is because at these deposition conditions, the lower ionization rate of the film-forming species and supply of insufficient C source results in lower content of amorphous carbon in the film. It is unstable for HfC phase due to the weaker protection effect of the less amorphous carbon matrix. Besides, the decrease in intensities of XRD peaks of the DC films deposited at 10 and 14 sccm after annealing treatment at 700 °C and 800 °C, respectively, is related to the phase transition. Recrystallization of original HfC grains after decomposition of the large-sized Hf atoms may cause a decrease in HfC grain size, and thus the XRD peak of HfC phase is broadened and reduced in intensity.

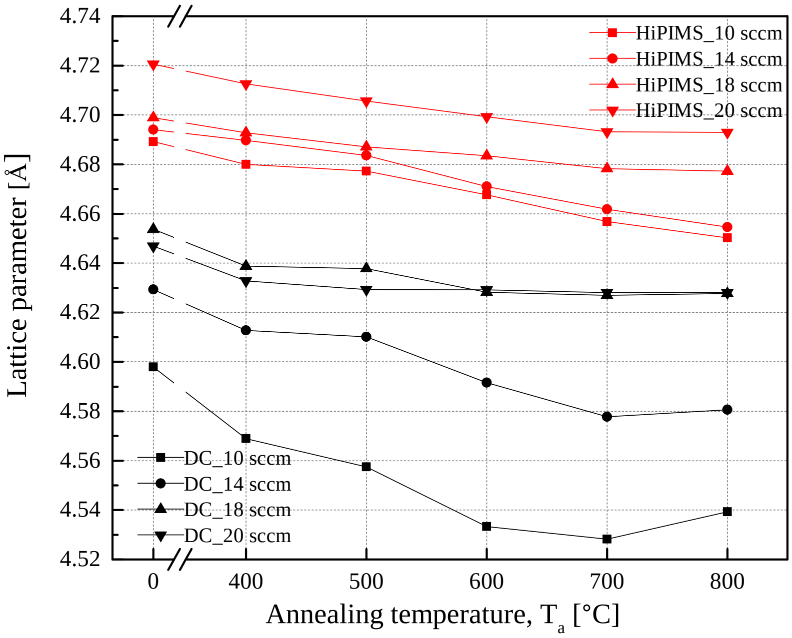

Figure 4-12. Evolution of the lattice parameter of the fcc HfC phase within HfC/a-C:H films prepared in DC and HiPIMS with different C_2H_2 flow rates, as a function of the vacuum annealing temperature T_a.

For the position evolution of the XRD peak, all the films, regardless of the deposition condition and C_2H_2 flow rate, shift toward the higher diffraction angle as the annealing temperature increases. The variation of the specific lattice parameter corresponding to the shift of the peak position is shown in Fig. 4-12. It is clear that for HiPIMS deposited films, the lattice parameter of each film shows a monotonically decreasing trend. Moreover, the rate of decrease in lattice parameter of the films deposited at low C_2H_2 flow rate (10 and 14 sccm) is faster than that of films deposited at high C_2H_2 flow rate (18 and 20 sccm), which is indicated by the negative slopes. However, the DC deposited films with different C_2H_2 flow rates have different evolutionary trends of lattice parameter as annealing temperature increases.

When we look at the evolution of the lattice parameter of the DC deposited film, the film deposited at low C_2H_2 flow rate increases again after high temperature annealing, whereas the film deposited at high C_2H_2 flow rate exhibits a monotonic decrease with increasing annealing temperature. In the cases of the DC films deposited at 10 and 14 sccm C_2H_2, the as-deposited films have significantly higher lattice parameters of 4.590 Å and 4.630 Å, compared to the annealed films to 700 °C where they are 4.528 Å and 4.578 Å, respectively. These lattice parameters then expand again to 4.539 Å and 4.581 Å after further annealing temperature upon 800 °C. In the cases of the DC films deposited at 18 and 20 sccm C_2H_2, their lattice parameters gradually decrease from 4.653 Å and 4.647 Å (at as-deposited state) to 4.628 Å and 4.628 Å (after annealing at 800 °C). The decrease rate of the lattice parameter becomes slower when the annealing temperature is greater than 600 °C. Moreover, the fact that the lattice parameter of the DC film deposited at 20 sccm is smaller than that of the film deposited at 18 sccm is attributed to the lower compressive stress of the film deposited at 20 sccm C_2H_2.

The decrease in lattice parameter with increasing annealing temperature corresponds to the release of compressive stress. During the annealing process, the film acquires energy to enhance the mobility and self-diffusion of atoms and clusters within it. The decrease in defect density and the increase in grain size thus occur in the film, resulting in the generation of tensile stress. Accordingly, the compressive stress is partially offset and the right-shift of the XRD peak is observed after the annealing treatment. The lattice parameter rises again as the annealing temperature further increases (occurs in the DC films deposited at 10 and 14 sccm C_2H_2) can be accounted for by the phase transition. It has been confirmed that the phase transition is a process in which a part of Hf atoms are segregated from HfC grains, and then a new stoichiometric HfC phase and a solid structure of Hf(C) phase are formed. For the HfC grains after segregation, the remaining result is an increased stoichiometric ratio. Consequently, the XRD peak shifts to the left and the lattice parameter increases.

The summary of nanohardness as a function of annealing temperature for HfC/a-C:H films deposited in DC and HiPIMS are presented in Fig. 4-13. It can be seen that all HfC/a-C:H films show remarkable hardness and no attenuation of hardness is observed when the annealing treatment reaches 800 °C, indicating the hardness of all HfC/a-C:H films performs well as the annealing temperature increases. In the case of DC deposited film, the hardness of the three films deposited at 10, 14 and 18 sccm C_2H_2

remain unchanged as the annealing temperature increases. The hardness of the film with the highest carbon content (deposited at 20 sccm C_2H_2) rises from 28.2 GPa to 34.6 GPa as the annealing temperature increases to 700 °C. In the case of HiPIMS deposited film, the hardness of the film having the lowest carbon content (deposited at 10 sccm C_2H_2) is not affected by the annealing treatment. The hardness of the films deposited at 14, 18 and 20 sccm C_2H_2 is enhanced with the annealing temperature. Moreover, the higher the C_2H_2 flow rate used for film deposition, the faster the rate of increase in hardness, suggested by the slope of the hardness evolution.

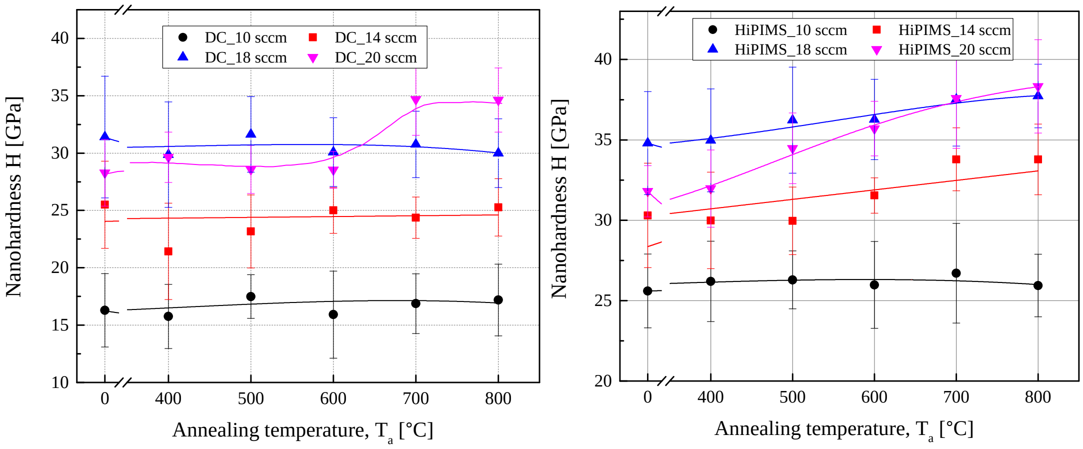

Figure 4-13. Nanohardness as a function of the vacuum annealing temperature for the HfC/a-C:H films deposited in DC (left) and HiPIMS (right) with different C_2H_2 flow rates.

From the above stability analysis of the phase of the HfC/a-C:H film (via XRD), it is known that as the annealing temperature rises, the residual compressive stress in the film is gradually annealed out. However, the influence of this variation does not have any negative effect on the film hardness. It means that compressive stress is not the main factor in hardness. For the nanocomposite film with excellent mechanical properties prepared by PVD technologies, the high hardness is typically observed to originate from the high compressive stress induced by energetic ion bombardment during the deposition, rather than being contributed solely by nanostructure, especially at low pressure conditions. For instance, Karvankova, P. *et al.* [32] reported that when

ZrN-Ni and CrN-Ni nanocomposite films were annealed at temperature above the deposition one, the compressive stress was released and the hardness was reduced. Therefore, the high hardness of the HfC/a-C:H film in our case that is not derived from compressive stress is desirable, which is able to expand the industrial applications of this film. Furthermore, the growth rate of the hardness of the film deposited under HiPIMS and high C_2H_2 flow rate conditions is more significant as the annealing temperature increases, which may be related to the higher carbon content of the film under these two conditions. It is known that the point defects and inter-column gaps within the as-deposited film formed during the rapid growth process can be considered as the hardness-degraded factor. However, the film can obtain energy under high temperature conditions, by which, the migration and diffusion of atoms or clusters therein are driven, and thus those hardness-degraded factors are filled and annihilated [33][34]. In our case of HfC/a-C:H films, during annealing, the migration and diffusion of carbon atoms inside the film is a more efficient way in filling the point defects and inter-column gaps due to its higher mobility compared to Hf atoms. Based on this view, the hardness-degraded factor in the film having a higher carbon content will be eliminated to a greater extent after the annealing treatment. Therefore, conditions that are more favorable for high carbon content cause the deposited film to hold a higher increase rate in hardness under high temperature environments.

By investigating the evolution of the microstructure and hardness of the film with increasing annealing temperature, it is determined that the HfC/a-C:H films prepared in DC and HiPIMS have strong thermal stability when the annealing temperature is as high as 800 °C. Moreover, both HiPIMS and high flow rate of C_2H_2 deposition conditions are advantageous for the prepared film to achieve a more stable phase composition and a higher hardness after annealing treatment.

4.3.4 Oxidation resistance

Oxidation tests were performed by annealing treatment in ambient air at different temperatures from 200 °C up to 600 °C with an incremental step of 100 °C. The oxidation degree of the film after annealing was measured by XRD, SEM, and energy dispersive X-ray spectroscopy (EDS). The phase composition of the film, tested by XRD after each annealing treatment, shows that when the annealing temperature <400 °C, none of the films deposited in both DC and HiPIMS conditions present any sign of oxidation. After annealing at 400 °C, a weaker anomalous peak at $2\theta \approx 34.67°$ appears on the diffraction spectra of DC films deposited at lower C_2H_2 flow (10, 12 and 14 sccm), while the diffraction spectra of HiPIMS films remain unchanged. After annealing at 500 °C, this anomalous peak appearing on the DC deposited films becomes more remarkable, while the diffraction spectra of the HiPIMS films are still stable and no other peaks can be detected. As the annealing temperature rises to 600 °C, distinct oxidation peaks appear on both DC and HiPIMS deposited films, indicating that the oxidation of the film begins to be active. To facilitate the comparison and analysis of the oxidation degree of the film, the diffraction spectra of DC and HiPIMS deposited films after annealing 500 °C and 600 °C are shown in Fig. 4-14.

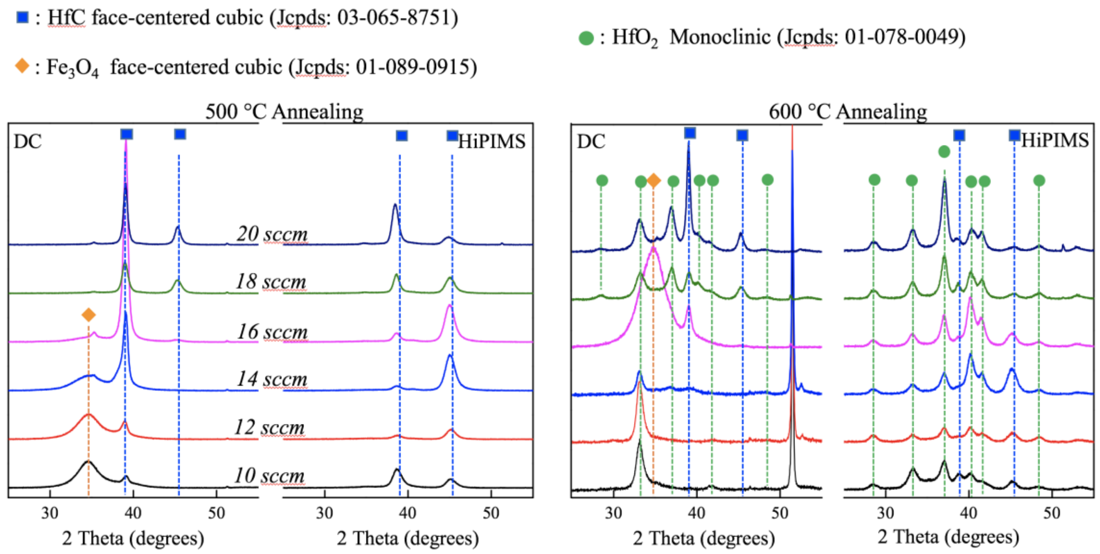

Figure 4-14. X-ray diffractograms of DC and HiPIMS deposited HfC/a-C:H films with different C_2H_2 flow rates after annealing treatment at 500 °C (left) and 600 °C (right).

After annealing at 500 °C, the anomalous peak at $2\theta \approx 34.67°$ is assigned to the (220) plane of the Fe_3O_4 phase, which appears in four DC films deposited from 10 to 16 sccm C_2H_2 and coexists with the HfC diffraction peaks. Moreover, the smaller the

C_2H_2 flow rate, the stronger the intensity of Fe_3O_4 phase. In the case of the DC films prepared at 18 and 20 sccm C_2H_2, no other diffraction peaks are detected except for the HfC phase. All the HiPIMS deposited films remain as-deposited state, no new phases related to oxides are detected, indicating higher stability compared to DC deposited films.

For the film in which the strong Fe_3O_4 diffraction peak appears, no signs of film peeling are detected. We infer that the Fe_3O_4 diffraction peak coexisting with HfC phase is caused by the diffusion of Fe atoms from the substrate into the film and their subsequent oxidation. According to the morphological analysis in Section 4.2.3, DC deposited films have relatively looser columnar crystal growth and larger inter-column gap compared to the HiPIMS deposited film. During the temperature rise period of the annealing process, Fe atoms will diffuse into the HfC/a-C:H film from M2 substrate through these loose inter-column gaps. Moreover, there may be more interconnected grain boundaries in the DC film deposited at low C_2H_2 flow rates (from 10 to 16 sccm) that are derived from larger grain sizes and less amorphous carbon content, which penetrate the entire film thickness and provide the passage for the external diffusion of Fe atoms. In the high temperature oxidizing environment, oxygen preferentially reacts with Fe, thus producing the observed Fe_3O_4 diffraction peaks. In addition, it should be noted that the oxidation peak of Fe_3O_4 is very wide, corresponding to extremely fine grain size. Since the Fe atoms forming the Fe_3O_4 phase are dispersed in the inter-column gap and the interconnected grain boundaries of the HfC film rather than being densely packed in a certain local region, the growing Fe_3O_4 grain is difficult to aggregate with adjacent species and coarsen. In addition, the degree of Fe atom diffusion that gradually decreases as C_2H_2 increases (reflected by the weaker intensity of the Fe_3O_4 peak) is due to the increasingly denser morphology and fewer interconnected grain boundaries.

After annealing at 600 °C, it can be observed that the oxidation resistance of DC deposited films increases with increasing C_2H_2 flow rate. The three DC films deposited at 10, 12 and 14 sccm C_2H_2 are completely detached from the substrate. Their XRD spectra exhibit a strong peak located at $2\theta \approx 52°$ and five weaker peaks of HfO_2, which are assigned to the substrate M2 and the oxidized product of the pure Hf interlayer (pre-deposited for better adhesion) after the HfC/a-C:H film peels off, respectively. The DC film deposited at 16 sccm C_2H_2 is intact and exhibits a spectrum where the Fe_3O_4, HfO_2 and HfC phases coexisted. These three coexisting phases represent the oxidized Fe atoms (that diffused from the substrate), the oxide layer of the HfC/a-C:H film surface, and the stable inner layer of HfC/a-C:H film, respectively. To determine this phase composition suggested by XRD spectrum, the EDS map of the cross-section of this film after 600 °C annealing treatment is given in Fig. 4-15. The cross-sectional EDS map of the same annealed film deposited in HiPIMS is also shown in this figure for comparison.

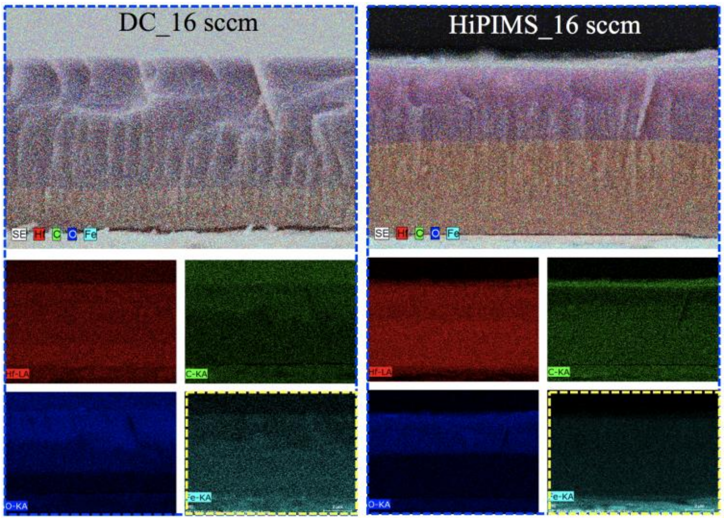

Figure 4-15. EDS map analysis of the cross-sections of the HfC/a-C:H films deposited at 16 sccm C_2H_2 in DC (left) and in HiPIMS (right) after annealing treatment at 600 °C.

By comparing the Fe element mapping spectrogram (marked by the yellow dotted box) in Fig. 4-15, the outward diffusion of Fe atoms in the DC deposited film is determined. In addition, it should be recognized that, in terms of peak shape and relative intensity with respect to HfC, the Fe_3O_4 peak appearing here (XRD of 600 °C annealed DC film at 16 sccm) is very similar to those occurring on the DC films (at low C_2H_2 flow rates) after 500 °C annealing treatment. It also indirectly confirms our previous inference that the Fe_3O_4 peak after 500 °C annealing is also caused by the outward diffusion of Fe atoms. For DC films deposited at 18 and 20 sccm C_2H_2, the coexistence of HfC and HfO_2 phases clearly appears, and no any phase associated with Fe_3O_4 is detected. It indicates that the more compact morphology of the film at high C_2H_2 flow rate effectively blocks the diffusion of Fe atoms. At the same time, the HfC peak of the film deposited at 20 sccm has a stronger relative intensity, indicating the better oxidation resistance than that of the film deposited at 18 sccm. Regardless of the C_2H_2 flow rate, all the film prepared under HiPIMS begins to oxidize, exhibiting stronger (in intensity) oxidation peaks HfO_2 coexisting with the weakened HfC peaks. Taking the XRD spectra of as-deposited HiPIMS films as the benchmark, the intensity of the HfC diffraction peak is compared. It can be seen that the intensities of the HfC peaks are comparable to those of HfO_2 peaks at low C_2H_2 flow rates from 10 to 14 sccm, while at high C_2H_2 flow rates from 16 to 20 sccm, the HfC peaks tend to be indistinguishable and its intensities are much weaker than those of HfO_2 peaks. Therefore, it can be roughly judged that the oxidation resistance of the HiPIMS deposited films decreases as the C_2H_2 flow rate increases. Moreover, compared to the performance of the DC deposited films in high temperature oxidizing environment, the HiPIMS deposited films are not adversely affected by atomic diffusion from the substrate. It is attributed to the denser morphology and fewer interconnected grain boundaries of the HiPIMS films. In order to more accurately investigate the oxidation situation of HfC/a-C:H films under different C_2H_2 flow rates and different deposition conditions, the cross-sectional morphologies of the films after oxidation at 600 °C are scanned by SEM and EDS.

Figure 4-16 shows the SEM and EDS scanning maps of the cross-sections for the representative HfC/a-C:H films which are DC films and HiPIMS films deposited at 14, 16, 18 and 20 sccm, respectively. It can be observed that the oxidation resistance of the DC deposited films gradually increases with the increase of C_2H_2 flow rate, and the optimal oxidation resistance is obtained at 20 sccm C_2H_2. For the DC film deposited at 14 sccm, only top view and EDS spectrum analysis are given since the film is completely delaminated from the substrate after annealed at 600 °C. Through the concentration of elements Hf, O, C and Fe in the EDS spectrum, it can be inferred that the surface we observed is the oxidation product of the pure Hf interlayer remaining after HfC/a-C:H film complete oxidation stripping. It is consistent with the XRD spectrum of the DC film deposited at 14 sccm C_2H_2 (which exhibits a rather weak peak of HfO_2 and a very strong substrate peak of M2). The reasons for film peeling are (i) the mismatch of the thermal expansion coefficients between the film and the substrate and (ii) the insufficient residual compressive stress. During the temperature rise stage of the annealing treatment, tensile stress is induced in the film. However, for the film deposited with low C_2H_2 flow rate, the residual compressive stress is insufficient to counteract this tensile stress, and the competition result is that the tensile stress cracking appears on the oxide film and thus exhibits a high-density network-like penetrating crack. The tensile cracks spreading over the surface of the sample is too large to be sealed effectively at the oxidation temperature and created free paths for oxygen penetration, which cause the rapid oxidation and flaking of the film. For the DC films deposited at 18 and 20 sccm, 54% and 29% of the films are oxidized, respectively, indicated by the thickness of layer 1 in EDS map.

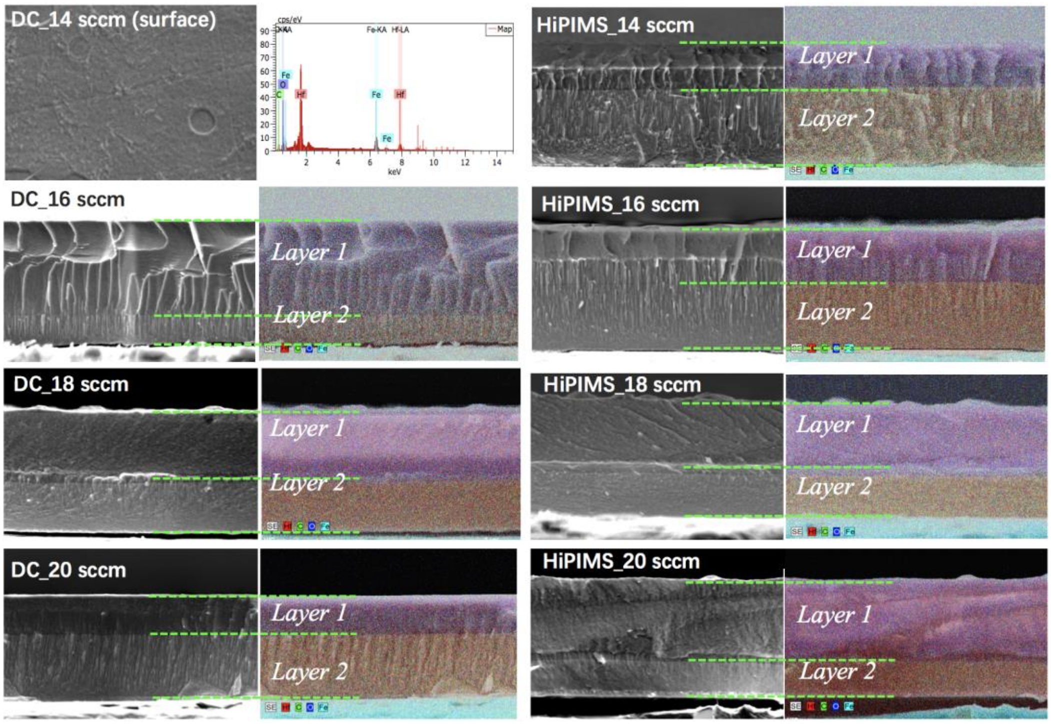

Figure 4-16. The cross-section SEM images and corresponding EDS maps of HfC/a-C:H films after annealing at 600 °C deposited in DC (left column) and HiPIMS (right column).

Contrary to the DC deposited film, the oxidation resistance of the HiPIMS deposited film continues to decrease as the C_2H_2 increases. For the HiPIMS film deposited at 14 sccm C_2H_2, the oxide layer accounts for 26% of the film thickness. As C_2H_2 increases to 18 and 20 sccm, the thickness of the oxide layer increases to 55% and 69% of the entire film thickness, respectively.

Overall comparison of the oxidation resistance of DC and HiPIMS deposited films, it can be stated that for the low carbon content HfC/a-C:H films (deposited at 10 to 16 sccm C_2H_2), the HiPIMS deposited films exhibit better oxidation resistance. For the middle carbon content films (deposited at 18 sccm), the oxidation resistance is independent of the deposition condition. Whereas for the high carbon content films (deposited at 20 sccm C_2H_2), the DC condition favors stronger oxidation resistance. Such variable oxidation resistance of the film is because it is simultaneously influenced by multiple factors rather than monotonous control via a certain factor. It is governed by three factors: the morphology of the film, the size of the HfC grains, and the content of amorphous carbon matrix.

For the low carbon content HfC/a-C:H films deposited at 10 to 16 sccm, the oxidation resistance is dominated by the film morphology (i.e., the inter-column gaps) and the grain size. On the one hand, the loose inter-column gap of the DC film fails to block the diffusion of Fe and O elements from the substrate and from the environment under the high temperature oxidation atmosphere. The subsequent rapid reaction between them is catastrophic to the stability and oxidation resistance of the HfC/a-C:H film. On the other hand, for the carbon-based nanocomposite film, the main antioxidant mechanism is accessed by growing the outermost barrier layer (acts as an efficient layer against the diffusion of oxygen) via fast oxidation of crystalline grain. Accordingly, the film underneath is not at risk of suffering from continuous intrusion by oxygen. However, the larger grain size of the DC film cannot be rapidly oxidized, thus the formation of the barrier layer is slower than that of the HiPIMS film, thereby leading to a thicker oxide layer on the DC films. Consequently, the synergy of the poor anti-diffusion ability of the film morphology and the slower formation rate of the barrier layer results in a weaker oxidation resistance for the DC film deposited at low C_2H_2 flow rates.

For the middle carbon content HfC/a-C:H films deposited at 18 sccm C_2H_2, the very close oxidation resistance under different deposition conditions is caused by the competition between the amorphous carbon content and the grain size. Although the amorphous carbon phase plays a decisive role in promoting mechanical properties and tribological performance, it is a drawback in terms of oxidation resistance (especially sp^2-C, which is quite unstable at temperatures exceeding 400 °C [35]). In the early stage of the oxidation process (before the barrier layer is formed), the carbon on the surface of the HfC/a-C:H film is oxidized and then escapes from the film surface. The vacancies left behind would be used as the channel for oxygen to diffuse into the interior of the film, and the strategy of reducing the channel diameter and eventually sealing the channels is the rapid oxidative growth, aggregation and interconnection of the grains. At the deposition condition of 18 sccm C_2H_2, compared to DC films, the HiPIMS film has a smaller grain size. It thus results in a faster oxidation of the grains (i.e., rapid growth of the barrier layer), which is advantageous for achieving a stronger antioxidant capacity. However, the HiPIMS film also contains more amorphous carbon than the DC film, especially the unstable sp^2-C content (indicated via Table 4-1). When the amorphous carbon matrix is first oxidized, the vacancies left and the radius of the formed channels may be larger than those in DC film. Thus the higher content of amorphous carbon in the HiPIMS film provides a larger passage for oxygen, playing a role in deteriorating the oxidation resistance. The synergy of these two completely opposite factors ultimately engenders almost the same antioxidant capacity on the HiPIMS and DC films deposited at 18 sccm C_2H_2.

For the high carbon content HfC/a-C:H films deposited at 20 sccm C_2H_2, the oxidation resistance of the DC deposited film is significantly stronger than that of the HiPIMS deposited film. It is primarily determined by the scale of the mean grain separation (filled by the amorphous carbon). Compared to the films deposited at 18 sccm C_2H_2, the grain size of the DC film is increased obviously, but the content of amorphous carbon therein is only slightly augmented. The grain size of the HiPIMS film is reduced, accompanied by a large increase in amorphous carbon content. Accordingly, at the deposition condition of 20 sccm C_2H_2, the mean grain separation filled by amorphous carbon is narrowed in the DC deposited films, but is greatly broadened in the HiPIMS film. Since oxygen diffusion channels are more easily initiated by the oxidation of amorphous carbon filled in the grain space, the oxidation resistance of the HiPIMS film is degraded to a greater extent than that of the DC film. Therefore, the balance result of the competition maintained at 18 sccm C_2H_2 is broken, and the oxidation resistance of the DC film becomes stronger.

4.4 Conclusion

Nanocomposite HfC/a-C:H films were deposited utilizing DC magnetron sputtering and HiPIMS operated at floating substrate in the acetylene containing atmosphere. As a function of carbon content and deposition conditions, the chemical bonding state, structure, morphology, residual stress, mechanical and tribological properties, and thermal stability, as well as oxidation resistance of the HfC/a-C:H films were systematically investigated.

The results reveal that the mechanical properties, friction behavior, and thermal stability of the HfC/a-C:H film show the same development trend under both DC and HiPIMS deposition conditions as the carbon content increases. As the carbon content increases, the hardness of the HfC/a-C:H film exhibit the typical behavior of nc-MeC/a-C:H films. It first increases with increasing carbon content and then reaches the maximum value under the appropriate mean grain separation constructed by the HfC grains and amorphous carbon matrix. Outside this mean grain separation scale, the hardness begins to drop. Beside, the effect of the stoichiometric ratio of the HfC grain on the film hardness is emphasized. The friction coefficient of the film decreases monotonously as the carbon content increases, attributed to the increasing content of amorphous carbon matrix. The thermal stability of the film is gradually enhanced with increasing carbon content when the vacuum annealing temperature reaches 800 °C. It is provided by stronger encapsulation and inhibition effects of more amorphous carbon on the grain growth as the carbon content increases. Moreover, the higher the carbon content of the film, the more potential it is to be further hardened at high temperatures, since the micro-pores and inter-column gaps in the film can be more completely filled and eliminated by C atoms (with faster migration and self-diffusion rates). It is worth noting that for these three properties, although the development trend of the HfC/a-C:H film is consistent under both DC and HiPIMS conditions, the HiPIMS deposited films perform better than the DC ones. The plasma characteristics of the HiPIMS discharge are responsible for the higher hardness and effective Young's modulus, lower friction coefficient and stronger thermal stability of the HiPIMS deposited films.

Different from the evolutions of mechanical properties, friction behavior and thermal stability, as the carbon content increases, the evolution of wear rates is slightly different in DC and HiPIMS deposited films, while the oxidation resistance displays a completely opposite development trend in DC and in HiPIMS. It is shown that with increasing carbon content, the wear rate monotonically decreases for the DC deposited films, but first decreases and then rises for the HiPIMS deposited films. This indicates that the wear rate of the DC film is controlled by tribochemical factor, while the HiPIMS film is dominated by mechanical features. Furthermore, the lower wear rate is achieved on the HiPIMS deposited films due to their higher hardness and more amorphous carbon content providing stronger resistance to plastic deformation and easier shearing. With the increase of carbon content, the oxidation resistance of DC deposited films is gradually optimized, while the oxidation resistance of HiPIMS deposited films is gradually deteriorated. It is determined by the synergistic effect of the morphology of the film, the size of the HfC grains, and the content of amorphous carbon matrix. Moreover, HiPIMS condition facilitates the film to hold stronger oxidation resistance in the case of low carbon content films. In the case of high carbon content films, DC conditions are conducive to stronger oxidation resistance.

4.5 References

[1] L.E. Toth, Transition Metal Carbides and Nitrides (Academic Press, New York, 1971).

[2] Holleck, H. (1986). Material selection for hard coatings. Journal of Vacuum Science & Technology A: Vacuum, Surfaces, and Films, 4(6), 2661-2669.

[3] Jhi, S. H., Ihm, J., Louie, S. G., & Cohen, M. L. (1999). Electronic mechanism of hardness enhancement in transition-metal carbonitrides. Nature, 399(6732), 132.

[4] Jhi, S. H., & Ihm, J. (1997). Electronic structure and structural stability of TiCxN1−x alloys. Physical Review B, 56(21), 13826.

[5] Li, G., & Li, G. (2010). Microstructure and mechanical properties of hafnium carbide coatings synthesized by reactive magnetron sputtering. Journal of Coatings Technology and Research, 7(3), 403-407.

[6] Wang, Y. L., Xiong, X., Li, G. D., Zhang, H. B., Chen, Z. K., Sun, W., & Zhao, X. J. (2012). Microstructure and ablation behavior of hafnium carbide coating for carbon/carbon composites. Surface and Coatings Technology, 206(11-12), 2825-2832.

[7] Yoo, H. I., Kim, H. S., Hong, B. G., Sihn, I. C., Lim, K. H., Lim, B. J., & Moon, S. Y. (2016). Hafnium carbide protective layer coatings on carbon/carbon composites deposited with a vacuum plasma spray coating method. Journal of the European Ceramic Society, 36(7), 1581-1587.

[8] Shuo, W., Kan, Z., Tao, A., Chaoquan, H., Qingnan, M., Yuanzhi, M., ... & Weitao, Z. (2015). Structure, mechanical and tribological properties of HfCx films deposited by reactive magnetron sputtering. Applied Surface Science, 327, 68-76.

[9] Jiang, K. M., Zhao, D. Q., Jiang, X., Huang, Q., Miao, L. J., Lu, H. M., & Li, Y. (2018). Electronic-structure, corrosion and mechanical properties of nc-CrC/aC: H films deposited by multi-arc ion plating. Journal of Alloys and Compounds, 750, 560-569.

[10] Meng, Q. N., Wen, M., Mao, F., Nedfors, N., Jansson, U., & Zheng, W. T. (2013). Deposition and characterization of reactive magnetron sputtered zirconium carbide films. Surface and Coatings Technology, 232, 876-883.

[11] Lewin, E., Wilhelmsson, O., & Jansson, U. (2006). Nanocomposite nc-TiC/a-C thin films for electrical contact applications. Journal of applied Physics, 100(5), 054303.

[12] Berg, S., & Nyberg, T. (2005). Fundamental understanding and modeling of reactive sputtering processes. Thin solid films, 476(2), 215-230.

[13] Wallin, E., & Helmersson, U. (2008). Hysteresis-free reactive high power impulse magnetron sputtering. Thin Solid Films, 516(18), 6398-6401.

[14] Kubart, T., Aiempanakit, M., Andersson, J., Nyberg, T., Berg, S., & Helmersson, U. (2011). Studies of hysteresis effect in reactive HiPIMS deposition of oxides. Surface and Coatings Technology, 205, S303-S306.

[15] Depla, D., & Gryse, R. D. (2002). Cross section for removing chemisorbed oxygen from an aluminum target by sputtering. Journal of Vacuum Science & Technology A: Vacuum, Surfaces, and Films, 20(2), 521-525.

[16] Sarakinos, K., Alami, J., Klever, C., & Wuttig, M. (2008). Process stabilization and enhancement of deposition rate during reactive high power pulsed magnetron sputtering of zirconium oxide. Surface and Coatings Technology, 202(20), 5033-5035.

[17] Aiempanakit, M., Helmersson, U., Aijaz, A., Larsson, P., Magnusson, R., Jensen, J., & Kubart, T. (2011). Effect of peak power in reactive high power impulse magnetron sputtering of titanium dioxide. Surface and Coatings Technology, 205(20), 4828-4831.

[18] Samuelsson, M., Sarakinos, K., Högberg, H., Lewin, E., Jansson, U., Wälivaara, B., ... & Helmersson, U. (2012). Growth of Ti-C nanocomposite films by reactive high power impulse magnetron sputtering under industrial conditions. Surface and Coatings Technology, 206(8-9), 2396-2402.

[19] Pei, Y. T., Galvan, D., & De Hosson, J. T. M. (2005). Nanostructure and properties of TiC/aC: H composite coatings. Acta materialia, 53(17), 4505-4521.

[20] Zhang, R. F., Argon, A. S., & Veprek, S. (2010). Understanding why the thinnest SiNx interface in transition-metal nitrides is stronger than the ideal bulk crystal. Physical Review B, 81(24), 245418.

[21] Zhang, R. F., Argon, A. S., & Veprek, S. (2009). Electronic structure, stability, and mechanism of the decohesion and shear of interfaces in superhard nanocomposites and heterostructures. Physical Review B, 79(24), 245426.

[22] Parreira, N. M. G., Carvalho, N. J. M., Vaz, F., & Cavaleiro, A. (2006). Mechanical evaluation of unbiased W–O–N coatings deposited by dc reactive magnetron sputtering. Surface and Coatings Technology, 200(22-23), 6511-6516.

[23] Martínez-Martínez, D., López-Cartes, C., Fernández, A., & Sánchez-López, J. C. (2009). Influence of the microstructure on the mechanical and tribological behavior of TiC/a-C nanocomposite coatings. Thin Solid Films, 517(5), 1662-1671.

[24] Jansson, U., Lewin, E. (2013). Sputter deposition of transition-metal carbide films—A critical review from a chemical perspective. Thin Solid Films, 536, 1-24.

[25] Zehnder, T., & Patscheider, J. (2000). Nanocomposite TiC/a–C: H hard coatings deposited by reactive PVD. Surface and Coatings Technology, 133, 138-144.

[26] Musil, J., Louda, M., Soukup, Z., & Kubásek, M. (2008). Relationship between mechanical properties and coefficient of friction of sputtered aC/Cu composite thin films. Diamond and Related Materials, 17(11), 1905-1911.

[27] Leyland, A., & Matthews, A. (2000). On the significance of the H/E ratio in wear control: a nanocomposite coating approach to optimised tribological behaviour. Wear, 246(1-2), 1-11.

[28] Leyland, A., & Matthews, A. (2004). Design criteria for wear-resistant nanostructured and glassy-metal coatings. Surface and Coatings Technology, 177, 317-324.

[29] Musil, J., Novák, P., Čerstvý, R., & Soukup, Z. (2010). Tribological and mechanical properties of nanocrystalline-TiC/a-C nanocomposite thin films. Journal of Vacuum Science & Technology A: Vacuum, Surfaces, and Films, 28(2), 244-249.

[30] Musil, J. (2000). Hard and superhard nanocomposite coatings. Surface and coatings technology, 125(1-3), 322-330.

[31] Zábranský, L., Buršíková, V., Daniel, J., Souček, P., Vašina, P., Dugáček, J., ... & Peřina, V. (2015). Comparative analysis of thermal stability of two different nc-TiC/aC: H coatings. Surface and Coatings Technology, 267, 32-39.

[32] Karvankova, P., Männling, H. D., Eggs, C. H., & Veprek, S. (2001). Thermal stability of ZrN–Ni and CrN–Ni superhard nanocomposite coatings. Surface and Coatings Technology, 146, 280-285.

[33] Asher, T., Inberg, A., Glickman, E., Fishelson, N., & Shacham-Diamand, Y. (2009). Formation and characterization of low resistivity sub-100 nm copper films deposited by electroless on SAM. Electrochimica Acta, 54(25), 6053-6057.

[34] Brückner, W., Thomas, J., & Schneider, C. M. (2001). Evolution of stress and microstructure in NiFe (20 wt.%) thin films during annealing. Thin Solid Films, 385(1-2), 225-229.

[35] Osswald, S., Yushin, G., Mochalin, V., Kucheyev, S. O., Gogotsi, Y. (2006). Control of sp2/sp3 carbon ratio and surface chemistry of nanodiamond powders by selective oxidation in air. Journal of the American Chemical Society, 128(35), 11635-11642.

Conclusions and perspectives

The primary purpose of this thesis was to study the HiPIMS technology from (i) its plasma discharge mechanism to (ii) its superiority in structural modulation and performance optimization of two transition metal carbon-based nanocomposite films, namely TaC/a-C:H and HfC/a-C:H films.

On this basis, the thesis was organized into the following two main parts. In the first part, the dispersion relationship describing the plasma located in the ionization region during the HiPIMS discharge was analyzed, and then a coupling-induced wave model that can explain the driving mechanism of the spoke phenomenon was proposed. Moreover, the validity and accuracy of the proposed model were verified by comparison with published experimental data on the spokes during HiPIMS plasma discharge. In the second part, two nanocomposite TaC/a-C:H and HfC/a-C:H films were deposited by HiPIMS on several different substrates, and their relevant characteristics were carried out in detail. These two films were also deposited under DC condition as a reference comparison to reveal the effect of HiPIMS plasma on the growth of nanocomposite films. Furthermore, the correlations between the chemical bonding state and structure of TaC/a-C:H and HfC/a-C:H films and their mechanical properties, tribological behavior, thermal stability, and oxidation resistance were analyzed and discussed.

The results of the first part in terms of the spoke mechanism were devoted to the derivation and analysis of the dispersion relationship and its dynamic evolution characteristics. It revealed that during HiPIMS discharge, the coupling of Doppler-shifted electron Bernstein (DSEB) wave and ion sound (IS) wave induced a long-scale electric field (cm-size) oscillation waving at the frequencies difference, which was defined as the difference frequency (DF) wave, and a high-frequency short-scale electric field oscillation which was defined as the sum frequency (SF) wave. Based on the views, the coupling-induced wave model for the origin of the spoke was proposed. The collective behavior of ion rearrangement guided by the DF wave along azimuthal direction was the observed spoke. The spoke location was defined by the phase change position of the DF wave, and its typical size was related to the wavelength. Besides, we give a new insight into the driving mechanism of the ECD instability. The collective behavior of electron rearrangement guided by the SF wave was considered as the ECD instability. The characteristics of the spoke and ECD instability reproduced by the coupling-induced wave model, including frequency, velocity, wavelength, as well as the dynamic process and internal electric field distribution of the spoke, were strikingly similar to those reported in the literature. Moreover, the evolutions of spoke rotating velocity and mode number were considered and predicted by the proposed model, which were consistent with those reported by the experimental measurements from the literature.

In the results of the second part, the thesis focused on the nanocomposite TaC/a-C:H and HfC/a-C:H films deposited by HiPIMS technology. Comparing with the TaC/a-C:H and HfC/a-C:H films deposited in DC condition, it demonstrated that the HiPIMS deposited films have higher hardness and effective Young's modulus, higher toughness, lower friction coefficient and wear rate. This was attributed to the higher volume fraction of amorphous carbon matrix, finer grains, higher stoichiometric ratio of metal carbide grains, and greater compressive stress in the HiPIMS deposited films. These features responsible for better performance were supported by the greater degree of plasma reaction between target particles and C_2H_2 induced by the high energy density and high ionization rate of the HiPIMS discharge.

For the oxidation resistance, TaC/a-C:H and HfC/a-C:H films showed completely different condition dependencies. The TaC/a-C:H films deposited in HiPIMS presented stronger oxidation resistance than that deposited in DC, while for the HfC/a-C:H films, the oxidation resistance was determined synergistically by both the deposition conditions (DC and HiPIMS) and the carbon content in the films. It revealed that HiPIMS condition facilitated the HfC/a-C:H film to hold stronger oxidation resistance in the case of low carbon content films since HiPIMS plasma is more conducive to the growth of the nanostructure required for strong oxidation resistance, that is, smaller grains and dense morphology. In the case of high carbon content HfC/a-C:H films, DC condition was beneficial to the oxidation resistance of the film, derived from the narrower mean grain separation provided by the low energy density of DC plasma at comparable grain sizes. Meanwhile, the essential mechanism controlling the oxidation resistance of the carbon-based nanocomposite film was analyzed and emphasized, namely, the results of the synergistic effects of the morphology of the film, the size of HfC grains, and the content of the amorphous carbon matrix.

Thermal stability was only tested in the case of HfC/a-C:H films, the results indicated that HiPIMS condition provided a better strategy for growing carbon based nanocomposite film with stronger thermal stability, contributed by the stronger encapsulation and inhibition effects on grain growth by more amorphous carbon caused by the higher reactivity of the HiPIMS plasma. Moreover, the HiPIMS deposited film has greater potential for further hardening after high-temperature vacuum annealing, which was attributed to the fact that the point defects (vacancies) and inter-column gaps generated during the film preparation can be more completely filled and eliminated by more C atoms (with faster migration and self-diffusion rates).

Based on the results of the first part in this thesis, it is expected that more research will be devoted to HiPIMS plasma mechanism, which may be a key factor in solving some of the challenges currently faced by HiPIMS, and thus may become one of the cornerstones for rapidly pushing HiPIMS technology to industrial applications. Conclusions of the second part, in Chapters 3 and 4, identified that HiPIMS technology can provide a potential strategy for preparing higher performance TaC/a-C:H and HfC/a-C:H films in terms of hardness, wear resistance, oxidation resistance, and thermal stability by modulating the chemical bonding state and nanocomposite structure of the films through reactive plasma. It is very practical and can be transferred to other carbon-based nanocomposite films broader than that tested within this thesis.

Encouraged by the proven benefits of HiPIMS technology with respect to mechanical properties, tribological properties, oxidation resistance, and thermal stability of the film prepared, also in conjunction with the sensitivity of the HiPIMS plasma to the magnetic field, our future work will focus on further optimizing the performance of nanocomposite TaC- or HfC-based films by applying auxiliary magnetic field configuration in HiPIMS. It is known that HiPIMS plasma has a high ionization rate, which allows the magnetic field to be an effective “control button” on the dynamic characteristics of the plasma, thereby flexibly controlling film growth and tailoring film properties to meet specific needs. By designing a proper magnetic field configuration as the supplementary means for manufacturing TaC- or HfC-based films, it is expected that the above properties of the films can be further improved. Furthermore, the application of the auxiliary magnetic field provides more multidimensional control over film growth, which may provide finer modulation on film nanocomposite structure and stoichiometry, thereby allowing a more delicate investigation for film properties.

Titre : Etude du phénomène plasma dans les décharges HiPIMS. Application au dépôt réactif de revêtements nanocomposites en carbure de tantale et de hafnium et caractérisation de leurs propriétés physicochimiques, structurales, mécaniques et de résistance à l'oxydation.

Mots clés : Plasma HiPIMS, films TaC/a-C:H et HfC/a-C:H, propriétés mécaniques, performances tribologiques, stabilité thermique, résistance à l'oxydation.

Résumé : La technologie de pulvérisation magnétron par impulsions de haute puissance (HiPIMS) a été développée et est considérée comme une méthode efficace pour la préparation des films. La technologie HiPIMS permet une bien plus grande flexibilité pour ajuster la structure et les performances du film, conduisant à des films avec des propriétés uniques qui sont souvent irréalisables dans les autres approches PVD. Cependant, le mécanisme sous-jacent du plasma pour soutenir la croissance du film impliqué est actuellement flou. De plus, la technologie HiPIMS est limitée au laboratoire, de nombreux films aux propriétés souhaitables n'ont pas été explorés dans le cadre de la pulvérisation HiPIMS. Dans ce travail, (i) l'origine de la structure cohérente du plasma haute densité (les « spokes ») dans la décharge HiPIMS et (ii) comment la structure et les propriétés des films de TaC/a-C:H et HfC/a-C:H sont gérées par HiPIMS ont été étudiés. Dans l'étude du mécanisme de formation des « spokes », basée sur la relation de dispersion du plasma HiPIMS et l'évolution du couplage entre deux ondes azimutales, un modèle d'onde induit par couplage a été proposé. Dans l'étude des films TaC/a-C:H et HfC/a-C:H, les états des liaisons chimiques, la structure, la morphologie, les propriétés mécaniques et tribologiques, la stabilité thermique ainsi que la résistance à l'oxydation des films ont été étudiés. En comparaison avec ces films déposés par pulvérisation magnétron DC, il est démontré que la technologie HiPIMS permet une stratégie potentielle pour préparer des films TaC/a-C:H et HfC/a-C:H plus performants en termes de dureté, de coefficient de frottement et de résistance à l'usure, de résistance à l'oxydation et de stabilité thermique en modulant l'état de liaison chimique et la structure nanocomposite des films à travers un plasma réactif.

Title : Study of the plasma phenomenon in HiPIMS discharge. Application to the reactive deposition of tantalum and hafnium carbide nanocomposite films and characterization of their physicochemical, structural, mechanical and oxidation resistance properties.

Keywords : HiPIMS plasma, TaC/a-C:H and HfC/a-C:H films, mechanical properties, tribological performance, thermal stability, oxidation resistance.

Abstract : High Power Impulse Magnetron Sputtering technology (HiPIMS) has been developed and considered as an effective method for film preparation. HiPIMS technology allows for much greater flexibility for manipulating film structure and performance, leading to films with unique properties that are often unachievable in the other PVD approaches. However, the underlying plasma mechanism for supporting film growth is currently blurred. Moreover, HiPIMS technology is still stationed in the laboratory, many films with desirable properties have not been explored under HiPIMS framework. In this work, (i) the driven mechanism of high density plasma coherent structure (i.e., spokes) in the HiPIMS discharge and (ii) how the structure and properties of the TaC/a-C:H and HfC/a-C:H films are regulated by HiPIMS were investigated. For the driven mechanism of spokes, based on the dispersion relationship of HiPIMS plasma and the evolution of the coupling between two azimuthal waves, the coupling-induced wave model was proposed. For the TaC/a-C:H and HfC/a-C:H films, the chemical bond states, structure, morphology, mechanical and tribological properties, thermal stability as well as oxidation resistance of the films were investigated. By comparison with DC deposited films, it is demonstrated that HiPIMS technology provides a potential strategy for preparing higher performance TaC/a-C:H and HfC/a-C:H films in terms of hardness, friction coefficient and wear resistance, oxidation resistance and thermal stability by modulating the chemical bonding state and nanocomposite structure of the films through HiPIMS reactive plasma.

Université Bourgogne Franche-Comté
32, avenue de l'Observatoire